

ATOM INTERFEROMETRY IN A 10 M FOUNTAIN

A DISSERTATION
SUBMITTED TO THE DEPARTMENT OF PHYSICS
AND THE COMMITTEE ON GRADUATE STUDIES
OF STANFORD UNIVERSITY
IN PARTIAL FULFILLMENT OF THE REQUIREMENTS
FOR THE DEGREE OF
DOCTOR OF PHILOSOPHY

Alex Sugarbaker
August 2014

© 2014 by Alexander Franz Sugarbaker. All Rights Reserved.
Re-distributed by Stanford University under license with the author.



This work is licensed under a Creative Commons Attribution-
Noncommercial 3.0 United States License.
<http://creativecommons.org/licenses/by-nc/3.0/us/>

This dissertation is online at: <http://purl.stanford.edu/kd753jv6128>

I certify that I have read this dissertation and that, in my opinion, it is fully adequate in scope and quality as a dissertation for the degree of Doctor of Philosophy.

Mark Kasevich, Primary Adviser

I certify that I have read this dissertation and that, in my opinion, it is fully adequate in scope and quality as a dissertation for the degree of Doctor of Philosophy.

Peter Graham

I certify that I have read this dissertation and that, in my opinion, it is fully adequate in scope and quality as a dissertation for the degree of Doctor of Philosophy.

Giorgio Gratta

Approved for the Stanford University Committee on Graduate Studies.

Patricia J. Gumpert, Vice Provost for Graduate Education

This signature page was generated electronically upon submission of this dissertation in electronic format. An original signed hard copy of the signature page is on file in University Archives.

Abstract

This thesis presents experimental results from the Stanford 10 m atom drop tower. We use atomic physics and laser spectroscopic techniques to test both general relativity and quantum mechanics. By dropping different types of atoms and observing their free-fall accelerations, it will be possible to test the equivalence principle and other general relativistic effects in the lab. By observing coherence after splitting an atom by up to 8.2 cm, we have probed the quantum-to-classical transition with increasingly macroscopic superposition states.

I will discuss our development of long-baseline atom interferometry with ^{87}Rb . We have demonstrated a record interrogation time of $2T = 2.3$ s. With $2\hbar k$ atom optics, we infer an acceleration sensitivity of $6.7 \times 10^{-12}g$ per shot. We have also measured Earth's rotation rate with 200 nrad/s precision and the direction of true North with 10 mdeg precision. I will show how spatially resolved detection and atomic point sources enable multiaxis inertial sensing.

This work has required advanced de Broglie wave atom optics. We have developed magnetic and optical-dipole lensing techniques capable of cooling atoms in two dimensions to an effective temperature of less than 50_{-30}^{+50} pK. We have also implemented large momentum transfer beamsplitters and mirrors (up to $12\hbar k$) for increased sensitivity and wavepacket separation. Many of the techniques presented here are broadly relevant to atom-interferometric precision measurement, from compact sensors of gravity, rotation, and acceleration to space-based gravitational wave detectors.

Acknowledgments

First and foremost, I thank my advisor Mark Kasevich. His optimism has pushed us to achieve the results presented in this thesis. His intuition and experience enable him to quickly give us many options to solve problems and explore new directions. He is a founder and visionary leader in our field, as evidenced by his inspiring keynote lecture at the 2013 International School of Physics “Enrico Fermi” on Atom Interferometry. I also thank my examination committee (Mark Kasevich, Peter Graham, Giorgio Gratta, Leo Hollberg, and Philip Levis) for their time.

All of the results presented in this thesis have been a collaborative effort of the EP Team, which has been a big group for an atomic physics experiment because of the 10 m scale and sheer awesomeness of the apparatus. Figure 1 shows most of the experimental and theoretical professors, postdocs, and PhD students that have contributed to the project. I’ve learned a lot from and with all of them during my time in graduate school. I would also like to acknowledge valuable discussions with our NASA collaborators, esp. Babak Saif.

The rest of the KTeam has been a great group, whether on the ski slopes, at the mandatory Patxi’s farewell dinners, during the bizarrely elected movie nights, or anytime I need to borrow the RF power meter. They are: Tim, Thomas, Philippe, Onur, Seth, David, Josh, Patrick, John, Brannon, Susannah, The Brothers Hammer, Nils, Mike, Sean, Sheng-wey, Christine, Kaspar, Catherine, Chris, Jan, Xinan, Jongmin, Hui-Chun, Chetan, Geert, Jason, Mark, Raj, Dave, Igor, Nick, Olaf, Christoph, Gunnar,¹ and other visitors, undergrads, and high school students.

Working in the Varian Physics Building wouldn’t have been possible without help

¹Here’s a puzzle for sneaky Belgians: 12842 43 121443y 138b9 2 ¾ 43 4 5314412³ 11 441. 2.13.

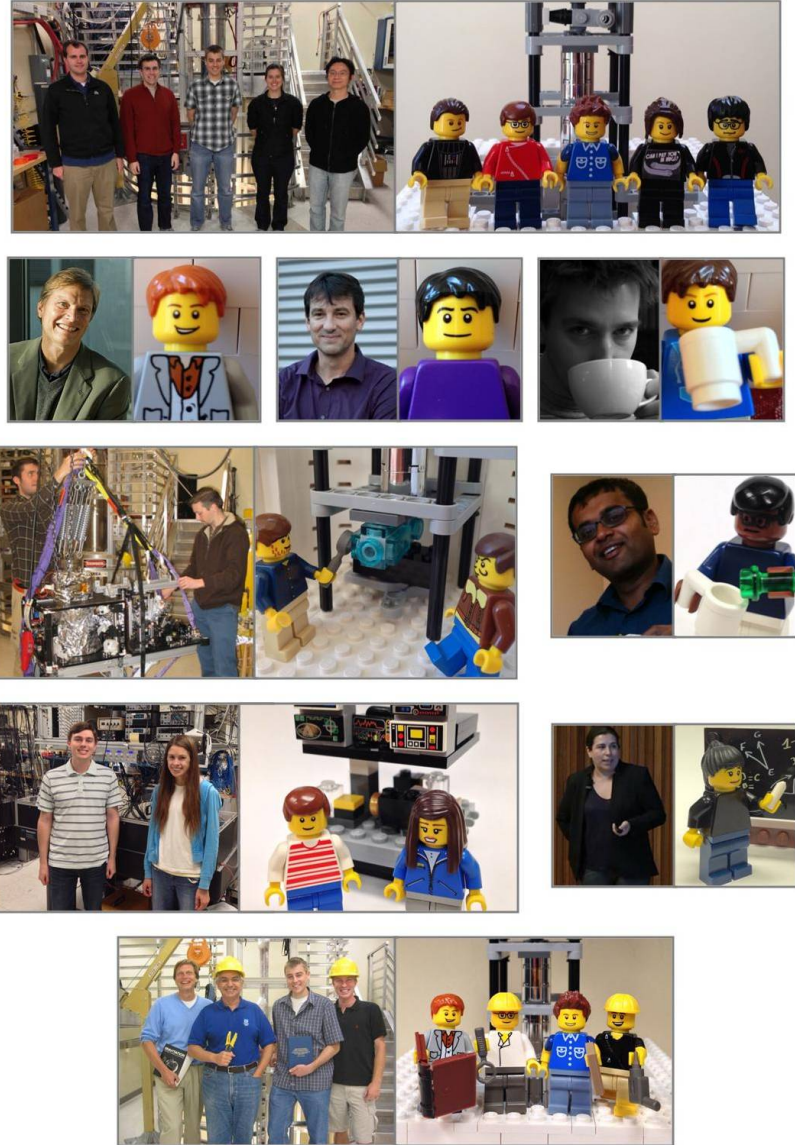


Figure 1: *From top/left:* Alex, Tim, Jason, Susannah, Sheng-wey, Mini-Me, Tiny Tim, Lego Jason, Short(er) Susannah, Harry Potter, Mark, Lego Mark, Philippe, Légo Philippe, Jan, Legö Jan, Dave, Gunnar, a lumberjack, Lego'nar (aka “the Dread Pirate Brickberts,” aka “the real stud of Lego”), Surjeet, Lego Surjeet, Chris, Christine, Christerbricks, Asimina, Lego Asimina, Mark, Savas, Jason, Peter, Lego Mixup (a little-known late-90s pop band). Thanks to David Pickett for designing and assembling the Lego caricatures.

from its wonderful administrative staff: Ping, Sha, Beth, Liz, Lucy, Stewart, and Khoi. I've been fortunate in that our lab is next to the machine shop: Karlheinz, John, Mehmet, Matt, and Scott have all helped us build the 10 m interferometer. Teaching has been a big part of grad school, and I thank Chaya, Rick, and Elva for the opportunities and support to explore new teaching methods and convey the excitement of physics to Stanford undergrads. I'm also grateful to Maria for marshaling us all through grad school – I'm sure she's glad the year of 46 is finally out the door.

I would also like to acknowledge financial support throughout graduate school from an Anne T. and Robert M. Bass Stanford Graduate Fellowship (SGF), from the National Science Foundation Graduate Research Fellowship Program (NSF GRFP), and from a National Defense Science and Engineering Graduate (NDSEG) Fellowship from the U.S. Department of Defense Air Force Research Laboratory/Air Force Office of Scientific Research (AFRL/AFOSR).

Thanks to my friends throughout the years for their support and distractions (Wellingtonians, Shoreyites, Colonizers, SPSers, Science Buses, PhysGrads, Rains Plants, Space Odysseys, Palmertons, and other Roommatesⁿ). Finally, I thank my parents, grandparents, and other family for their years of support. I didn't realize until partway through graduate school how many similarities there are between my research and that of both of my parents, as evidenced by these (suggestively abbreviated) quotes from some of their papers:

The relativistic heavy ion collider was built to create and investigate ... matter at energy densities unprecedented in a laboratory setting – matter so hot that neutrons, protons and other hadrons are expected to “melt”. [These] extreme conditions ... afford RHIC the exciting scientific opportunity to discover the properties of matter under conditions believed to pertain during a critical, though fleeting, stage of the universe’s earliest development following the big bang. The properties of such matter test fundamental predictions of quantum chromodynamics ... [1]

Standard T_2^* measurements (e.g., using conventional multiecho gradient-echo (GE) sequences) are affected by macroscopic static magnetic field (B_0) inhomogeneities ... The multi-GE slice excitation profile imaging (mGESEPI) method was developed for T_2^* measurements in the presence of macroscopic B_0 inhomogeneity, but it requires excessive acquisition times ... In this paper a more efficient technique ... is proposed. [2]

Contents

Abstract	iv
Acknowledgments	v
1 Introduction	1
1.1 Atom Interferometry	2
1.1.1 Raman Mach-Zehnder Interferometer	2
1.1.2 Interferometer Phase Shifts	5
1.2 Precision Gravity Measurements	9
1.2.1 Test of the Equivalence Principle	10
1.2.2 Other Laboratory Tests of General Relativity	12
1.2.3 Gravitational Waves	13
1.3 Macroscopic Quantum Mechanics	16
1.4 Organization of this Thesis	19
2 Experimental Apparatus and Methods	21
2.1 Experimental Overview	21
2.2 Interferometer Region (Free Fall)	25
2.2.1 Vacuum System	26
2.2.2 Magnetic Shielding	30
2.2.3 Atom Optics Lasers	33
2.2.4 Primary Telescope	41
2.2.5 Rotation Compensation System	42
2.3 Atom Source (Cooling)	45

2.3.1	Magneto-Optical Trap	45
2.3.2	Magnetic Trap Evaporation	48
2.3.3	Optically Plugged Quadrupole Trap	52
2.3.4	TOP Trap	53
2.3.5	Magnetic Lens	57
2.3.6	State Preparation	57
2.4	Launch	58
2.4.1	Coherent Optical Lattice Launch	58
2.4.2	Lattice Beam Geometry	60
2.4.3	Optimizing Lattice Launch Parameters	62
2.5	Detection	66
3	Long-Time Atom Interferometry	70
3.1	Point Source Interferometry (PSI)	70
3.2	Apparatus and Methods	72
3.2.1	Creation of the Atomic Point Source	72
3.2.2	Two-Photon Raman Atom Optics	74
3.2.3	Detection	75
3.2.4	Rotation Compensation	75
3.3	High-Contrast Interferometry	76
3.3.1	Rotation-Compensated Interferometer	76
3.3.2	Extended High-Contrast Regime with Spatial Imaging	76
3.4	Multi-Axis Gyroscope	79
3.5	Differential Accelerometer Sensitivity	80
3.6	Applications	81
3.7	Principal Component Analysis	81
4	Phase Shear Readout (PSR)	85
4.1	Atom Interferometry with Spatial Fringes	85
4.2	Apparatus and Methods	88
4.3	Beam-Tilt Phase Shear	88
4.4	Single-Shot Phase Readout	91

4.5	Gyrocompass	91
4.5.1	Differential Heterodyne Measurement	93
4.6	Timing-Asymmetry Phase Shear	95
4.6.1	Hybrid Phase Shears in 3D	95
4.7	Applications	97
5	Lens Cooling	98
5.1	Optical Dipole Lensing	99
5.1.1	Delta-Kick Cooling	99
5.1.2	Optical Dipole Lens	99
5.1.3	Refocusing to Analyze Pikokelvin Temperatures	100
5.1.4	Apparatus and Methods	101
5.1.5	Refocusing Results	103
5.1.6	Temperature Bounds	105
5.1.7	Limits from Initial Size and Gaussian Aberrations	105
5.1.8	Applications	107
5.2	Magnetic Lens Cooling	107
5.2.1	TOP Trap Thick Lens	108
5.2.2	Magnetic Lens Oscillations	108
5.2.3	Temperature Results	108
5.2.4	Lattice-Assisted Magnetic Lens Cooling	110
5.3	Implications and Conclusion	110
6	Large Momentum Transfer	113
6.1	Sequential Raman LMT	114
6.2	$12\hbar k$ Interferometer with 8.2 cm Wavepacket Separation	116
6.3	Sources of Contrast Loss and Ongoing Work	117
6.3.1	Spontaneous Emission	119
6.3.2	Rabi Frequency and Detuning Variations	120
6.3.3	Inhomogeneous Interferometer Phase	120
7	Conclusion	122

A Spontaneous Heating Rate Limit	124
A.1 Heating from a Classicalizing Modification to Quantum Mechanics . . .	124
A.2 Classical Model: Fokker-Planck Equation with a Stochastic Force . . .	126
A.3 Stochastic Modifications of the Trajectories	127
A.4 Delta-Kick Sequence with Stochastic Modification	128
A.4.1 Object to Lens	129
A.4.2 Lens to Image	129
A.4.3 Constraining the Heating Rate with Refocusing Data	130
B Miniaturization	132
Bibliography	134

List of Tables

1.1	Acceleration Sensitivity	10
3.1	PSI Phases	71
A.1	Stochastic Variable Correlations with Initial Distribution	128
A.2	Noise Averages of Stochastic Variable Correlations	128

List of Figures

1	Acknowledgments	vi
1.1	Raman Mach-Zehnder Light-Pulse Atom Interferometer	3
1.2	Space-Time Diagram	7
1.3	Atomic Gravitational Wave Interferometric Sensor	14
1.4	Constraints on Macroscopic Quantum Mechanics	18
2.1	Full Apparatus	23
2.2	Full Timing Diagram	24
2.3	Full Experiment Photo	27
2.4	Titanium Sublimation	29
2.5	Atom Number vs. Launch Height	30
2.6	Magnetic Shielding	32
2.7	Z-Axis Laser Beams	34
2.8	Rubidium Spectrum	35
2.9	Beam Size Constraints	42
2.10	Primary Telescope Lens	43
2.11	Rotation Compensation System	44
2.12	Atom Source	46
2.13	Cooling and Trapping Lasers	49
2.14	Z-Axis Lasers	50
2.15	High Power Lasers	51
2.16	Optically Plugged Trap	53
2.17	TOP Coil Drive Circuit	56

2.18	Quantization of the Launch Velocity	59
2.19	Lattice Launch Intensity and Detuning	65
2.20	Lattice Launch: Red vs. Blue	67
2.21	Imaging Lenses	68
3.1	PSI Apparatus	73
3.2	PSI Fringes	74
3.3	PSI Interferometers	77
3.4	PSI Frequencies	78
3.5	PSI Gyroscope	80
3.6	PSI Principal Component Analysis Example	82
4.1	PSR Apparatus	87
4.2	PSR Fringes	90
4.3	PSR Single Shot Phase	92
4.4	PSR Gyrocompass	94
4.5	PSR Fringe Control	96
5.1	Lensing Apparatus	102
5.2	Lensing Beam Aberrations	103
5.3	Cloud Size Versus Lens Duration	104
5.4	Relay Lensing	106
5.5	Magnetic Lens Oscillations	109
5.6	Lattice-Assisted Magnetic Lens Cooling	111
6.1	LMT Space-Time Diagram	115
6.2	LMT Contrast and Spontaneous Emission	118
B.1	Miniaturization	133

Chapter 1

Introduction

The Stanford 10 m drop tower provides a pristine environment in which to observe the free-fall dynamics of neutral atoms over several seconds. This allows for precise measurements of gravity and general relativity in the lab. In particular, the experiment targets testing the equivalence principle to one part in 10^{15} . Many of the concepts and techniques developed with this apparatus are also germane to proposed atom interferometer gravitational wave detectors, which could open a new window to the universe.¹

Measurements are made with many atoms simultaneously to facilitate differential measurements and improve statistics. This necessitates state-of-the art neutral atom cooling and trapping techniques to ensure consistent initial conditions across the ensemble prior to free fall. Conversely, the long drift time facilitates precise temperature measurements and new cooling techniques, pushing the bounds of ultracold temperatures even lower.

To measure forces acting on the atoms while they are in flight, we use atom interferometry. This leverages the de Broglie-wave nature of the atoms to make an interferometric fringe. As with optical interferometry, this enables precision measurements. But unlike photons, atoms are massive (and can also interact more strongly with other fields), allowing for new measurements and sensors. The interferometric

¹I use footnotes liberally throughout this thesis. The footnotes should not be necessary for general understanding – my intention is move details to the footnotes to improve the flow of the main text. Many calculations or quantitative justifications are also relegated to the footnotes.

measurement also entails splitting the atomic wavepacket over large distances. The creation of such macroscopic superposition states tests quantum mechanics in ever more macroscopic regimes.

1.1 Atom Interferometry

In atom interferometry, atoms are split and caused to follow spatially separated paths. The disparate parts of the atom are then brought back together to form an interference pattern. The interference is sensitive to the phase difference accrued by the atoms along the distinct paths. This phase depends on the exact evolution of the atomic wavefunction, which is in turn sensitive to the potential explored by the atom. This yields the precision measurement. Atom interferometry is reviewed in [3] and [4].

Atom interferometers have been used for a variety of precision measurements. They have measured the gravitational [5, 6] and fine-structure [7] constants. They have also enabled the realization of high performance gyroscopes [8], accelerometers [9], gravimeters [10], gravity gradiometers [11], and magnetometers [12].² These instruments can now be made compact, robust, and portable, with applications in inertial navigation, geodesy, and mineral exploration [14, 15].

1.1.1 Raman Mach-Zehnder Interferometer

Atoms can be split and interfered in a variety of ways. This thesis focuses on Raman light-pulse atom interferometry in the Mach-Zehnder configuration (see Figure 1.1). In light-pulse atom interferometry, short pulses of light are used to split, redirect, and recombine the atomic wavepackets. Between the pulses, the atoms are in free fall, affected only by the forces being measured.

A Mach-Zehnder (or Kasevich-Chu [16]) atom interferometer is analogous to its counterpart in optical interferometry [Fig. 1.1(d)]. An initial beamsplitter splits the incident wave (or wavepacket in the case of the atom) and directs it along two spatially separated interferometer arms. Mirror reflections then redirect the two arms so that

²Atomic clocks [13] could be added to this list as well. Clocks and interferometers have much in common. Both are examples of modern precision atomic spectroscopy.

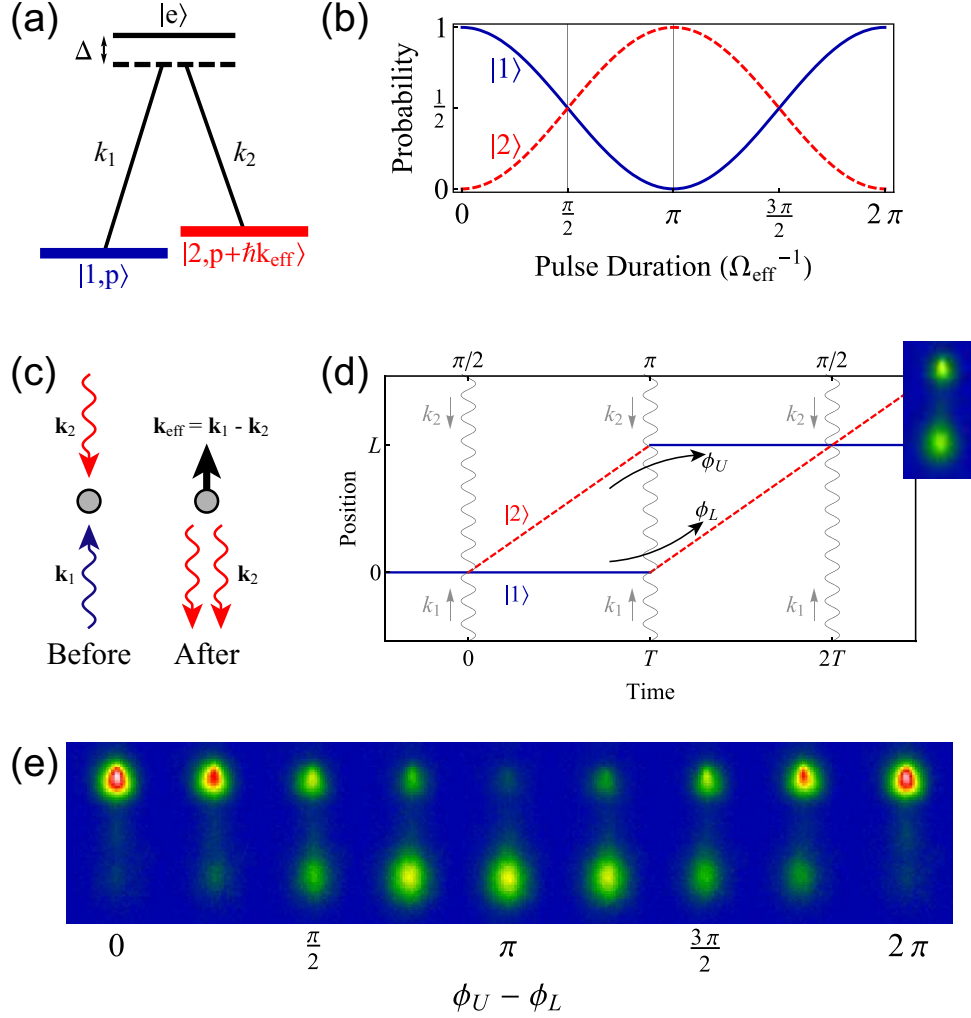


Figure 1.1: Raman Mach-Zehnder light-pulse atom interferometer. (a) Effective two-level system with hyperfine ground states $|1\rangle$ and $|2\rangle$. Counterpropagating lasers (c) with wavevectors k_1 and k_2 couple the ground states via two-photon Raman transitions. (b) Rabi flopping occurs while the lasers are on. Beamsplitters and mirrors can be implemented by pulsing the lasers for the $\pi/2$ and π times respectively. (d) Space-time diagram for a Mach-Zehnder, three-pulse configuration, with no external forces. A sample image of the atom density distribution at the two spatially resolved output ports is also shown. (d) Sequence of images of the output ports as a function of the phase difference $\phi_U - \phi_L$ between the upper and lower interferometer arms. The data are from the interferometer in Fig. 3.3(c), wherein the phase is scrambled by vibrations of the laser beam delivery optics. Here, the images have been sorted by their measured phases, and the phase indicated is approximate.

they overlap at a final beamsplitter. Interference occurs at the final beamsplitter, and each atom can be detected in one of two spatially distinct output ports. The probability of detecting an atom exiting from a given port depends on the phase difference between the two interferometer arms [Fig. 1.1(e)]. The two ports are out of phase by 180° : when one port is “light” (all the atoms exit), the other is “dark” (no atoms exit).³

The interferometers discussed in this thesis use two-photon Raman transitions for the beamsplitters and mirrors.⁴ Consider the first beamsplitter in the vertical interferometer in Fig. 1.1(d), with the atom initially in state $|1\rangle$. Laser light incident from below, with wavevector \mathbf{k}_1 , is absorbed by the atom. The atom then undergoes stimulated emission into a second laser beam, with wavevector \mathbf{k}_2 , incident from above. The full two-photon process transfers the atom into state $|2\rangle$ and gives it an upwards momentum kick [Fig. 1.1(b)]

$$\Delta\mathbf{p} = \hbar\mathbf{k}_1 - \hbar\mathbf{k}_2 \equiv \hbar\mathbf{k}_{\text{eff}} \approx 2\hbar\mathbf{k}_1 \text{ (two photon recoils)} \quad (1.1)$$

For a Raman transition, $|1\rangle$ and $|2\rangle$ are ground states and the two-photon transitions are driven through a virtual state that is far detuned (Δ) from an excited state $|e\rangle$.⁵ This forms an effective two-level system [Fig. 1.1(a)]. Therefore, while the light is on, the atom undergoes Rabi oscillations between $|1, \mathbf{p}\rangle$ and $|2, \mathbf{p} + \hbar\mathbf{k}_{\text{eff}}\rangle$ [Fig. 1.1(b)]. Specifically, the populations of the two states are

$$|c_1(t)|^2 = \cos^2\left(\frac{\Omega_{\text{eff}}t}{2}\right) \quad (1.2)$$

$$|c_2(t)|^2 = \sin^2\left(\frac{\Omega_{\text{eff}}t}{2}\right) \quad (1.3)$$

³This assumes perfect contrast and a uniform interferometer phase across the cloud, see Chapters 3 and 4.

⁴Several alternatives to Raman transitions exist. Chapter 6 uses sequential two-photon Raman transitions. Bragg transitions, not discussed here, are another two-photon process in which the atom returns to the same hyperfine ground state [17]. Single-photon atom interferometry with alkaline-earth-like atoms has also been proposed [18].

⁵For our ^{87}Rb Raman interferometers, $|1\rangle$ and $|2\rangle$ are the hyperfine ground states $|F = 1\rangle$ and $|F = 2\rangle$ respectively, and $|e\rangle$ is the $5^2\text{P}_{3/2}$ manifold (typically Δ is much greater than the $5^2\text{P}_{3/2}$ hyperfine splitting, see Figure 2.8).

where t is the time since the start of the optical pulse and Ω_{eff} is the two-photon Rabi frequency (Eq. 2.4). Here I have assumed perfect coherence (no spontaneous emission) and that the two-photon detuning $\delta = 0$ (though the single-photon detuning $\Delta \neq 0$).

For an optical pulse of duration $\delta t_{\pi/2} = \frac{\pi}{2}\Omega_{\text{eff}}^{-1}$, $|c_1|^2 = |c_2|^2 = 1/2$ and the atom is placed in an equal superposition of $|1, \mathbf{p}\rangle$ and $|2, \mathbf{p} + \hbar\mathbf{k}_{\text{eff}}\rangle$. Therefore, this pulse (a $\pi/2$ pulse) acts as a beamsplitter. Likewise, a π pulse with duration $\delta t_\pi = \pi\Omega_{\text{eff}}^{-1}$ yields complete inversion $|1, \mathbf{p}\rangle \leftrightarrow |2, \mathbf{p} + \hbar\mathbf{k}_{\text{eff}}\rangle$, and thus acts as a mirror. Figure 1.1(d) shows how a sequence of three such pulses ($\frac{\pi}{2}-\pi-\frac{\pi}{2}$) can open and close the interferometer.⁶ The time interval T between the pulses, combined with the momentum splitting $\hbar k_{\text{eff}}$, sets the scale (or area) of the interferometer, with larger interferometers having better sensitivity (Equation 1.11).

After the final beamsplitter, the two interferometer output ports have different momenta [Fig. 1.1(d)]. Therefore, they become spatially separated over time and can then be distinguished by imaging them with a spatially resolved detector. The interferometer phase can be inferred from the relative abundances of atoms in the two ports [Fig. 1.1(e)]. The following section discusses the origin of this phase.

1.1.2 Interferometer Phase Shifts

The phase difference between the two arms of the interferometer depends on the physical effects to be measured (the forces acting on the atom). Conceptually, the atom can be thought of as a classical proof mass, and the laser phase fronts as sub-micron rulers. These rulers measure the atom's position at each of the three optical pulses (three position measurements determine a uniform acceleration) [19]. In the semi-classical limit, the phase shift between the two arms of a three-pulse interferometer is

$$\Delta\phi_{\text{sc}} = \phi_1 - 2\phi_2 + \phi_3 \quad (1.4)$$

⁶Unlike in the optical Mach-Zehnder, the same mirror can address both arms in an atom interferometer.

where $\phi_i \equiv \phi_{\text{eff},i}(\mathbf{r}, t)$ is the effective laser phase (the phase difference between the two Raman lasers) at the classical position of the atom at the time of the i th pulse [3, 16].⁷

While Equation 1.4 is sufficient to determine almost all of the phase shifts discussed in this thesis, it is not fully general, nor is it trivial to justify its form from first principles. A full quantum mechanical treatment [14, 20, 21]⁸ shows that the total phase shift can be decomposed into three components

$$\Delta\phi_{\text{tot}} = \Delta\phi_{\text{prop}} + \Delta\phi_{\text{sep}} + \Delta\phi_{\text{las}} \quad (1.5)$$

Each of these terms depends on the trajectory of the atom through the interferometer, as determined by the optical pulses and the atom's free evolution with Lagrangian

$$L = \frac{1}{2}m(\dot{\mathbf{r}} + \boldsymbol{\Omega} \times (\mathbf{r} + \mathbf{R}_e))^2 - m\phi(\mathbf{r} + \mathbf{R}_e) \pm \frac{1}{2}\hbar\alpha\mathbf{B}(\mathbf{r})^2 \quad (1.6)$$

where m and \mathbf{r} are the mass and position of the atom, and \mathbf{R}_e and $\boldsymbol{\Omega}$ are Earth's radius and rotation rate. The gravitational potential is $\phi(\mathbf{r} + \mathbf{R}_e) = -(\mathbf{g} \cdot \mathbf{r} + \frac{1}{2}(T_{ij})r_i r_j + \dots)$, where \mathbf{g} is Earth's local gravitational field and $T_{ij} \equiv \partial_j g_i$ is the gravity gradient tensor. The magnetic field \mathbf{B} affects the atoms only through their second-order Zeeman shift α since they are kept in $|m_F = 0\rangle$ states throughout the interferometer.⁹

For the $\frac{\pi}{2}$ - π - $\frac{\pi}{2}$ interferometer discussed here, there are five semi-classical interaction vertices in the trajectory (labeled ABCDE in Figure 1.2). Each of the components of $\Delta\phi_{\text{tot}}$ can be evaluated with respect to these vertices as follows:

Propagation Phase The propagation phase $\Delta\phi_{\text{prop}}$ arises from the evolution of the atom wavefunction between the optical pulses. Specifically, this occurs along two path segments for the lower arm (AB and BD) and two path segments for the upper

⁷The effective phase is the phase difference between the two Raman lasers. The notation in Eq. 1.4 (in which the subscripts {1,2,3} indicate the pulse number) conflicts somewhat with the rest of this chapter (in which the subscripts {1,2} label the counterpropagating Raman beams). Both notations are standard, and it should be clear from the context which is meant.

⁸General relativity can also be included [20, 22, 23]. This is relevant to laboratory tests of GR and gravitational wave detection.

⁹Specifically, the second-order Zeeman shift is negative for atoms in $|F = 1\rangle$ (− sign in Eq. 1.6) and positive for atoms in $|F = 2\rangle$ (+ sign in Eq. 1.6).

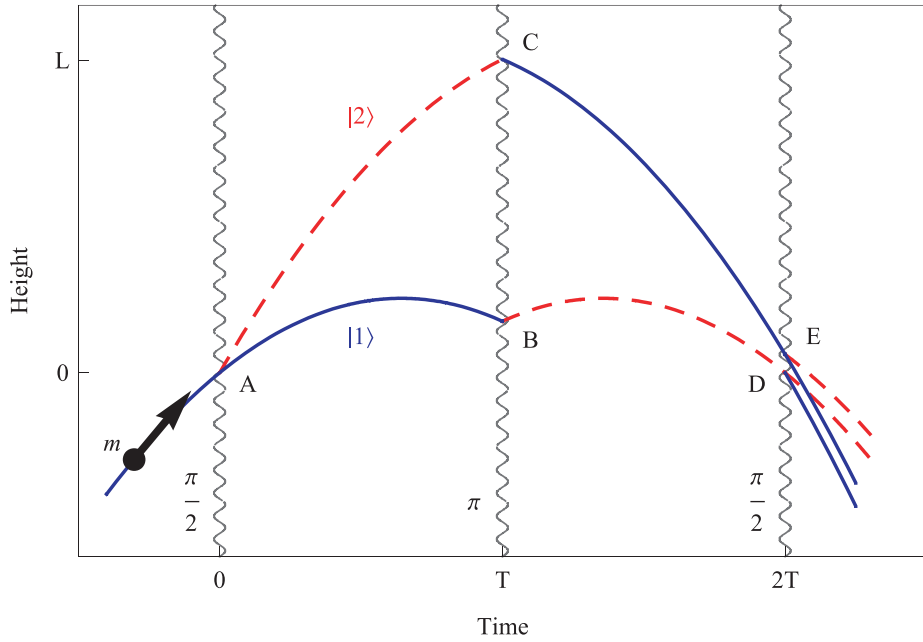


Figure 1.2: Non-relativistic space-time diagram for a $\frac{\pi}{2}$ - π - $\frac{\pi}{2}$ Raman light-pulse atom interferometer (see also Fig. 1.1). The trajectories shown are for the relevant case of a Lagrangian dominated by a uniform gravitational acceleration with small perturbations, and the five semi-classical interaction vertices are labeled ABCDE. The general case where the two arms do not intersect at the output ($\mathbf{r}_D \neq \mathbf{r}_E$) is shown. While the pulses shown are spaced symmetrically by time T , there can in general be an asymmetry (see Section 4.6). Adapted from [20].

arm (AC and CE). The phase shift is

$$\Delta\phi_{\text{prop}} = \frac{1}{\hbar} \left((\tilde{S}_{AC} + \tilde{S}_{CE}) - (\tilde{S}_{AB} + \tilde{S}_{BD}) \right) \quad (1.7)$$

where $\tilde{S}_{ij} = \int_{t_i}^{t_j} (L - E_f) dt$ accounts for both the classical action and the atom's internal energy (E_f in state $|f\rangle$) along the segment connecting vertices \mathbf{r}_i and \mathbf{r}_j .

Separation Phase The separation phase $\Delta\phi_{\text{sep}}$ arises from an imperfect overlap of the two interferometer arms at the final beamsplitter: $\mathbf{r}_D \neq \mathbf{r}_E$. This causes a phase shift

$$\Delta\phi_{\text{sep}} = \frac{1}{\hbar} \left(\frac{\mathbf{p}_{1,D} + \mathbf{p}_{1,E}}{2} \right) \cdot (\mathbf{r}_D - \mathbf{r}_E) \quad (1.8)$$

where $\mathbf{p}_{1,i} = \partial_{\dot{\mathbf{r}}} L(\mathbf{r}_i)$ is the classical canonical momentum after the final beamsplitter in the lower output port (state $|1\rangle$) at the vertex \mathbf{r}_i .

Laser Phase The laser phase $\Delta\phi_{\text{las}}$ arises from interactions of the atoms with the light during the optical pulses. A full solution to the two-level Rabi problem (for which only the population amplitudes were given in Eq. 1.3) shows that in the short pulse limit [20] the laser phase is imprinted on the part of the wavepacket that receives a momentum kick $\hbar k_{\text{eff}}$. The sign of the phase depends on whether the atom gains or loses momentum during the transition.¹⁰ The resulting phase shift is

$$\Delta\phi_{\text{las}} = \left(\phi_L(\mathbf{r}_A, 0) - \phi_L(\mathbf{r}_C, T) \right) - \left(\phi_L(\mathbf{r}_B, T) - \phi_L(\mathbf{r}_D, 2T) \right) \quad (1.9)$$

where $\phi_L(\mathbf{r}, t) = \mathbf{k}_{\text{eff}} \cdot \mathbf{r} - \omega_{\text{eff}} t + \phi_{\text{eff}}$. For the two-photon Raman transitions discussed here, $\mathbf{k}_{\text{eff}} \equiv \mathbf{k}_2 - \mathbf{k}_1$, $\omega_{\text{eff}} \equiv \omega_2 - \omega_1$, and $\phi_{\text{eff}} \equiv \phi_2 - \phi_1$ are the wavevector, frequency, and phase differences between the two Raman lasers.¹¹

¹⁰Specifically, $|1, \mathbf{p}\rangle \rightarrow |2, \mathbf{p} + \hbar\mathbf{k}_{\text{eff}}\rangle e^{i\phi_L}$ and $|2, \mathbf{p} + \hbar\mathbf{k}_{\text{eff}}\rangle \rightarrow |1, \mathbf{p}\rangle e^{-i\phi_L}$.

¹¹Equations 1.7 to 1.9 are for the lower port (state $|1\rangle$). For the other port, $\Delta\phi_{\text{prop}}$ is unchanged, but $\mathbf{p}_{1,i} \rightarrow \mathbf{p}_{2,i} = \mathbf{p}_{1,i} + \hbar\mathbf{k}_{\text{eff}}$ and $\phi_L(\mathbf{r}_D, 2T) \rightarrow \phi_L(\mathbf{r}_E, 2T)$ (two minus signs cancel switching from an atom kicked *down* from the *lower* arm into the *lower* output port to an atom kicked *up* from the *upper* arm into the *upper* output port). As a result, $\Delta\phi_{\text{prop},2} = \Delta\phi_{\text{prop},1}$, while $\Delta\phi_{\text{sep},2} = \Delta\phi_{\text{sep},1} + \mathbf{k}_{\text{eff}} \cdot (\mathbf{r}_D - \mathbf{r}_E)$ and $\Delta\phi_{\text{las},2} = \Delta\phi_{\text{las},1} - \mathbf{k}_{\text{eff}} \cdot (\mathbf{r}_D - \mathbf{r}_E)$. Thus, $\Delta\phi_{\text{tot},2} = \Delta\phi_{\text{tot},1}$, and the phase shift is the same regardless of which output port is considered.

A full phase shift calculation then entails determining the classical trajectories of the Lagrangian (Eq. 1.6) and then using Eqs. 1.7 to 1.9 to determine the phase shift [20, 21]. However, many terms often cancel, and for a wide range of effects it is sufficient to consider only the laser phase in the limit $\mathbf{r}_C \approx \mathbf{r}_B$, in which case the total phase shift reduces to the semi-classical limit (Eq. 1.4).

1.2 Precision Gravity Measurements

Ultracold neutral atoms are pristine inertial test masses with which to test gravity. Their free fall can be observed over long times, and their trajectories can be precisely measured with atom interferometry. This has enabled precision measurements of the universal gravitational constant G [5, 6]. As will be discussed in this section, atom interferometry also facilitates laboratory tests of the equivalence principle and general relativity. It could also be used for gravitational wave detection.

The high sensitivity of atom interferometry to gravitational effects can be seen by evaluating the phase shift of a $\frac{\pi}{2}$ - π - $\frac{\pi}{2}$ interferometer in the presence of a uniform gravitational acceleration \mathbf{g} . Using the method outlined in Section 1.1.2, the phase shift is found to be

$$\Delta\phi_g = k_{\text{eff}} g T^2 \approx 2NkgT^2 \quad (1.10)$$

As discussed in Chapter 6, this phase shift increases with large momentum transfer (LMT) atom optics ($N > 1$). In this case, the beamsplitters and mirrors impart a momentum $\hbar k_{\text{eff}} = 2N\hbar k > 2\hbar k$ to the atom.

Atom shot noise limits the phase resolution of modern atom interferometric sensors.¹² For a sensor with a time-averaged atom flux of n ,¹³ the shot-noise-limited

¹²That is, it is typically possible to reduce other noise sources below the level of shot noise. Squeezed states could reduce the noise level below the shot noise limit [24–27]. At the Heisenberg limit, the phase sensitivity is a factor of \sqrt{n} better.

¹³The effective flux is $n = f\mathcal{N}q\tau^{-1}$, where f is the contrast, \mathcal{N} is the atom number per shot, τ^{-1} is the experimental repetition rate, and q is the number of interferometers run concurrently [23].

	1	2	3	4
n (atoms/s)	10^5	10^4	5×10^4	2.5×10^5
$\hbar k_{\text{eff}}$	$2\hbar k$	$20\hbar k$	$50\hbar k$	$100\hbar k$
T (s)	1.15	1.15	1.15	1.15
$\Delta\phi_g = k_{\text{eff}}gT^2$	2×10^8	2×10^9	5×10^9	1×10^{10}
Sensitivity ($g/\sqrt{\text{Hz}}$)	2×10^{-11}	5×10^{-12}	9×10^{-13}	2×10^{-13}
η_{AI} (g , One Hour)	3×10^{-13}	8×10^{-14}	1×10^{-14}	3×10^{-15}
η_{AI} (g , One Day)	5×10^{-14}	2×10^{-14}	3×10^{-15}	7×10^{-16}
η_{AI} (g , One Month)	9×10^{-15}	3×10^{-15}	5×10^{-16}	1×10^{-16}

Table 1.1: Phase shifts and sensitivities for atom interferometers with varied atom flux n and momentum splitting $\hbar k_{\text{eff}}$ for $T = 1.15$ s. Column 1 corresponds to the interferometer presented in Section 3.5 (where the sensitivity is given per shot, with an experimental repetition rate of $\tau^{-1} = (20 \text{ s})^{-1}$). The remaining columns show improvements that would yield $\sim 10^{-15}$ precision in a month, day, or hour of integration. Column 2 assumes a lower atom number since more aggressive cooling and/or velocity selection is needed for high contrast LMT interferometry. Columns 3 or 4 therefore need compensating improvements in cooling efficiency and/or repetition rate.

phase resolution is $\delta\phi \sim 1/\sqrt{n}$. This yields an acceleration sensitivity of

$$\delta g = \left(\frac{\delta\phi}{\Delta\phi_g} \right) g = \frac{1/\sqrt{n}}{k_{\text{eff}}T^2} \quad (1.11)$$

Table 1.1 shows the phase shift and shot-noise-limited sensitivity for several interferometers, including one at our current performance level (Chapter 3). The other columns highlight performance improvements that could yield a precision of $\sim 10^{-15}g$ after a month, day, or hour of data collection. This would enable the equivalence principle test discussed in the next section.

1.2.1 Test of the Equivalence Principle

The Stanford 10 m drop tower was designed to test the equivalence principle with atom interferometry at high precision [14, 28]. The equivalence principle states that

all objects fall with the same acceleration under the influence of gravity.¹⁴ It is the foundational assumption of Einstein’s general relativity, so testing it probes our fundamental understanding of gravity. A violation of the equivalence principle can be viewed as the observation of a fifth force, revealing new physics.

Equivalence principle tests are typically characterized by the Eötvös parameter

$$\eta = \left| \frac{\Delta a}{\bar{a}} \right| = \frac{|a_1 - a_2|}{\frac{1}{2}|a_1 + a_2|} \quad (1.12)$$

where a_1 and a_2 are the (potentially different) accelerations of two freely-falling test masses. The current best limits on violations of the equivalence principle constrain $\eta < 10^{-13}$. Laser-lunar ranging yields a precise measurement of the distance between the Earth and the Moon, which can in turn be used to constrain EP-violating differences in their accelerations toward the Sun at $\eta = (-1.0 \pm 1.4) \times 10^{-13}$ [30]. A torsion pendulum experiment has constrained $\eta = (0.3 \pm 1.8) \times 10^{-13}$ between beryllium and titanium test masses [31].¹⁵ Atom interferometric measurements with freely-falling atoms have also been made ($\eta_{^{85}\text{Rb}-^{87}\text{Rb}} = (1.2 \pm 1.7) \times 10^{-7}$ [32], $\eta_{^{133}\text{Cs}-\text{CornerCube}} = (7 \pm 7) \times 10^{-9}$ [10],¹⁶ $\eta_{^{39}\text{K}-^{87}\text{Rb}} = (0.3 \pm 5.4) \times 10^{-7}$ [33], and $\eta_{^{87}\text{Sr}-^{88}\text{Sr}} = (0.2 \pm 1.6) \times 10^{-7}$ [34]). They have not yet reached the same sensitivity levels, but the field is rapidly evolving and the fundamental sensitivity improvement of a 10 m scale apparatus is significant (Section 3.5).

Our experiment aims to test the equivalence principle at the level of $\eta = 10^{-15}$ by using atom interferometry to compare the free-fall accelerations of ^{85}Rb and ^{87}Rb in the Stanford 10 m drop tower. The sensitivity can be computed from Eq. 1.11 and

¹⁴Here I implicitly focus on the weak equivalence principle, which states that in the absence of all other forces, the motion of a test mass in a gravitational field is locally indistinguishable from its motion in a uniformly accelerated frame. Ensuring “the absence of all other forces” corresponds to controlling systematic effects (primarily electromagnetic for our experiment). Stronger versions of the equivalence principle exist, but are not directly tested by the experiment proposed here [29].

¹⁵Other classic experiments include Galileo’s supposed dropping of balls with different masses from the Leaning Tower of Pisa and Apollo 15 astronaut David Scott’s dropping of a hammer and a feather on the Moon.

¹⁶The corner cube and atom interferometric measurements were not made concurrently.

Eq. 1.12:

$$\eta_{\text{AI}} \approx \frac{|\Delta\phi_{87} - \Delta\phi_{85}|}{k_{\text{eff}} g T^2} \quad (1.13)$$

Table 1.1 shows the operating parameters and integration times necessary to reach a statistical sensitivity of $\eta_{\text{AI}} \sim 10^{-15}$ with our apparatus. It is also necessary to reduce or measure systematic perturbations to this level. Such systematics include magnetic fields, gravity gradients, the Coriolis effect, laser phase noise, and laser wavefront errors. The phase shifts associated with these effects can be calculated as outlined in Section 1.1.2. By running the ^{85}Rb and ^{87}Rb interferometers simultaneously with common lasers, many systematics are common and are heavily suppressed in the differential measurement of $|\Delta\phi_{87} - \Delta\phi_{85}|$. Nevertheless, imperfect initial conditions and isotope-dependent susceptibilities to some systematics yield differential phase shifts that need to be mitigated at the 10^{-15} level [14, 20]. Many aspects of the apparatus (Chapter 2) are designed with this goal.

1.2.2 Other Laboratory Tests of General Relativity

While the equivalence principle test will yield a null measurement if general relativity holds, several other interesting effects could be measured with an atom interferometer with acceleration sensitivity at the $10^{-15}g$ level [28, 35]. For instance, it would be possible to observe the gravitation of the atom's kinetic energy. One could also detect gravity sourced by the energy density of the gravitational field itself. The observation of these effects would make it possible to constrain alternative theories of gravity.¹⁷ They would join gravitational redshift tests [36, 37] in the canon of laboratory tests of general relativity.

¹⁷The parameterized post-Newtonian (PPN) expansion provides a means of comparing alternative theories of gravity. The strengths of the velocity and self-gravitation source terms will in general vary for different theories. Since general relativity is not the only theory in which the equivalence principle holds, constraining the PPN parameters could be a stronger test of relativity [22, 28].

1.2.3 Gravitational Waves

Atom interferometers could also play a role in the direct detection of gravitational waves. General relativity predicts that accelerating masses generate gravitational radiation, just as accelerating charges generate electromagnetic radiation [38]. Gravitational waves propagate at the speed of light as fluctuations in space-time. They interact with matter only weakly, making them difficult to detect. Nevertheless, experimental searches are underway with sensitivities predicted to be sufficient to detect gravitational waves from the binary inspirals of compact objects (black holes, neutron stars, white dwarfs) [39, 40].¹⁸

The direct detection of gravitational waves would provide resounding support for general relativity. It would also open up a new way of looking out into the universe - a new branch of astronomy and astrophysics. This would extend well beyond studying the abundances and properties of binary inspirals. The surface of last scattering is transparent to gravitational waves because of their weak coupling. Therefore, they could be used to look further back into the early universe than is possible with light. For instance, it might be possible to directly observe cosmological gravitational waves from inflation or other sources.¹⁹

Most modern gravitational wave detectors are optical interferometers with macroscopic proof masses. As a gravitational wave passes, the distance between the proof masses is modulated at the gravitational wave frequency by the expansion and contraction of spacetime, and the signal is read out interferometrically. Examples of such instruments include the ground-based \sim kilometer-baseline LIGO, VIRGO, GEO600, and TAMA300 detectors [40]. A satellite mission has also been proposed (LISA [44]) to extend the baseline and avoid fundamental noise from Earth's time-varying gravitational field. This would improve sensitivity at lower frequencies, where there are more binary inspiral sources [Figure 1.3(b)] and potentially stronger cosmological sources.

Atom interferometry could expand and improve upon the existing gravitational

¹⁸At present, these experiments have only set upper limits [41, 42].

¹⁹Indirect evidence for inflationary gravitational waves results from the recently-measured B-mode spectrum of the cosmic microwave background [43]. A direct measurement of this spectrum at smaller length scales (corresponding to mHz gravitational wave frequencies) would further constrain inflationary theories [42].

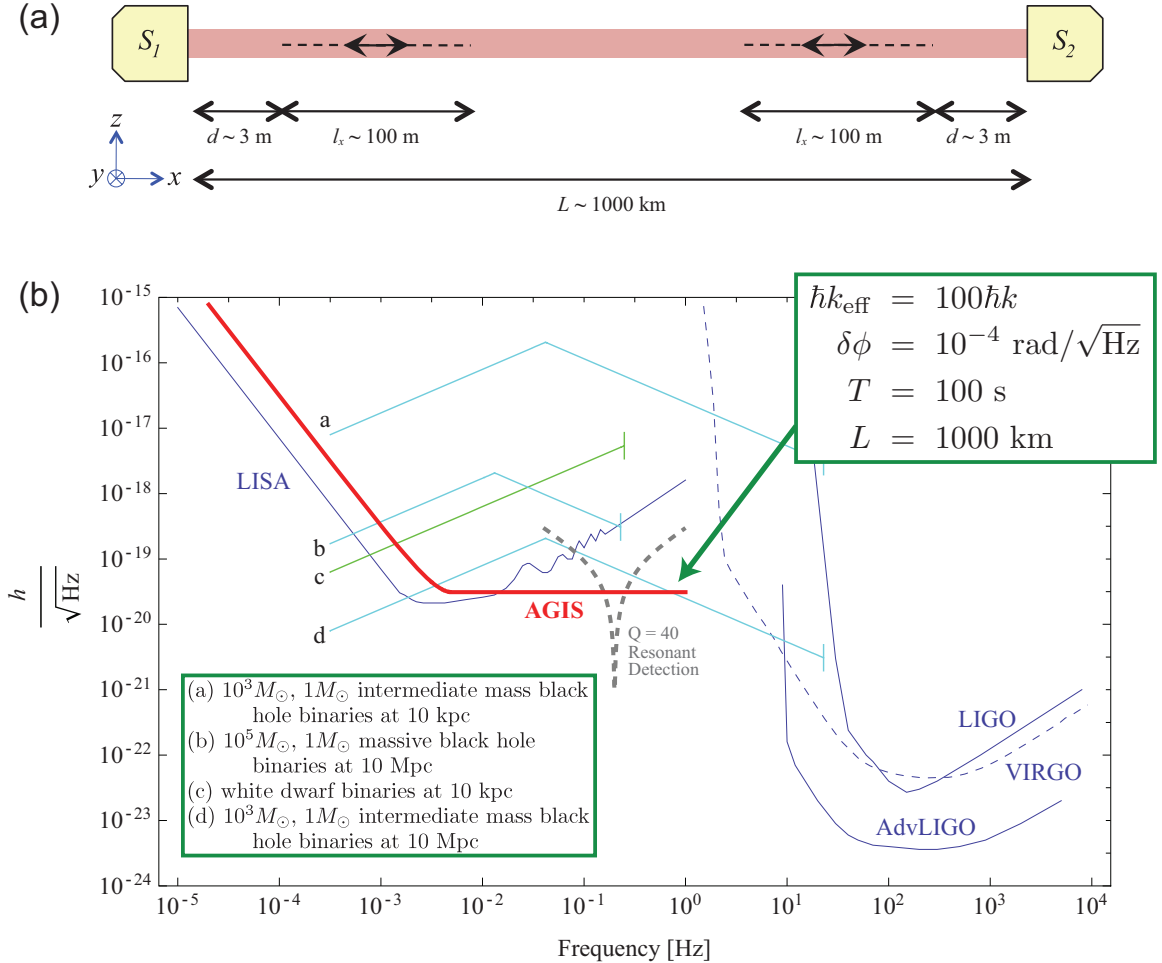


Figure 1.3: (a) Schematic of a single-axis AGIS configuration with two atom interferometers operated along a common baseline by lasers emitted from a pair of satellites. (b) AGIS gravitational wave strain sensitivity for the parameters indicated. Singularities arising from zeros of the differential phase shift (Equation 1.14) at $\omega = 2\pi n/T$ for integer n are removed by averaging the sensitivity over varied interrogation times T . The sensitivity curves of several other current or proposed experiments are also shown, as are the expected signals from binary inspirals at various distances. Adapted and updated from [45].

wave detector designs by replacing the macroscopic proof masses with ultracold atoms [18, 23, 45–47]. A common technological challenge for all of the conventional detectors is isolating the proof masses from environmental disturbances. This requires careful suspension of the proof masses on Earth or drag-free flight for a satellite mission [48]. Ultracold neutral atoms circumvent some of these challenges. They can be observed in free fall in Earth-based detectors, and they can be moved away from their parent satellites in space-based detectors. Furthermore an Atomic Gravitational wave Interferometric Sensor (AGIS) can be designed with less sensitivity to laser phase noise, allowing for a simpler single axis instrument [18, 47]. In general, an AGIS could yield similar sensitivity to a conventional interferometer at reduced cost.

Figure 1.3(a) presents a schematic of an AGIS in space. Two atom interferometers are separated by a long baseline L and manipulated by common lasers originating from opposing satellites (which also emit the atoms prior to measurement). For a three-pulse sequence, the differential phase shift between the two interferometers is [46]

$$\Delta\phi_{\text{tot}} = 2k_{\text{eff}}hL \sin^2\left(\frac{\omega T}{2}\right) \sin(\phi_0) \quad (1.14)$$

where h , ω , and ϕ_0 are the strain, frequency, and phase of the gravitational wave, and the atom interferometers have an interrogation time T and momentum splitting $\hbar k_{\text{eff}}$. The interferometer pair forms a gravity gradiometer, sensitive to the gravitational wave strain.²⁰ For a shot-noise-limited phase sensitivity $\delta\phi$, the differential phase shift yields a gravitational wave strain sensitivity, as plotted in Figure 1.3(b) for the parameters indicated.

To reach this shot-noise-limited strain sensitivity, many systematic effects must be mitigated. As with the equivalence principle test (Section 1.2.1), phase errors can arise from magnetic fields, gravity gradients, rotations, laser wavefront errors, etc. We have studied these effects in detail in [23, 45, 47], which I will not repeat here. Many of the experiments carried out in the Stanford 10 m atom drop tower can be viewed as developing the technology relevant to an AGIS mission.

²⁰Alternatively, the phase shift can be viewed as a clock comparison between the time kept by the lasers' phase evolution and the atoms' own internal clocks. The spacetime strain of the gravitational wave changes the light travel time between the atom and the laser [46].

1.3 Macroscopic Quantum Mechanics

Long-baseline atom interferometry also tests quantum mechanics at macroscopic scales.²¹ The maximum separation between the two arms of the interferometer (Figure 1.2) occurs at time T , and is

$$\Delta z = \frac{\hbar k_{\text{eff}}}{m} T \quad (1.15)$$

For a $2\hbar k$ ^{87}Rb interferometer with $T = 1.15$ s, $\Delta z = 1.4$ cm. Each atom is split by 1.4 cm before being brought back together and interfered. The atom is also held apart for a macroscopic time $2T = 2.3$ s before being interfered. In Chapter 6, I show that we have demonstrated interference with $\hbar k_{\text{eff}} = 12\hbar k$. This yields a wavepacket separation of 8.2 cm. These large superposition states probe quantum coherence at macroscopic scales.

Many theories attempt to explain why we don't observe macroscopic systems in quantum superposition states (why we don't see Schrödinger's cat in two places at once) [49, 50]. In general, these theories explain a loss of coherence or collapse of the wavefunction at large scales. For example, continuous spontaneous localization theories predict a small, but finite rate for particle wavefunctions to collapse [51]. For a macroscopic composite system, this effect adds up and is large enough that superposition states cannot endure. Other collapse theories predict a loss of coherence resulting from gravitational self-interaction [52]. A quantum foam, or inherent graininess of spacetime, could also destroy large-scale coherence [53].

A variety of experiments have created or propose to create large superposition states. These include supercurrents in SQUIDs, photon entanglement with micromirror resonators, atom and neutron interferometers, and Talbot-Lau interferometers with molecules or molecular clusters. Most of these experiments can be coarsely characterized by three parameters: the mass of the composite particle M_{comp} , the observed coherence time T_{sup} , and the separation length scale Δx_{sup} (the size of the

²¹I emphasize that the atom interferometers discussed here are not testing quantum gravity, as is sometimes hinted in the literature. Nevertheless, large quantum superposition states are formed during the gravity measurements.

composite particle σ_{comp} is also relevant). These parameters can vary by several orders of magnitude for different experiments [54].

In [55], the authors describe a minimal modification to quantum mechanics that facilitates comparisons between these diverse experiments.²² Within this framework, experimentally observed macroscopic superpositions can be referenced to hypothetical superpositions created with a single electron. For instance the observation of interference with contrast f in an experiment with $(M_{\text{comp}}, T_{\text{sup}}, \Delta x_{\text{sup}}, \sigma_{\text{comp}})$ sets a lower limit on the coherence time τ_e for an electron in a superposition state of a given length scale \hbar/σ_q .

This allows for the generation of exclusion curves for macroscopicity, as shown in Figure 1.4 for several completed or proposed experiments. Constraints from the Stanford 10 m atom interferometer are also shown. In general, the maximum value of excluded τ_e scales as $|\frac{1}{\ln f}| M_{\text{comp}}^2 T_{\text{sup}}$.²³ Above $\hbar/\sigma_q \sim \Delta x_{\text{sup}}$, the exclusion curve rolls off because these length scales have not been explored by the superposition state. Below $\hbar/\sigma_q \sim \sigma_{\text{comp}}$, the curve rolls off because only a fraction of the composite particle's mass contributes to the decay of coherence.

The modification to quantum mechanics proposed in [55] also yields a fundamental diffusion effect (see also Appendix A and [56]). As a result, a free gas of particles experiences spontaneous heating, with a rate governed by (Eq. A.7 and [55])²⁴

$$\left(\frac{M_{\text{comp}}}{m_e}\right)^2 \frac{\sigma_q^2}{2M_{\text{comp}}\tau_e} < \frac{1}{2}k_B\partial_t\mathcal{T} \quad (1.16)$$

where m_e is the electron mass, and \mathcal{T} is the temperature of the gas. Thus, the precision

²²A linear modification is added to the von Neumann equation for the time-evolution of the density matrix: $\partial_t\rho = \frac{1}{i\hbar}[H, \rho] + \mathcal{L}\rho$. Assuming Galilean invariance, exchange symmetry, the bystander criterion, and center-of-mass scale invariance, it is shown that $\mathcal{L}\rho = \frac{1}{\tau}[\int d^3s d^3q g(s, q) W_1(\mathbf{s}, \mathbf{q})\rho W_1^\dagger(\mathbf{s}, \mathbf{q}) - \rho]$ where W_1 is a Weyl translation operator, $1/\tau$ is the classicalization rate, and g is a classicalizing phase space distribution that can be taken to be Gaussian with position and momentum widths σ_s and σ_q . Experimental contrast is reduced after evolution for time t by the factor $R_t = \exp[\frac{1}{\tau} \int_0^t dt' \tilde{g}(\mathbf{r} - \frac{\mathbf{p}}{m}t', \mathbf{p}) - t]$. (σ_s usually contributes negligibly, and $\sigma_s = 20$ pm for all curves in Figure 1.4.) For details, see [54].

²³In [55], the authors further define a single macroscopicity parameter for an experiment based on this maximal value. This removes spatial information that could be relevant to a collapse theory.

²⁴I give a 1D temperature constraint. Note that in the context of the heating rate limit in Eq. 1.16, the *effective* temperature, not a thermodynamic temperature, is the appropriate metric.

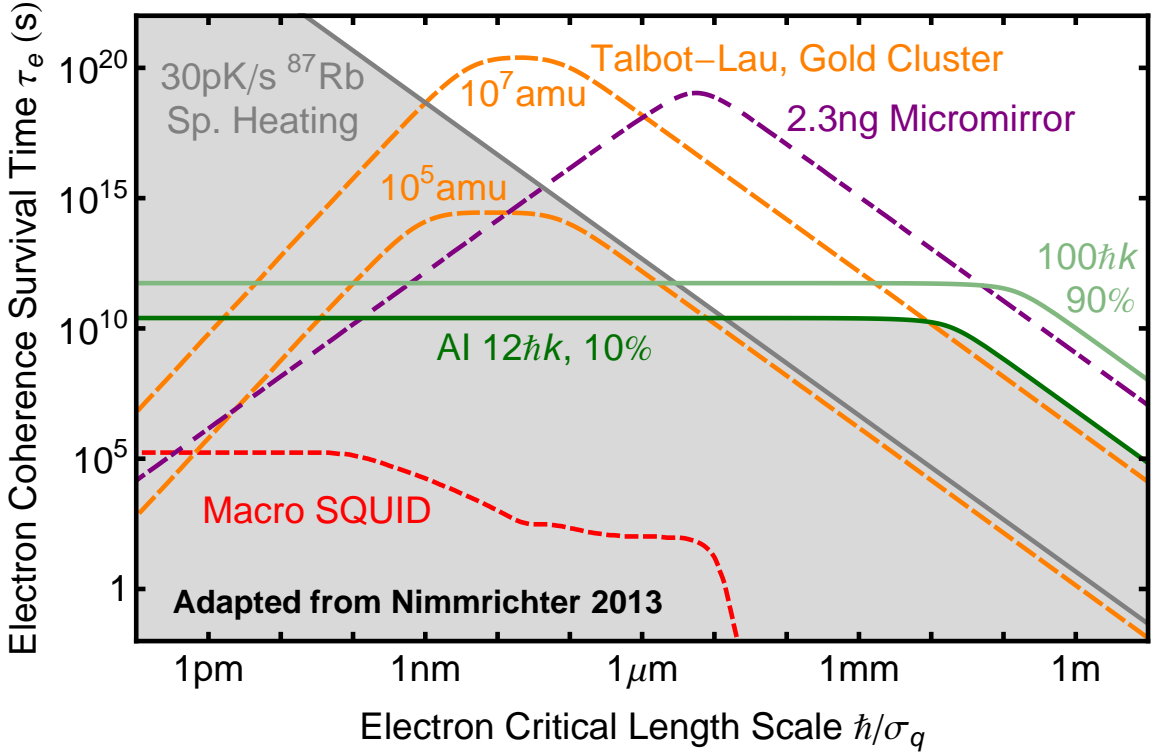


Figure 1.4: Exclusion plots for decoherence at macroscopic scales for the minimal modification to quantum mechanics proposed in [55]. For a given experiment, a point on the curve indicates that an electron superposition state of length scale \hbar/σ_q will survive for at least time τ_e . The gold cluster (orange, dashed), micromirror (purple, dot-dashed), and SQUID (red, dotted) curves are taken from [55] (see also the references therein). The gold cluster and micromirror curves correspond to proposed experiments. The gray (solid) curve corresponds to the heating-rate limit set in Chapter 5 and the dark green (solid) curve corresponds to the $12\hbar k$ atom interferometer discussed in Chapter 6. Together, these results rule out the light-gray shaded region. The light green (solid) curve corresponds to an improved $100\hbar k$ atom interferometer with 90% contrast. [Fig. 6.2(a) also presents a $2\hbar k$ interferometer with 90% contrast, not shown here. This result matches the $100\hbar k$ curve for $\hbar/\sigma_q \lesssim 1$ cm and it is only slightly below the $12\hbar k$ curve for $\hbar/\sigma_q \gtrsim 1$ cm. Thus, it rules out a small additional piece of the parameter space.]

temperature measurement in Chapter 5 yields an excluded region in Figure 1.4.

Many of the macroscopic decoherence theories discussed above conform to the minimal modification to quantum mechanics discussed in [55]. Thus, the exclusion curves in Figure 1.4 are not only useful for comparing different experiments, but also show how experimental results could constrain classicalizing decoherence theories. This would improve our understanding of quantum mechanics in macroscopic regimes.

1.4 Organization of this Thesis

Chapter 1 has presented in brief the scientific motivation and theoretical background for long-baseline atom interferometry in the Stanford 10 m drop tower. The remainder of the thesis is organized as follows. Chapter 2 describes the experimental apparatus and methods that are common throughout the thesis. The remaining chapters present experimental results that differ primarily in how the atoms are manipulated while they are in free fall in the 10 m tower.

In Chapter 3, $2\hbar k$ atom interferometry is demonstrated with a record interrogation time of $2T = 2.3$ s. The interferometer is configured as a precision accelerometer and gyroscope, and uses point source interferometry (PSI). Chapter 4 expands upon these results with a phase shear readout (PSR) technique, in which phase gradients are applied across the atom cloud to facilitate precision measurements. Chapter 5 is an interlude from interferometry, in which matter-wave lensing techniques are presented that allow atom cooling to effective temperatures below 100 pK. Finally, in Chapter 6, large momentum transfer (LMT) atom optics are used to enhance the interferometer sensitivity and create quantum superposition states with wavepacket separations up to 8.2 cm.

Collaborators and Prior Publication of Material in this Thesis

Section 1.2.3 above draws from [45] and [47] and covers work carried out in collaboration with Jason M. Hogan, David M. S. Johnson, Susannah Dickerson, Tim Kovachy, Sheng-wey Chiow, Peter W. Graham, Mark A. Kasevich, Babak Saif, Surjeet Rajendran, Philippe Bouyer, Bernard D. Seery, Lee Feinberg, and Ritva Keski-Kuha. Chapter 3

is adapted from [57] and covers work carried out in collaboration primarily with Susannah Dickerson, Jason Hogan, David Johnson, and Mark Kasevich.²⁵ Chapter 4 is adapted from [58] and covers work carried out in collaboration primarily with Susannah Dickerson, Jason Hogan, David Johnson, and Mark Kasevich.²⁶ Chapter 5, Appendix A, and Fig. 1.4 are adapted from [59] and [60] and cover work carried out in collaboration primarily with Tim Kovachy, Jason Hogan, Susannah Dickerson, Christine Donnelly, Chris Overstreet, and Mark Kasevich.²⁷ Chapter 6 covers ongoing work carried out in collaboration primarily with Sheng-wey Chiow, Susannah Dickerson, Christine Donnelly, Jason Hogan, Mark Kasevich, Tim Kovachy, and Chris Overstreet.²⁸

While I attempt to tell a full story, this thesis is a continuation of of the work presented in the theses of Jason Hogan [20] and David Johnson [63].²⁹ Especially in Chapter 2, I focus on documenting changes without excessive overlap with these prior theses, or with the contemporaneous thesis of Susannah Dickerson [29].

²⁵With contributions to the apparatus from, and valuable discussions with, Tim Kovachy, Sheng-wey Chiow, Jan Rudolph, and Philippe Bouyer.

²⁶With contributions to the apparatus from, and valuable discussions with, Philippe Bouyer, Sheng-wey Chiow, Tim Kovachy, and Jan Rudolph.

²⁷With contributions to the apparatus from, and valuable discussions with, Sheng-wey Chiow, Naceur Gaaloul, and Jan Rudolph.

²⁸Other publications to which I have contributed during my Ph.D. that are not generally included in this thesis are [61] and [62].

²⁹[20] in particular is a great reference for interferometer phase shifts and details on the core of the apparatus discussed in this thesis.

Chapter 2

Experimental Apparatus and Methods

Most of the experimental apparatus is common throughout this thesis, though the applications vary somewhat in the ensuing chapters. In this chapter, I will describe the common features as much as possible, leaving some details for Chapters 3-6. While the apparatus has been designed to operate with both ^{85}Rb and ^{87}Rb for tests of the equivalence principle, this thesis focuses on results obtained with ^{87}Rb alone. Nevertheless, some hardware and design constraints relevant to dual species operation will be mentioned.

2.1 Experimental Overview

Fundamentally, an experimental measurement consists of *cooling* (2.3), *launch* (2.4), *free fall* (2.2), and *detection* (2.5). All of these steps occur when the Rb atoms are in a given section of the 10 m atomic fountain apparatus in Fig. 2.1. Each measurement is destructive, yielding an image of the atom cloud while simultaneously obliterating it. A scientific campaign therefore consists of a sequence of such measurements, either with the same experimental parameters to build up statistics, or with varied parameters to explore the dependency. Each measurement currently takes \sim 30 s to complete

(including data initialization and readout).¹ A full timing diagram appears in Fig. 2.2.

During the *cooling* stage, $10^5\text{-}10^6$ ^{87}Rb atoms are collected at the bottom of the tower and cooled to 1-10 nK. This stage is needed to generate a cloud of atoms that will stay sufficiently well-localized over the course of an entire measurement. At room temperature, the atoms in a gas of Rb move at speeds of hundreds of meters per second and would collide with the walls of our vacuum chamber long before falling back to the bottom. The cooling process relies on techniques that have been established in the atomic physics community over the past three decades: laser cooling and evaporative cooling, both of which yielded Nobel prizes [65–69]. To reach nanokelvin temperatures, we added more recently developed matter-wave lensing techniques (Chapter 5).

We *launch* the cold atoms vertically, with a typical launch velocity of $v_L \sim 13$ m/s. Launching the atoms from the bottom (as opposed to dropping them from the top) doubles the free-fall time of the apparatus, quadrupling its sensitivity (Eq. 1.11). Launching also allows for operation with different initial atom velocities. This is beneficial for running simultaneous interferometers at different heights (a gradiometer), for exploring velocity-sensitive phase shifts, and for other diagnostics. To launch the atoms, we trap them in a vertical optical lattice with a pair of lasers and then chirp one laser’s frequency to accelerate the lattice in the lab frame. For example, an acceleration of $100g$ applied for 13 ms accelerates the atoms to 13 m/s over 8 cm.

After launch, the atoms are in *free fall* for up to 2.8 s. During this time, interferometry and/or further cooling are performed (as described in Chapters 3-6). During most of their flight, the atoms are in a pristine 8.5 m tall interferometer region. To meet the demands of high-precision atom interferometry, this region is at ultrahigh vacuum, is magnetically shielded, and has a uniform mass distribution to reduce gravity gradients. Since the interferometer region is the heart of the apparatus and informs the design of other components, I will discuss it first in Section 2.2.

Detection occurs once the atoms fall back to the bottom of tower. An optical pulse excites the atoms, which reradiate into 4π via spontaneous emission. Two perpendicular imaging systems, consisting of CCD cameras and high-numerical-aperture lenses,

¹Several techniques could improve upon this experimental repetition rate, including reduced atom preparation times, interleaved measurements with concurrent interferometers [64], and increased data transfer rates (including CCD readout). The system has not yet been fully optimized.

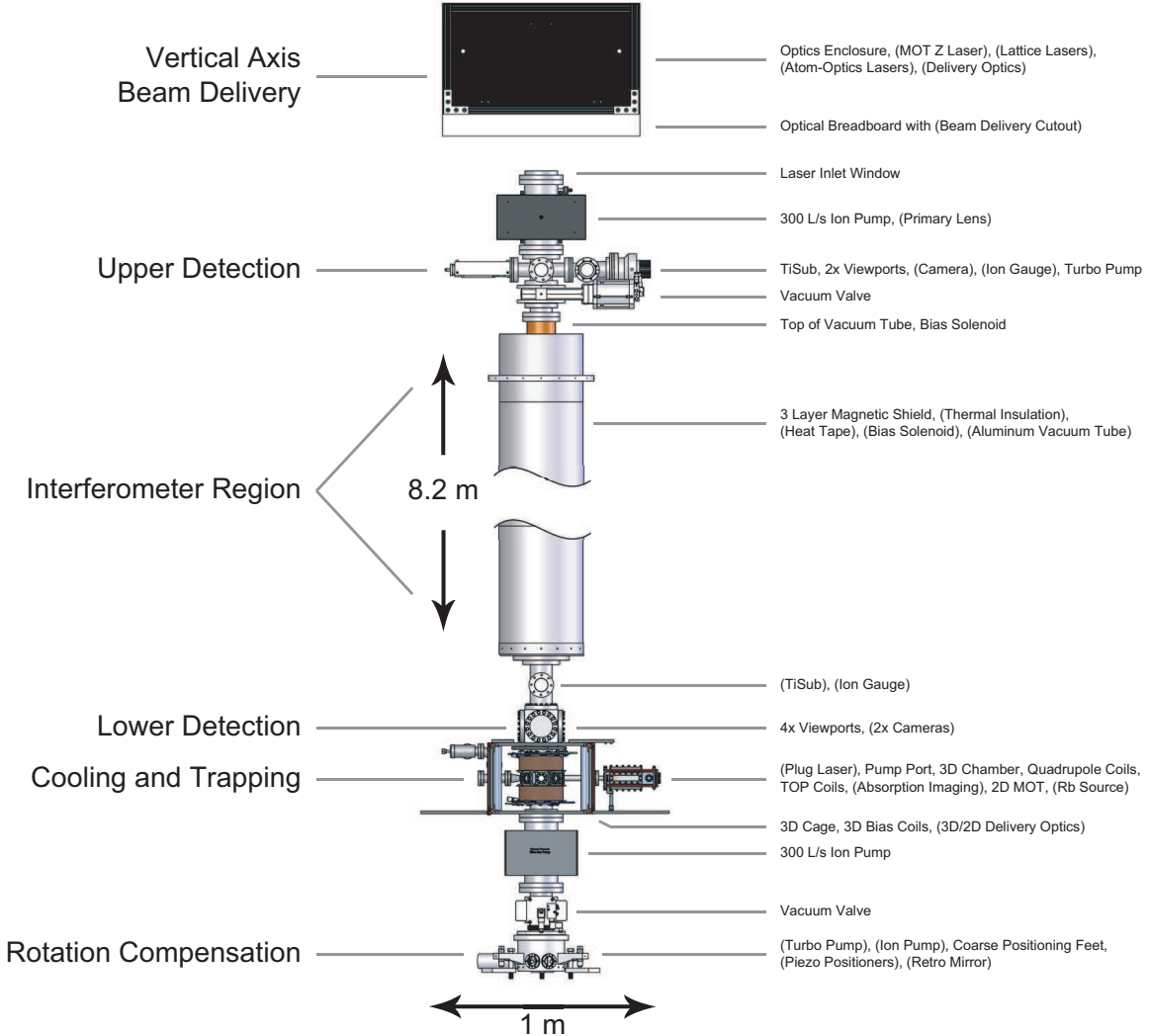


Figure 2.1: Schematic of the full 10 m fountain apparatus. Six primary regions are identified on the left; detailed components are identified on the right. If multiple components are at the same height, they are listed as they appear in the figure from left to right. Components in parentheses are either not included in the CAD model or are obstructed by other components.

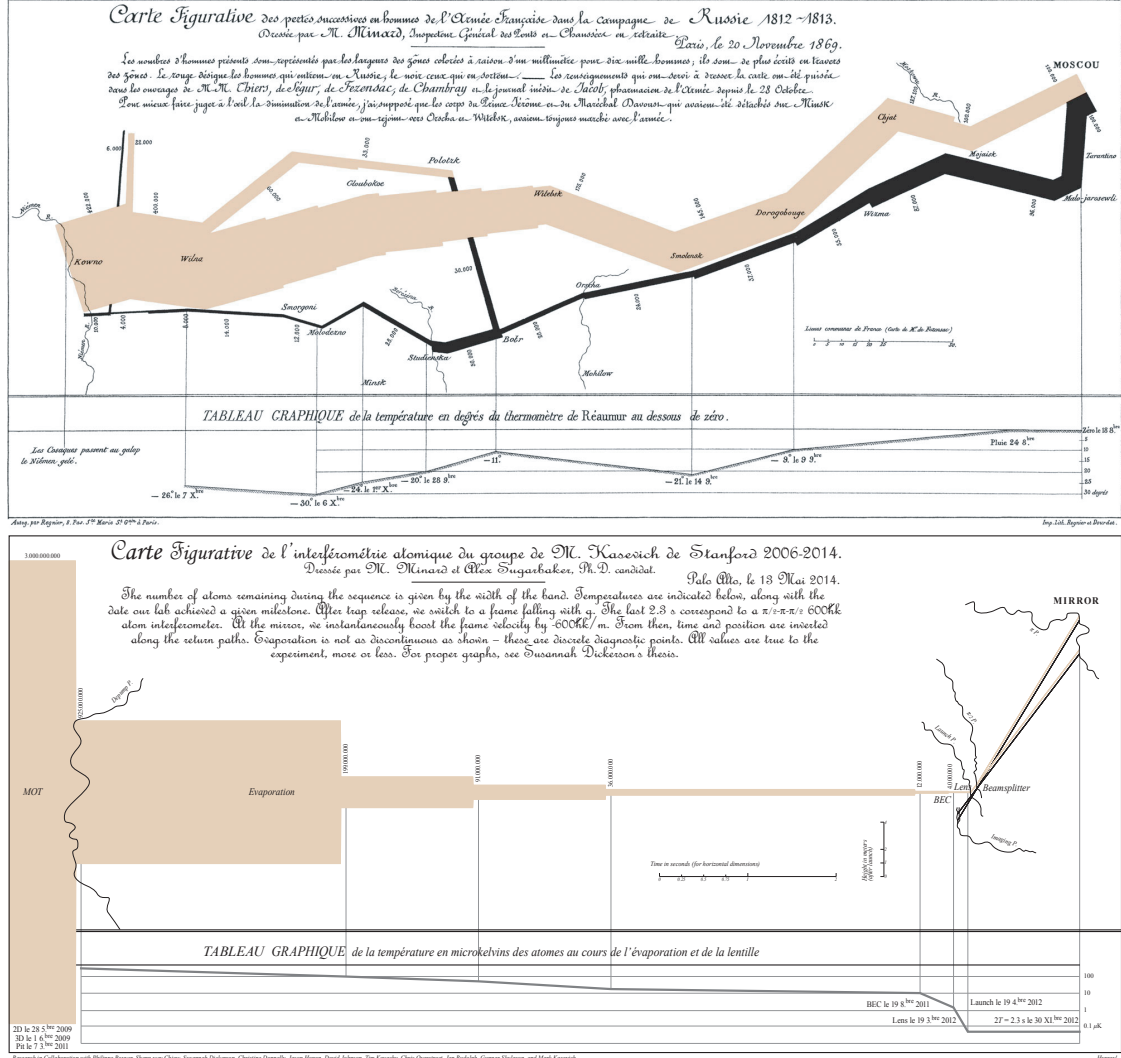


Figure 2.2: *Lower panel:* Full timing diagram for a single experimental shot, including magneto-optical trapping, evaporation, magnetic lensing, and atom interferometry. The momentum splitting of the atom optics is greatly exaggerated for clarity. The evaporation and lensing sequence corresponds to our ~ 50 nK source [see for instance Fig. 3.3(b) and Fig. 5.5]. Further details are explained in the in-figure caption. See [29] for conventional timing diagrams. *Upper panel:* Charles Joseph Minard's infamous flow map of Napoleon's failed Russian campaign of 1812. A comparison between the upper and lower panels highlights the catastrophic loss of atoms during evaporation and the ultracold temperatures reached in our lab. It is also apparent that embarking upon a Ph.D. thesis is at least as foolhardy as attempting to conquer Russia in winter.

collect the scattered light. The imaging systems are spatially resolved. This facilitates the measurement of time-of-flight temperatures (Chapter 5), the normalization of interferometer output port atom population ratios (Section 3.3.1), and the observation of spatially varying interferometer phases (Chapters 3 and 4).

Each measurement (or sequence of measurements) is orchestrated by a sophisticated computer control system. At the core of this system is a custom FPGA timing system with nanosecond timing jitter. It has ~ 100 I/O channels to measure and control laser intensities/frequencies, magnetic coil currents, component temperatures, etc.² Other devices with relaxed timing constraints or external trigger inputs are controlled with ~ 5 standard personal computers throughout the lab. All of the computer hardware is coordinated by a suite of custom software, the Stanford Timing Interface (STI). A centralized server pushes timing events to all of the computers, where programs interface with individual devices. In turn, experimentalists interact with the server through portable client software. Further details on the FPGA timing system and the STI can be found in [20, 63].

2.2 Interferometer Region (Free Fall)

The interferometer region constitutes the majority of the apparatus's 10 m height, and is the primary feature that distinguishes it from similar previous experiments. The apparatus is in an 8 m deep pit in the basement of Stanford's Varian Physics Building (the top of the apparatus sticks up out of the pit, see Fig. 2.3). Most of the components in Fig. 2.1 are supported by an 80/20 tower structure bolted to the pit walls. The interferometer region is designed to provide a uniform environment for precision atom interferometry. This includes an ultrahigh vacuum system (Section 2.2.1) and magnetic field control (Section 2.2.2). The interferometer region also conceptually includes the atom-optics lasers (Section 2.2.3) and the two most critical optical elements for the delivery of the atom-optics lasers: the primary telescope lens (Section 2.2.4) and the

²A typical configuration of these channels is: 8 direct digital synthesis (DDS), 2 differential fast analog in, 24 digital out, 40 slow analog out, and 4 fast analog out, but this can be varied. Two such systems can be combined, with a slave clocked by a master.

retroreflection mirror (Section 2.2.5).

2.2.1 Vacuum System

A high quality vacuum environment is essential throughout the chamber to reduce collisions of the Rb atoms with background gas. Typically, the momentum imparted to the Rb atom in such a collision is enough to remove it from the ensemble, so this is not a systematic effect on a phase measurement. Nevertheless, atom loss constitutes a loss of signal. A vacuum environment of $p = 10^{-10}$ Torr increases the mean collision time to $\tau_c \gtrsim 100$ s, much longer than the duration of the experimental sequence $\tau \sim 20$ s.³

To achieve pressures $\lesssim 10^{-10}$ Torr, we use standard ultrahigh vacuum (UHV) techniques, scaled up to 10 m. An 8.84 m long cylindrical vacuum tube spans the majority of the length of the vacuum system. A continuous tube was selected to reduce spurious gravity inhomogeneities, and the tube is made of non-magnetic aluminum. The inner diameter of the tube is 10 cm. A large diameter is critical in that it allows larger Gaussian laser beams to propagate along its length without aperture diffraction effects (Section 2.2.4). A larger tube also has a reduced gravitational impact on the atoms traveling on-axis, and its vacuum conductance is greater. However, the larger aperture increases the cost and technical challenges of magnetically shielding the interferometer region (Section 2.2.2) and applying large dynamic magnetic fields in the atom source (Section 2.3).

The primary vacuum pumps are a pair of 300 L/s ion pumps at the top and bottom of the tower (Fig. 2.1). Initial pumping from atmosphere was achieved with diaphragm, scroll, and turbo pumps that are valved-off and deactivated during normal operation (for improved base pressure and reduced vibrations). To reduce the outgassing rate of the aluminum tube, it was baked to ~ 175 °C for 3 days using heat tape permanently installed inside the magnetic shield [20].

³Assuming a background gas of N₂, $\tau_c = (n\sigma\bar{v})^{-1}$, where n and \bar{v} are the density and RMS velocity of N₂ at room temperature at pressure p , and $\sigma = 3.5 \times 10^{-14}$ cm³ is the Rb-N₂ collision cross section [70].



Figure 2.3: Photograph of the full apparatus installed in the pit. For the majority of the length, the primary features visible are the outer layer of the magnetic shield and the 80/20 support structure. See also Fig. B.1.

Titanium Sublimation

Limited conductance reduces the effective pumping rate at the center of the vacuum tube. We therefore designed a system to spray titanium into the tube. Titanium is a strong getter, meaning that many components of the residual background gas will react with it to form inert compounds stuck to the chamber walls. This makes titanium sublimation pumps (TSP or TiSub) common in UHV systems. We mount commercial TiSub cartridges in vacuum translation stages at the top and bottom of the vacuum tube (Fig. 2.4). When inserted, the TiSub filaments have a clear line-of-sight into the tube (when removed, they do not obstruct the optical beamline). A current of ~ 45 A applied through a titanium filament in the cartridge causes enough heating to induce sublimation, ejecting titanium atoms into the chamber. Integrated shields (in conjunction with vacuum valves) block the titanium from reaching the in-vacuum optics (Sections 2.2.4 and 2.2.5) and vacuum viewports.

It is difficult to predict the exact current and duration at which to drive the titanium filament. Background pressure, filament geometry, and thermal insulation all affect the current needed to induce sublimation. Also, the chamber geometry and the pressure and composition of the background gas influence the amount of sublimated titanium needed, as well as how often it should be replenished. In practice, we heat the filaments until the pressure spikes and then look for any improvements in base pressure once the system cools back to ambient.

After sublimating with both the upper and lower TiSub systems (upper: 46 A for 4×5 minutes; lower: 43 A for 2×15 minutes),⁴ we observed a drop in pressure from 5.8×10^{-11} Torr to 2.6×10^{-11} Torr as measured with an ion gauge at the top and a drop in pressure from 1.0×10^{-10} Torr to 4.0×10^{-11} Torr as measured with an ion gauge at the bottom. The pressure reduction in the middle of the tube could be greater than the factor of 2 observed at the top and bottom, but there is no gauge at the middle to measure this. However, by adjusting the height to which we launch the atoms we can get a rough sense of loss rates. Since the atoms spend substantially

⁴In smaller systems, one short heating cycle is usually sufficient. We find that the high-current vacuum feedthroughs overheat (and can open vacuum leaks) if run for longer than $\sim 5\text{-}10$ min. We therefore sublimate in multiple short bursts, letting the system cool down between heating cycles.

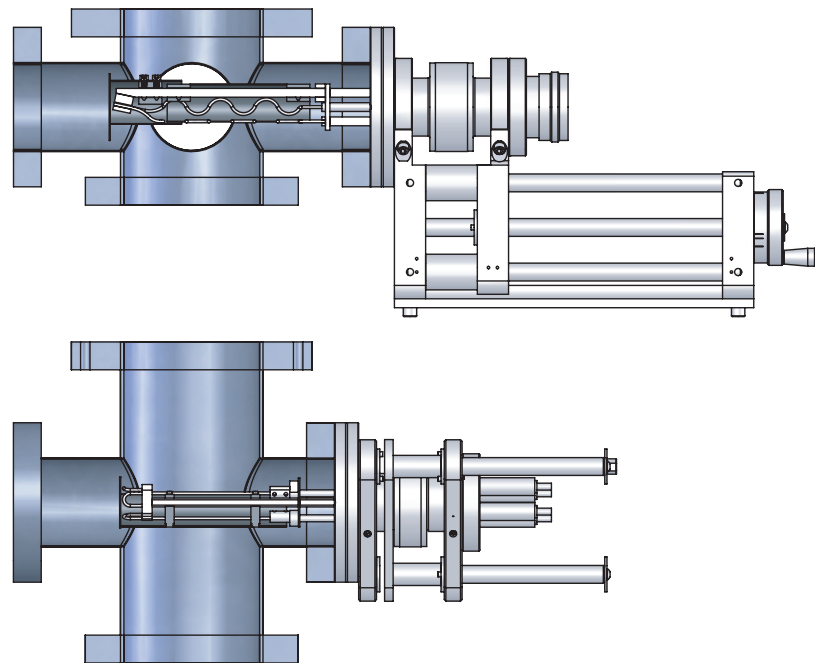


Figure 2.4: Titanium sublimation system. The upper and lower vacuum crosses are attached to the top and bottom of the tower, respectively (Fig. 2.1). Hood structures prevent the titanium sublimated from the filaments from hitting windows and in-vacuum optics. The translation stages shown on the right of the figure are used to retract the TiSub cartridges from the optical beamline. The upper (lower) TiSub system consists of a Varian TSP 916-0017 (Lesker TSPH4) cartridge with Varian style (Lesker PE style) filaments on a McAllister Technical Services BLT27S-06 (BLT026-4) translation stage.

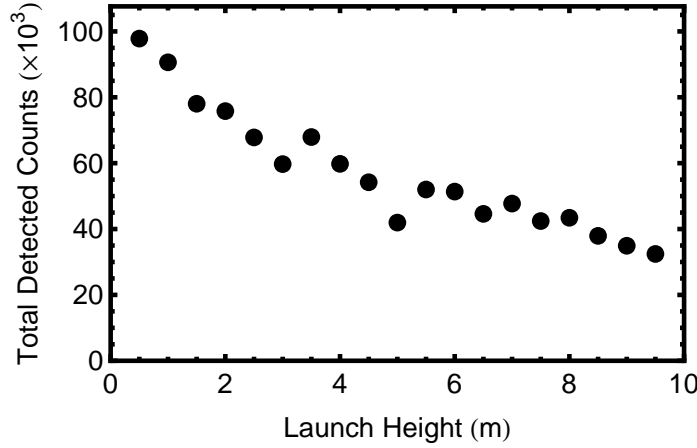


Figure 2.5: Atom number detected (at the bottom of the tower) vs. launch height. Each point is the average of 3 separate experimental trials. A fluorescence imaging pulse 5 ms in duration yields the indicated number of total counts on a CCD camera (Section 2.5). More than 50% of the atoms are lost for an 8.5 m launch. This could result from imperfect vacuum or from Landau-Zener tunneling and spontaneous emission during the launch itself (Section 2.4.3). Note that a loss rate of 50% is inconsistent with the predictions of Fig. 2.19 (the lattice detuning here is ~ 90 GHz). It is possible that the lattice intensity and alignment were not perfectly optimized, which could, for instance, substantially increase losses to Landau-Zener tunneling.

longer at the turning point of their trajectory, we might expect increased loss rates for half-height launches. Figure 2.5 shows the detected atom number as a function of launch height. The atom number decreases with launch height, but there is no substantial dip at the center.

2.2.2 Magnetic Shielding

The interferometer region must be an environment with well-controlled magnetic fields. Consider an equivalence principle test. Prior to an interferometric measurement, the Rb atoms are prepared in a first-order Zeeman insensitive $|m_F = 0\rangle$ state. Nevertheless, the second order Zeeman coefficient α is not zero, leading to a potential $U_B = \pm \frac{1}{2}\hbar\alpha B^2$.⁵

⁵ As in Eq. 1.6, the second-order Zeeman shift is negative for atoms in $|F = 1\rangle$ and positive for atoms in $|F = 2\rangle$. As a result, the magnetic field response is different for Raman interferometers (in which the internal state changes) and Bragg interferometers (in which the internal state does not

The second order coefficient is different for the two isotopes ($\alpha_{87} = 2\pi \times 575.15 \text{ Hz/G}^2$ and $\alpha_{85} = 2\pi \times 1293.98 \text{ Hz/G}^2$) [71, 72]. This results in a differential phase shift of [20]

$$-\left(\frac{\alpha_{85}}{m_{85}} - \frac{\alpha_{87}}{m_{87}}\right) \hbar k_{\text{eff}} B_0 (\partial_z B) T^2 \quad (2.1)$$

that depends on the bias field B_0 and the field gradient $\partial_z B$. To reduce magnetic-field induced differential phase shifts to the 10^{-15} level requires $\partial_z B \lesssim 3 \mu\text{G}/\text{m}$ for a bias field of $B_0 = 1 \text{ mG}$ [20]. A high performance magnetic shield and a bias solenoid were designed to create this magnetic field environment.

In the interferometer region, the measured vertical field gradient with no shielding is $\sim 30 \text{ mG/m}$ (Fig. 2.6). Thus a magnetic shield with a shielding ratio of $\sim 10^4$ along the vertical axis is desired to achieve $\partial_z B \lesssim 3 \mu\text{G}/\text{m}$. Our magnetic shield consists of three concentric cylinders of 0.050" thick μ -metal around the vacuum tube [62]. It reduces the ambient Earth field ($\sim 500 \text{ mG}$) to $420 \mu\text{G}$ (rms) in the axial direction (Fig. 2.6), and $(460, 730) \mu\text{G}$ (rms) in the two transverse directions. The shielding ratio is therefore $\sim 10^3$.⁶ Reaching the desired level for the equivalence principle will therefore likely require measuring the magnetic field *in situ*, which can be achieved by running short interferometers at various heights with $|m_F \neq 0\rangle$.

Figure 2.6 also highlights the importance of material uniformity for the magnetic shield. Originally, each of the shield layers consisted of 14 axial segments bolted together. With this design, substantial $\sim 100 \text{ mG}$ peaks were observed as the field leaked through the joints between segments. While several methods for improving the continuity at the gaps were attempted [62], the ultimate solution required welding the segments together and re-annealing them.⁷

change). The phase shift in Eq. 2.1 is the leading order term for a Bragg interferometer. Raman interferometers can have larger magnetic field responses [29]. However, for even N , these terms are suppressed for $2N\hbar k$ sequential Raman LMT sequences (Section 6.1), because the atoms are then in a single hyperfine ground state for most of the interferometer duration.

⁶For a long cylindrical shield, models assuming simple linear materials would predict a substantially lower axial shielding ratio of 8.0 for our shield (the larger transverse shielding ratio would be 4×10^5). However, μ -metal is hysteretic, and a degaussing procedure substantially improves performance. The dynamic axial shielding ratio is nevertheless substantially lower and is more consistent with the simple models [62].

⁷Re-annealing is necessary because the forming and welding processes apply stresses to the μ -metal and reduce its permeability.

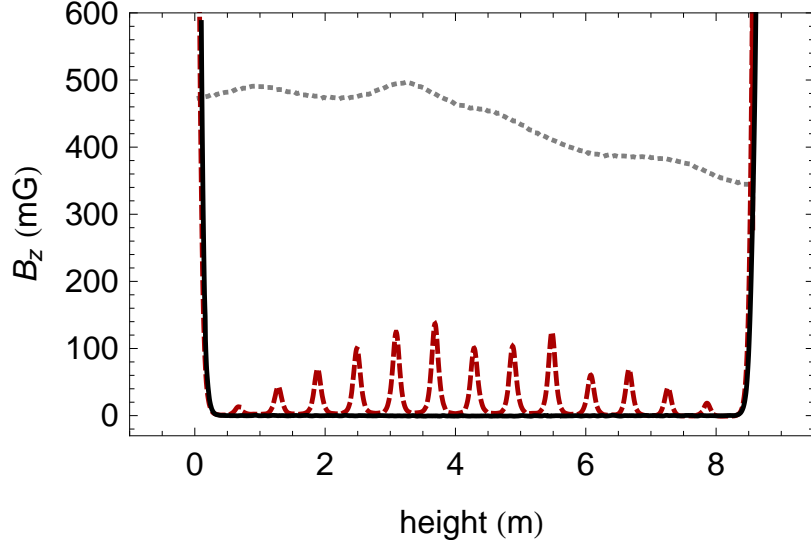


Figure 2.6: Measured axial magnetic field along the vacuum tube axis. The dotted gray curve is the ambient magnetic field measured before the shields were installed. The dashed red curve is the field with the segmented shields. The solid black curve is the field with the welded shields. From [62].

Equation 2.1 suggests keeping the magnitude of the magnetic field in the interferometer region as small as possible to minimize magnetically-induced phase shifts. However, a constant bias field B_0 is required to maintain the alignment of the atoms' spins, which would otherwise follow the stochastic field direction as the atoms moved through the tower. If B_0 is much greater than the residual field inside the magnetic shield, the polarization axis remains well-defined. We apply B_0 along the vertical axis with a solenoid wrapped around the vacuum tube. The solenoid has 3.44 turns/cm and is broken up into 11 segments along the tower, which can be driven independently (to compensate for field gradients). For the experiments in this thesis, we connect the segments in series and drive them with a 35 mA DC current, yielding a calculated $B_0 = 151$ mG.⁸

⁸This ignores fringe effects and the effect of the magnetic shield. For measured values, see [29]. We choose this value of B_0 so as to greatly exceed the residual field inside the shield (~ 500 μ G). Therefore, B_0 could be lowered somewhat, but would likely have to exceed $B_0 = 1$ mG, which was assumed following Eq. 2.1. This further constrains $\partial_z B$, or in turn the necessary precision of the *in situ* field measurement mentioned in the text.

2.2.3 Atom Optics Lasers

The interferometry region also supports the laser beams that perform the atom optics (beamsplitters, mirrors, and lenses). These beams propagate along the vertical axis through the center of the vacuum tube [see Fig. 2.7(a)]. Several other lasers share this axis, as will be discussed in subsequent sections, but the atom optics beams are the most critical. Fundamentally, we deliver light from above and retroreflect it off of a mirror at the bottom (Section 2.2.5). This provides the two counterpropagating beams for a Raman transition [Fig. 1.1(a)]. The beams must also be enlarged with a telescope (the primary telescope) prior to interacting with the atoms (Section 2.2.4).

Fundamental Requirements for the Atom Optics Lasers

The frequencies of the two atom-optics lasers (ω_1 and ω_2) are chosen so as to drive Raman transitions [Fig. 1.1(a) and Fig. 2.8]. They must account for the recoil energy corresponding to the momentum transfer of the multi-photon process, the Doppler shift in the frame moving with the atom's initial velocity \mathbf{v} , and the difference between the atom's initial and final internal energies. Specifically, at the two-photon Raman resonance, the frequency difference is [73, 74]

$$\omega_1 - \omega_2 = \frac{\hbar \mathbf{k}_{\text{eff}}^2}{2m} + \mathbf{k}_{\text{eff}} \cdot \mathbf{v} + (\omega_{|2\rangle}^a - \omega_{|1\rangle}^a), \quad (2.2)$$

where $\mathbf{k}_{\text{eff}} = \mathbf{k}_1 - \mathbf{k}_2$ (Eq. 1.1), $\hbar\omega_{|1\rangle}^a$ is the internal energy of an atom in state $|1\rangle$, and $\hbar\omega_{|2\rangle}^a$ is the internal energy of an atom in state $|2\rangle$. The ground state hyperfine splitting for ^{87}Rb is $(\omega_{|2\rangle}^a - \omega_{|1\rangle}^a) = 2\pi \times 6.8 \text{ GHz}$ [71].⁹

The atom optics lasers also need to have the appropriate single-beam intensity I and single-photon detuning Δ (Fig. 2.8) to drive high-Rabi-frequency Raman transitions without excessive loss from spontaneous emission. For a transition with a natural linewidth Γ and in the far-detuned limit ($\Delta \gg \Gamma$), the scattering rate due to

⁹Our laser systems can typically be adapted to drive Bragg transitions by removing this 6.8 GHz frequency shift, but that is not the focus of this thesis.

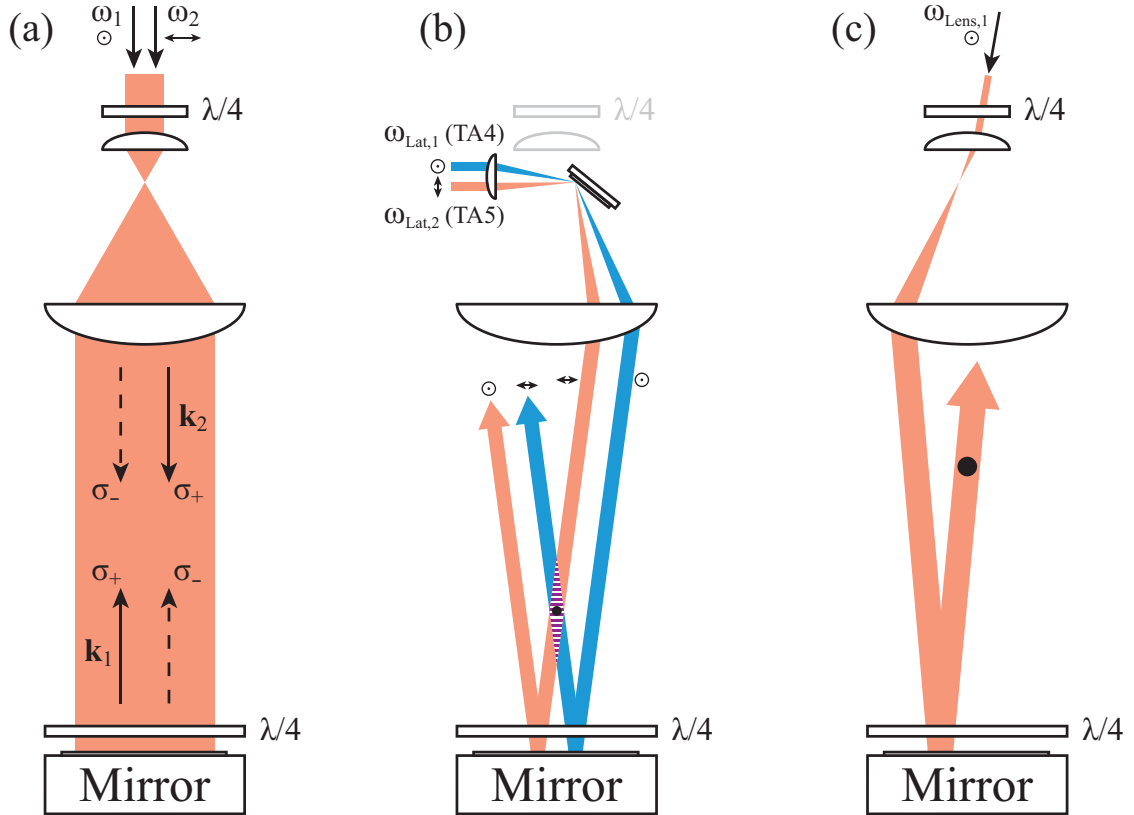


Figure 2.7: Vertical (z) axis laser beam delivery. The laser beams are launched from an optics box above the interferometer region (Fig. 2.14, not shown here), and retroreflect from a mirror at the bottom. The primary telescope (Section 2.2.4) at the top of the tower is also shown. (a) Large-diameter beams for the MOT and atom optics, in a $\sigma^+ - \sigma^+$ configuration. Adapted from [20]. (b) Lattice launch beams (Section 2.4). The divergence of the lattice beams is not shown for simplicity. They actually go through a focus near the retroreflection mirror. The polarizations indicated are idealized (but nearly correct prior to retroreflection). In actuality, the $\lambda/4$ at the bottom is not at 45° relative to the input polarization, and the retroreflected polarizations are rotated by 29° . (c) Optical dipole beam path used for atom lensing (Chapter 5, see also Fig. 5.1). A 750 mm lens is used to focus one of the atom optics beams to a $\sim 200 \mu\text{m}$ $1/e^2$ radial waist at the input lens to the primary telescope. This yields a 3.4 mm beam in the interferometer region that is nearly collimated.

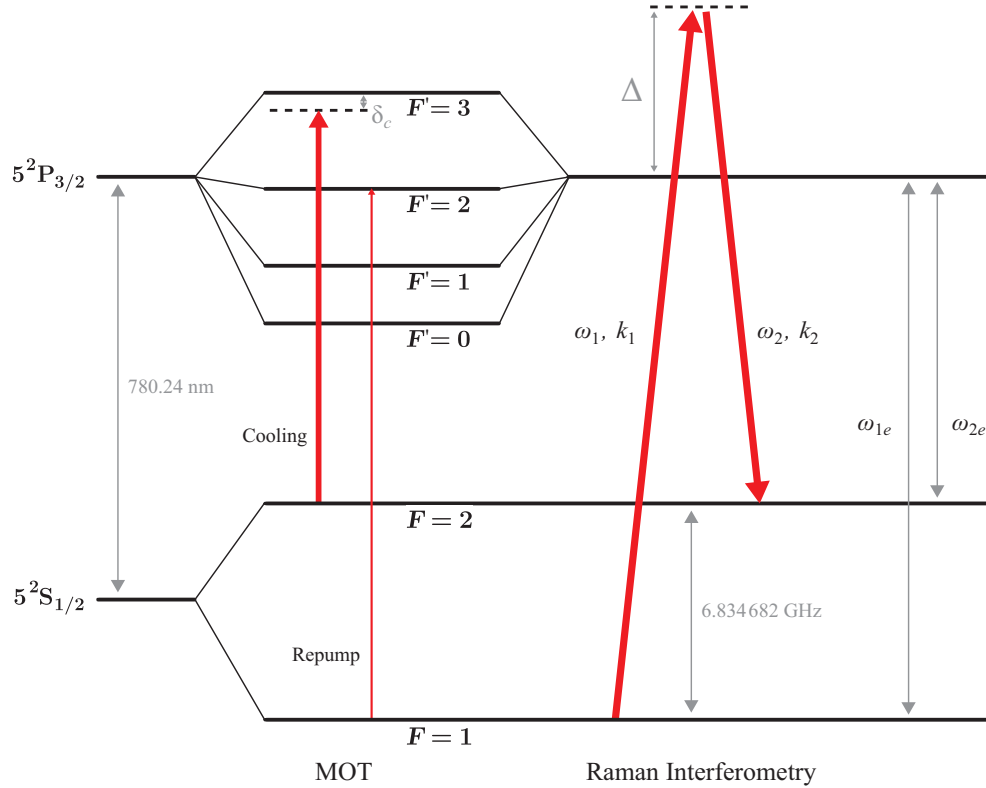


Figure 2.8: The D_2 line of ^{87}Rb . The cooling and repump transitions of the MOT are shown, as well as the two-photon Raman transition used for atom interferometry (see also Fig. 1.1). The detunings and relative sizes of the fine and hyperfine structures are not to scale and the Raman transition is shown in the limit where the single-photon detuning Δ is much greater than the hyperfine splitting of the F' manifold (~ 500 MHz). Further details on the level structure of Rb can be found in [71].

spontaneous emission is [71]

$$R_{\text{sc}} = \frac{\Gamma}{2} \frac{(I/I_{\text{sat}})}{(2\Delta/\Gamma)^2} \quad (\text{single beam, } \Delta \gg \Gamma) \quad (2.3)$$

where I_{sat} is the saturation intensity parameter, accounting for the polarization of the light. The effective two-photon Rabi frequency is [71, 73]

$$\Omega_{\text{eff}} \equiv \frac{\Omega_1 \Omega_2}{2\Delta} = \frac{1}{2\Delta} \sqrt{\frac{\Gamma^2}{2} \frac{I_1}{I_{\text{sat}}}} \sqrt{\frac{\Gamma^2}{2} \frac{I_2}{I_{\text{sat}}}} \approx \frac{\Gamma}{2} \frac{(I/I_{\text{sat}})}{(2\Delta/\Gamma)} \quad (2.4)$$

where I have assumed equal single-beam intensities $I \equiv I_1 \approx I_2$.

Consider a π pulse with duration $\delta t_\pi = \pi \Omega_{\text{eff}}^{-1}$ (Section 1.1.1). The fraction of atoms lost to spontaneous emission during the pulse from both Raman beam pairs¹⁰ is (using Eqs. 2.3 and 2.4)

$$\frac{-\delta N_a}{N_a} \approx 4R_{\text{sc}}\delta t_\pi = 4\pi \frac{R_{\text{sc}}}{\Omega_{\text{eff}}} = 2\pi \frac{\Gamma}{\Delta} \quad (\text{for } R_{\text{sc}}\delta t_\pi \ll 1) \quad (2.5)$$

where N_a is the number of atoms remaining and δN_a is the number of atoms lost during the interval δt_π . From Eq. 2.5 it is clear that the number of atoms lost due to spontaneous emission scales as $\frac{1}{\Delta}$.¹¹ This suggests increasing Δ to reduce losses, especially for LMT sequences (Chapter 6). However, Ω_{eff} also scales as $\frac{1}{\Delta}$, so without a compensating increase in intensity I , $\delta t_\pi = \pi \Omega_{\text{eff}}^{-1}$ becomes large.

Practically, it is desirable to maintain high Rabi frequencies ($\delta t_\pi \lesssim 100 \mu\text{s}$) for good transfer efficiency. For longer pulse durations, the velocity selectivity of the Raman transition becomes narrower than $\sim 10 \text{ nK}$,¹² a typical temperature for our atom

¹⁰In our retroreflection scheme [Fig. 2.7(a)], one pair of beams drives the transition. The second pair is Doppler detuned from resonance, but still contributes to spontaneous emission.

¹¹Similar results hold for a $\frac{\pi}{2}$ pulse and for LMT pulse sequences. In fact, for a $2N\hbar k$ sequential Raman Mach-Zehnder interferometer (Chapter 6), the total pulse area is equivalent to that of $4N - 2$ π pulses. The total number of atoms lost during the interferometer sequence due to spontaneous can then be found by multiplying the right-hand side of Eq. 2.5 by this factor and integrating [since $R_{\text{sc}}(4N - 2)\delta t_\pi \gtrsim 1$ for large N].

¹²The width of the velocity-selective Raman transition is $\Delta\omega \sim \frac{1}{\delta t_\pi}$ [73]. This yields a velocity acceptance $v_{\text{Raman}} \sim \frac{\Delta\omega}{k}$, corresponding to temperature $\frac{1}{2}k_B T_{\text{Raman}} = \frac{1}{2}mv_{\text{Raman}}^2$. We often intentionally apply a velocity-selective Raman transition (with $\delta t_\pi \gtrsim 100 \mu\text{s}$) to remove (vertically) hotter

source (Section 2.3.5). This reduces the transfer efficiency of the pulse, and in turn the contrast of the interferometer. Similarly, the broader linewidth of shorter pulses makes them more immune to other sources of inhomogeneous broadening. Finally, high Rabi frequencies facilitate the short pulse limit ($\delta t_\pi \ll T$) in calculating the interferometer phase (Section 1.1.2). Since large beams are needed to minimize spatial intensity variations (Section 2.2.4), high Rabi frequencies require high-power lasers.

Stark Shift Compensation

In addition to the Raman laser frequencies ω_1 and ω_2 in Eq. 2.2, it can be useful to add additional frequency content to the atom optics beams to cancel AC Stark shifts. Consider a single-frequency laser with intensity I_i and single-photon detuning $\Delta_{ij} = \omega_i - \omega_{je}$ relative to the $|j\rangle \rightarrow |e\rangle$ transition (with frequency ω_{je} , see Fig. 2.8).¹³ The AC Stark effect yields an energy shift to state $|j\rangle$ of [74]

$$\Delta E_{ij} = \frac{\hbar\Omega_i^2}{4\Delta_{ij}} = \frac{\hbar\Gamma}{4} \frac{(I_i/I_{\text{sat}})}{(2\Delta_{ij}/\Gamma)} \quad (\text{for } \Omega_i \ll |\Delta_{ij}|) \quad (2.6)$$

For red detuning, $\Delta_{ij} < 0$ and the state $|j\rangle$ is shifted down in energy ($\leftarrow \omega_{|j\rangle}^a$). For blue detuning, $\Delta_{ij} > 0$ and the state $|j\rangle$ is shifted up in energy ($\omega_{|j\rangle}^a \rightarrow$).

The single-photon detunings of ω_i from ω_{1e} and ω_{2e} are not equal in general ($\Delta_{i1} \neq \Delta_{i2}$), and so the Stark shifts of the two hyperfine ground states are also not equal (Eq. 2.6). If $\omega_{2e} < \omega_i < \omega_{1e}$, then the Stark shift pushes the atomic states away from each other

$$\leftarrow \omega_{|1\rangle}^a \quad \omega_{|2\rangle}^a \rightarrow \quad (2.7)$$

and the ground-state energy splitting $|\omega_{|1\rangle}^a - \omega_{|2\rangle}^a|$ is increased. If, however, $\omega_i < \omega_{2e}$ or $\omega_i > \omega_{1e}$, then the light shifts both atomic states in the same direction, but one

atoms prior to interferometry.

¹³In Eqs. 2.3, 2.4, and 2.6, I ignore the hyperfine splitting of the excited state F' manifold (as well as contributions from the recoil and Doppler shifts to the single-photon detuning Δ). This is an oversimplification, especially for AC Stark compensation, where Eq. 2.6 should actually be taken as a sum over all excited states $|e\rangle$.

state is affected more strongly than the other (because $|\Delta_{i1}| \neq |\Delta_{i2}|$)

$$\leftarrow \omega_{|1\rangle}^a \leftarrow \omega_{|2\rangle}^a \text{ or } \omega_{|1\rangle}^a \longrightarrow \omega_{|2\rangle}^a \rightarrow . \quad (2.8)$$

Thus, while both states are shifted in the same direction, their separation $|\omega_{|1\rangle}^a - \omega_{|2\rangle}^a|$ decreases. In either case, the Stark shift has changed the ground-state energy splitting $\omega_{|1\rangle}^a - \omega_{|2\rangle}^a$, which in turn contributes to a two-photon detuning from the Raman resonance (Eq. 2.2).

The combined Stark shift from both (possibly multiple-frequency) Raman lasers is nonzero in general, and so the lasers can become detuned from the two-photon resonance. This Stark detuning is intensity dependent, so the non-uniform laser beam profile yields a spatially-dependent Rabi frequency Ω_{eff} , which in turn yields poor pulse transfer and reduced interferometer contrast. There are several methods for compensating for the AC Stark shift:

1. *Multiple-Beam Intensity Balancing.* If one of the Raman beams shifts the atomic states towards each other while the other pushes them apart, then it is possible to compensate for their combined impact on the frequency difference $\omega_{|1\rangle}^a - \omega_{|2\rangle}^a$ by adjusting the relative intensities of the two beams. This works only if the ratio of the beam intensities $\frac{I_1(r,z)}{I_2(r,z)}$ is everywhere the same, which will not generally be true given diffraction and imperfect beam overlap.
2. *Single-Beam Relative Compensation.* By adding one or more spectator frequencies to a given beam, it is possible to compensate for its impact on the frequency difference $\omega_{|1\rangle}^a - \omega_{|2\rangle}^a$ by adjusting the relative strengths of the frequency components in the beam (as long as there is at least one frequency component that shifts the states towards each other and one that pushes them apart). This can be done independently for both beams. The relative Stark shift is then compensated regardless of the relative beam intensities, but the absolute energies of the atomic states are in general shifted by an intensity-dependent amount. This can yield a spatially-dependent interferometer phase (Eq. 1.7) if the intensity profile of the atom optics beams is different for the upper and lower interferometer arms.

3. *Single-Beam Absolute Compensation.* (Die beste aller möglichen Welten.) This scheme expands upon relative compensation by adding spectator frequency content such that all beams have at least three frequency components (ω_α , ω_β , ω_γ), with $\omega_\alpha < \omega_{2e} < \omega_\beta < \omega_{1e} < \omega_\gamma$. By adjusting the relative strengths of the frequency components, it is possible to completely cancel the Stark shift of both of the hyperfine ground states. There is then no intensity-dependent detuning or phase shift.

Atom Optics Lasers Implementation

This thesis encompasses two generations of atom optics lasers. The first was a tapered amplifier (TA) system with sufficient power for $2\hbar k$ interferometry (Chapters 3 and 4). The second is a high power laser system for LMT interferometry (Chapter 6). The increased power is also used for optical dipole lensing (Chapter 5).

For the first-generation system, the detuning was $\Delta \sim 1$ GHz, the single beam power was $P_0 \sim 200$ mW, the $1/e^2$ radial waist was $\omega_0 = 2$ cm, and AC Stark shifts were compensated with multiple-beam intensity balancing. Typical Rabi frequencies corresponded to $\delta t_\pi = 70$ μ s. Specifically, the laser light originated from the cooling master laser (M in Fig. 2.13), with the cooling fiber modulator off (ϕM_2), yielding light 1 GHz blue-detuned from the $|F = 2\rangle \rightarrow |F' = 3\rangle$ transition. For interferometry, the master laser was cavity-stabilized to a linewidth of < 1 kHz.¹⁴ This seed light was then split. One path was frequency shifted by an AOM to account for Doppler and recoil shifts, and the other was passed through a fiber EOM to generate a 6.8 GHz Raman sideband.¹⁵ These paths were then amplified by 1 W TAs, mode-cleaned with pinhole spatial filters, recombined with orthogonal polarizations, and transmitted to the primary beam path [Fig. 2.7(a)].¹⁶ The relative power of the two beams was adjusted to reduce residual AC Stark shifts to < 2 kHz.¹⁷

¹⁴The laser was locked to a cavity, and the cavity's length was stabilized to Rb saturation spectroscopy (Fig. 2.13).

¹⁵Specifically, AOM₂ and ϕM_5 , with AOM₁ off (Fig. 2.14).

¹⁶The 1 W TAs were TA₄ and TA₅ in Fig. 2.14. These TAs originally supplied both the lattice and the atom optics beams. See also [20].

¹⁷For multiple-beam compensation, we measure residual relative AC Stark shifts by halving the intensity of both beams and observing any shift in Raman resonance.

In the second generation, high-power laser system, the detuning can be $\Delta \sim 3$ GHz (or more), the total single beam power is $P_0 \sim 3$ W, the $1/e^2$ radial waist is $\omega_0 = 2$ cm, and AC Stark shifts can be compensated absolutely. Typical Rabi frequencies (for $\Delta \sim 3$ GHz) correspond to $\delta t_\pi = 15$ μ s. The second-generation laser system is summarized in Fig. 2.15. It is based on a 1560 nm RIO Orion laser with a free-running linewidth < 1 kHz, combined with 30 W fiber amplifiers and PPLN doubling crystals. Separate fiber modulators and AOMs on each path supply the frequency shifts needed for Raman interferometry and absolute AC Stark compensation.

For $\Delta \sim 3$ GHz, the carrier (unshifted, doubled RIO) is centered between ω_{2e} and ω_{1e} . One path is modulated at 6.8 GHz, and Raman transitions are driven by one of the resulting first order sidebands and the carrier on the other path. The depth of the 6.8 GHz modulation is adjusted to minimize single-beam relative AC Stark shifts.¹⁸ The other path (from which the carrier contributes to the Raman transition), is modulated at ~ 5 GHz. These modulation sidebands don't contribute to the Raman transition, but they do facilitate single-beam absolute AC Stark shift compensation on the second path.

Three feedback loops stabilize the Rabi frequency and AC Stark compensation of the high-power atom optics beams. The total optical power of each beam is monitored by a photodiode and adjusted by actuating the RF power to an AOM (Fig. 2.15). The frequency content of each beam is measured with a Fabry-Perot spectrum analyzer (with software fitting of the peak heights). The sideband-to-carrier ratio (modulation depth) is adjusted by actuating the microwave drive power to the fiber phase modulator. The Fabry-Perot trace also measures any asymmetry between the positive and negative first order sidebands. This asymmetry can arise from the limited doubling bandwidth of the PPLN crystal.¹⁹ We reduce the measured asymmetry by actuating the temperature of the PPLN crystal. Due to the measurement time of the Fabry-Perot and the response

¹⁸For single-beam compensation, we halve the power of each path individually. By adjusting the modulation depth to minimize the resulting shift in resonance, we achieve single-beam relative compensation. For the symmetric modulation scheme used, this roughly corresponds to single-beam absolute AC Stark compensation as well [29].

¹⁹The doubling bandwidth of 50 GHz [29] is not much larger than our typical modulation frequencies, which are $\gtrsim 5$ GHz. A weak etalon effect in the crystal could also yield a temperature-dependent frequency response.

time of the PPLN temperature, the feedback loops have step-response times exceeding the duration of a single experimental measurement (~ 30 s).²⁰ We therefore measure the power and spectrum at the end of one experimental trial, and adjust the actuator in preparation for the next. The feedback loops can then compensate for slow drifts in the system over the course of a sequence of trials.

2.2.4 Primary Telescope

Ideally, the Gaussian atom optics laser beams should be as large as possible. This increases the flatness of the intensity profile sampled by the finite-width atom cloud, which in turn improves Rabi frequency uniformity and reduces residual AC Stark shifts. Larger beams also have longer Rayleigh ranges. This reduces axial intensity variation and uncertainties arising from the Gouy phase with an unknown beam-waist location. In practice, the beam size is limited by the need for sufficient intensity with finite laser power. It is also limited by the clear aperture of the vacuum system ~ 10 cm.²¹ For an aperture of radius a , diffraction causes substantial intensity and phase variation for an input beam with $1/e^2$ radial waist $\omega_0 \gtrsim 2a/4.6$ (the 1% ripple criterion, see Fig. 2.9). We therefore typically operate at or below the 1% criterion.

Since the laser phase is directly imprinted on the atoms during an interferometric measurement, laser wavefront errors should be minimized. We therefore put both the retro mirror and the final lens of the primary telescope inside the vacuum system to avoid unnecessary vacuum viewports along the interferometer axis. Figure 2.10 shows the primary lens as it is mounted inside the upper ion pump. A 50 mm lens (located in the optics enclosure above the chamber, see Fig. 2.1) acts as the input to the Keplerian telescope. While this does not eliminate wavefront errors from the vacuum window altogether, the beam is smaller as it passes through the window. This approach also allows us to maintain a fully vertical telescope without any folding mirrors (which would have adverse impacts on wavefront and polarization, especially

²⁰The photodiode power-feedback loop is faster, but still difficult to actuate during the short optical pulses ($\delta t_\pi \sim 10 \mu\text{s}$), so we also apply power feedback only from one trial to the next.

²¹Currently, the limit is actually set by the 8.64 cm clear apertures of the in-vacuum optics (primary lens and retro mirror). Several 6" conflat flanges along the tube have bore diameters of 9.68 cm.

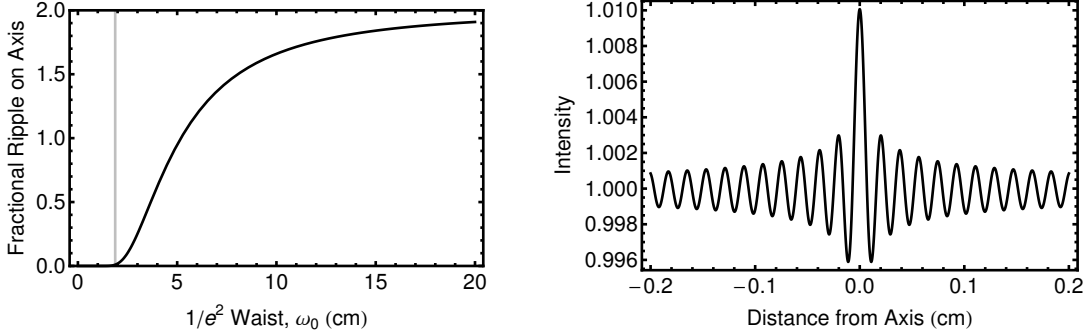


Figure 2.9: Intensity variation resulting from diffraction of a Gaussian beam from an aperture with radius $a = 4.32$ cm. Left: Fractional on-axis intensity ripple amplitude as one translates along the axis of the beam ($\sim 2 \exp[-(a/\omega_0)^2]$). The vertical gray line indicates the 1% ripple criterion ($\omega_0 = 1.9$ cm), above which the ripple increases dramatically. Right: Paraxial radial intensity profile 10 m from the aperture at the 1% ripple criterion.

for the circularly polarized beam). In the future, the chamber could be extended vertically and an in-vacuum pinhole spatial filter could be placed at the focus of the primary telescope, scrubbing all wavefront errors prior to the final lens.

Spherical aberration in the primary lens can also cause wavefront errors. A simple spherical lens is preferred from the perspective of surface quality (better polishing methods as compared to an asphere; fewer surfaces and better vacuum compatibility as compared to a compound achromatic lens). However, a spherical lens has 4th order phase variations that increase for smaller F/#, favoring a longer-focal-length primary lens. We chose a CVI PLCX-101.6-360.6-UV lens (plano-convex, 86.4 mm clear aperture, 786 mm back focal length at 780 nm). In the future, this lens could be replaced with an optic of improved quality.

2.2.5 Rotation Compensation System

The retro mirror is the most important optical element in the system. Like the primary telescope lens, it must be large enough to minimize aperture effects with large optical beams. Unlike the primary telescope, only one beam in the Raman pair is reflected by

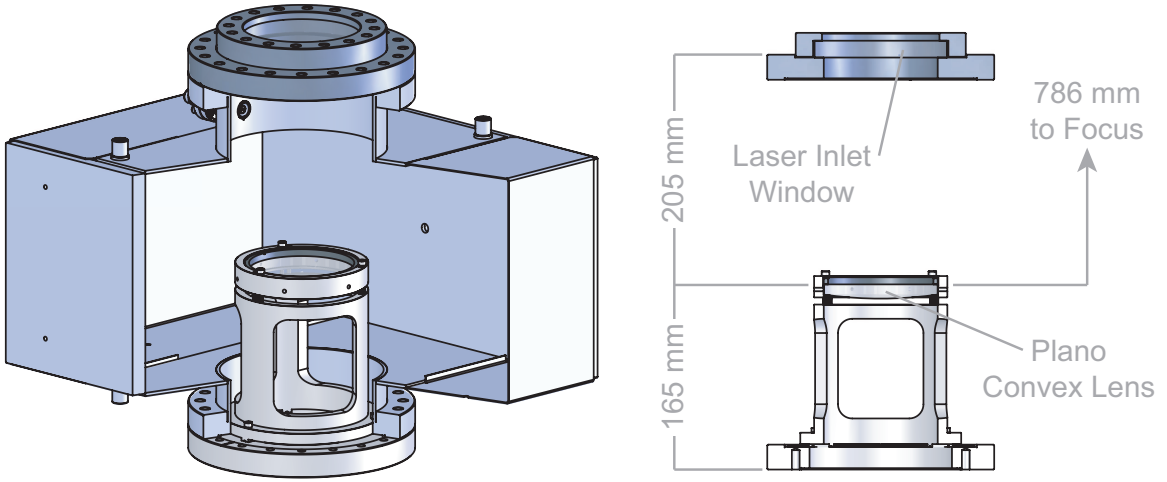


Figure 2.10: Collimating lens of the primary telescope (see also Fig. 2.7). The lens is installed inside a 300 L/s ion pump at the top of the vacuum chamber (see Fig. 2.1). A tophat/tripod structure supports the lens in a tip-tilt mount (aligned prior to installation of the ion pump).

the mirror before interacting with the atoms, so there is no common mode cancellation of the wavefront errors it introduces.²²

The retro mirror also sets the direction of \mathbf{k}_{eff} (Eq. 1.1) for the two-photon Raman transitions, which in turn sets the direction of the momentum splitting and the axis of the interferometer. To be concrete, let two co-propagating, overlapping laser beams be incident from above at an angle θ with respect to the normal vector $\hat{\mathbf{n}}$ of the retro mirror. The laser with wavevector \mathbf{k}_2 interacts with the atoms on the way down, and the laser with wavevector \mathbf{k}_1 interacts with the atoms after reflection. Then

$$\mathbf{k}_{\text{eff}} = \mathbf{k}_1 - \mathbf{k}_2 \approx 2k_1 \cos(\theta)\hat{\mathbf{n}} \quad (2.9)$$

As the Earth rotates while the atoms are in free fall for ~ 3 s, $\hat{\mathbf{n}}$ rotates as well if the retro mirror is held fixed in the lab frame. This leads to Coriolis phase shifts across the atom cloud (see Chapters 3 and 4).

²²Given diffraction and imperfect alignment (especially as the mirror is rotated), wavefront errors from the lens will not be canceled at all length scales, so the demands on its optical quality are not that much less stringent in practice.

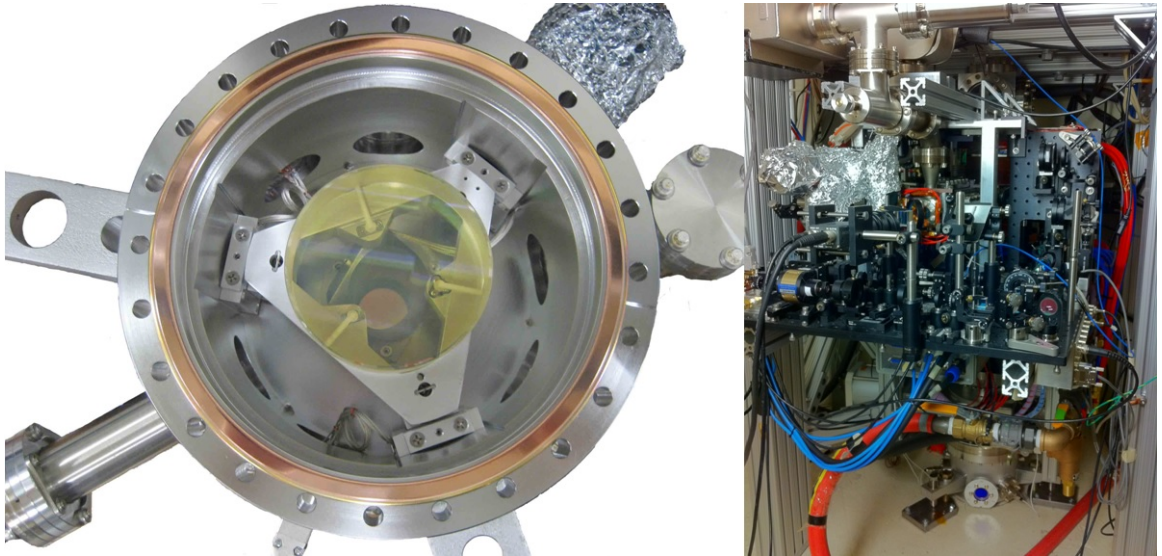


Figure 2.11: Retroreflection mirror and rotation compensation system (RCS). Left: the mirror mounted on a piezo-actuated tripod, inside its vacuum can. Two of three coarse-positioning arms are partly visible. Right: the RCS bolted to the pit floor and connected to the bottom of the vacuum chamber with bellows. The back of the 2D MOT (with associated optics) is also visible (see Fig. 2.12).

To control and mitigate these phase shifts, it is essential to be able to rotate the retro mirror about an arbitrary axis in the horizontal plane. We therefore mount the retro mirror on a custom in-vacuum piezo-actuated tip-tilt stage (Fig. 2.11). This system has a precision of ~ 1 nrad and a range of $\sim 400 \mu\text{rad}$ [29].²³ The mirror itself is made of ultra-low thermal expansion (ULE) glass, and is 5 cm thick to reduce distortions during rotation.²⁴ With this system, it is possible to “turn off” the rotation of the Earth during each measurement by rotating $\hat{\mathbf{n}}$ in the opposite direction. This keeps the interferometer axis fixed inertially.

²³At the location of our lab in Stanford, CA, the rotation rate is $\Omega_E = 57.9 \mu\text{rad/s}$, so this allows us to establish an inertial frame for up to 7 s, assuming the appropriate initial alignment. Conversely, since the atoms are only in free fall for 3 s, there is overhead in the event of the failure of one of the three piezo stages.

²⁴A small fraction of the light incident on the retroreflection mirror is transmitted through the anti-reflection coating and 5 cm thick ULE glass and can be viewed through a vacuum window. We use this transmitted light to characterize and align the MOT, lattice, and atom optics beams. It is also possible to monitor the orientation of the retroreflection mirror with a laser angle sensor [61].

2.3 Atom Source (Cooling)

Several stages of cooling are required prior to launch to keep the atoms well localized during free fall. Even with common sub-Doppler laser cooling techniques, the photon recoil limit for laser-cooled ^{87}Rb atoms is 360 nK (5.9 mm/s) [71]. At this temperature, an atomic point source expands to 15 mm after 2.5 s of free evolution. This is comparable to the size of atom-optics beams, so the atoms would explore a non-uniform intensity. Therefore, after a magneto-optic trap (MOT) stage (Section 2.3.1), we pursue sub-recoil ultra-cold temperatures with evaporative cooling techniques (Sections 2.3.2 to 2.3.4). Evaporative cooling yields an atom ensemble of much higher phase space density (typically we evaporate to Bose-Einstein condensation (BEC) [68, 69]). However, the high spatial density and repulsive interactions of the Rb atoms generate a large chemical potential that yields substantial kinetic energy on trap release.²⁵ We therefore use a magnetic lensing stage to reduce the spatial density and velocity distribution of the ensemble (Section 5.2). All of the cooling and trapping stages (MOT, evaporation, and magnetic lensing) occur in a vacuum chamber at the bottom of the interferometer region (Fig. 2.12). Images of the atom distribution in the atom source chamber are made with absorption imaging [29].

2.3.1 Magneto-Optical Trap

The first stage of cooling is a magneto-optical trap (MOT). The MOT has become the workhorse of cold-atom physics, and useful references are [74, 75]. Fundamentally, an electromagnetic environment is established such that when an atom moves away from the center of the MOT, it preferentially scatters light from a laser beam pointed in a direction opposite to the atom's velocity. This reduces the atoms' thermal velocity distribution and confines them to the center of the trap. Our MOT typically loads 4×10^9 ^{87}Rb atoms in 3 s. Three major components are needed for a MOT: (1) a *vacuum chamber*, (2) *magnetic field control*, and (3) *cooling lasers*.

²⁵This kinetic energy can even exceed the recoil temperature. Nevertheless, the phase space density at the end of evaporation is much higher than in the MOT, so the temperature can be improved by reducing the spatial density in a phase-space-conserving process (adiabatic relaxation or lensing).

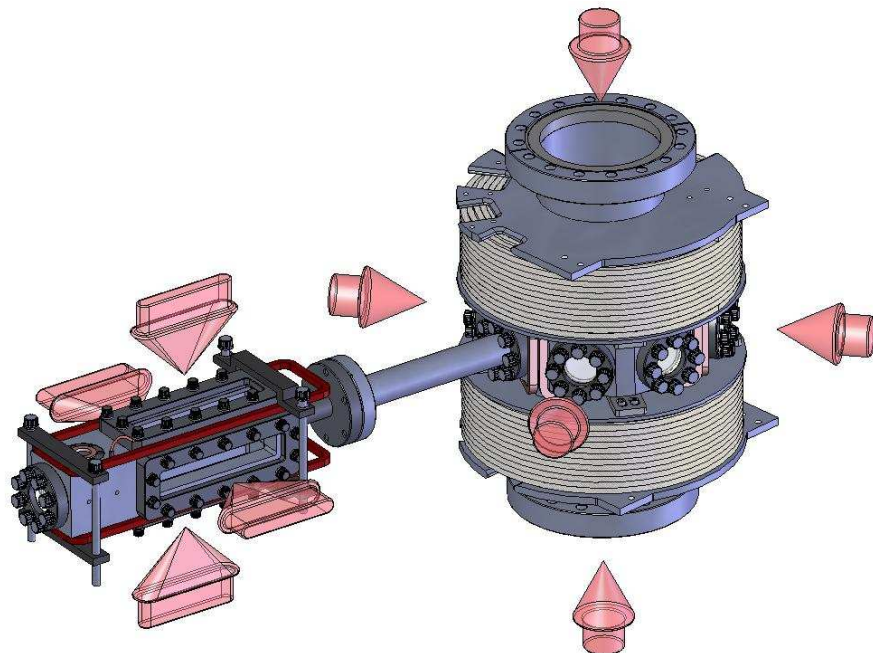


Figure 2.12: The atom source. The 2D MOT (left) is connected to the 3D MOT with a differential pump. The vertical quadrupole coils (light-beige) are wound directly on the chamber, above and below the 3D MOT windows. Some of the TOP coils are partially visible (light-red, each of the four coils encircles two ports on the octagonal chamber). From [20].

MOT Vacuum Chamber

Background gas collisions remove atoms from the trap. A UHV chamber is therefore needed. However, some background pressure of Rb atoms is necessary to load the trap. The interplay between the collision-loss and loading rates motivates splitting the trap, with the primary 3D MOT fed by an atomic beam from a preliminary 2D MOT.²⁶ The chambers are connected with a differential pump (a 3 mm diameter, 5 cm long graphite constriction), allowing Rb partial pressures in the 2D MOT to rise to $\sim 10^{-7}$ Torr while maintaining UHV in the 3D chamber (and interferometer region). The 2D MOT mimics the 3D MOT, but with elongated beams for increased trapping volume. Along the 2D MOT axis, a pair of weak, unbalanced laser beams (the pusher and retarder) slightly cool the atoms axially while pushing them toward the 3D, increasing its effective loading rate. Hereafter, I focus on the 3D MOT, or simply “the” MOT.

Magnetic Field Control

Magnetic fields are controlled with several Helmholtz (or anti-Helmholtz) coil pairs. The primary trapping field is a vertical quadrupole field established by anti-Helmholtz coils wound directly on the vacuum chamber (Fig. 2.12). During MOT loading, the radial field gradient is 5.6 G/cm. Three additional pairs of Helmholtz coils apply bias fields to cancel Earth’s field at the center of the trap (not shown in Fig. 2.12).

Cooling Lasers

Two optical frequencies are required for the MOT (see Fig. 2.8).²⁷ Cooling occurs on the $|F = 2\rangle$ to $|F' = 3\rangle$ cycling transition of the ^{87}Rb D₂ line at 780 nm.²⁸ A

²⁶Five grams of natural-abundance Rb (72% ^{85}Rb , 28% ^{87}Rb) was initially transferred into the 2D MOT vapor cell. Since Rb has a low melting point (39 °C), its vapor pressure in the cell can be adjusted by heating it slightly.

²⁷I focus on ^{87}Rb , though the system is capable of simultaneously cooling ^{87}Rb and ^{85}Rb [20, 29].

²⁸For the 3D MOT, the cooling laser is $\delta_c/(2\pi) = 10$ MHz red-detuned (the linewidth of the transition is $\Gamma/(2\pi) = 6.1$ MHz [71]). The 2D MOT cooling light is 4 MHz closer to resonance. This increases the damping rate in the 2D MOT (at the cost of a reduced capture velocity and an increased ultimate temperature), which increases the effective loading rate of the 3D MOT. The 4 MHz shift is implemented with a push-pull AOM pair on the 2D cooling beamline (center of Fig. 2.13).

small fraction of the atoms will decay to the $|F = 1\rangle$ state, where they are no longer affected by the cooling light. We therefore add a small amount of repump power on the $|F = 1\rangle$ to $|F' = 2\rangle$ transition to clear atoms from $|F = 1\rangle$.

All of the cooling and trapping light originates from a single master laser on a remote optical table (Fig. 2.13). The master laser is a Newport Vortex external cavity diode laser (ECDL) with a linewidth of $\lesssim 1$ MHz. It is locked to Rb via saturated absorption spectroscopy in a vapor cell [76], and acousto-optic modulators (AOMs) [77] and fiber electro-optic phase modulators apply the \sim GHz frequency shifts needed to address particular hyperfine lines (for cooling and repump; for details on the modulation scheme, see [20, 78]). Optical tapered amplifiers (TAs [79]) and booster optical amplifiers (BOAs) boost the power of the light, which is sent to the atom source in the pit in 40 m optical fibers. (The vertical z -axis MOT light goes to the top of the pit, and joins the atom-optics beam path, see Fig. 2.14.) In the pit, the light is split for all of the counterpropagating beam pairs of the 2D and 3D MOTs, enlarged with telescopes, and circularly polarized before being directed into the vacuum chamber.

2.3.2 Magnetic Trap Evaporation

We cool the atoms further by forced evaporation in a quadrupole magnetic trap (with the same anti-Helmholtz coils used for the MOT). The field in the quadrupole trap is

$$\mathbf{B} = -(\nabla B)x\hat{\mathbf{x}} - (\nabla B)y\hat{\mathbf{y}} + 2(\nabla B)z\hat{\mathbf{z}}, \quad (2.10)$$

where ∇B is the radial gradient.²⁹ This yields a potential $U = \mu|B|$, where $\mu = \mu_B g_F m_F$ is the product of the Bohr magneton and the Landé g-factor. In state $|F = 1\rangle$, ⁸⁷Rb atoms have $g_F = -\frac{1}{2}$, so $|F = 1, m_F = -1\rangle$ atoms can be trapped by this potential.

We transfer the atoms from the MOT into the pure magnetic trap by turning off

²⁹ ∇B is set by the current I and geometry of the Helmholtz coils. We find that a current of $I = 17.5$ A is necessary to support the atoms against gravity ($\mu 2\nabla B = mg$), which implies that $\nabla B/I = 0.87$ G/cm/A.

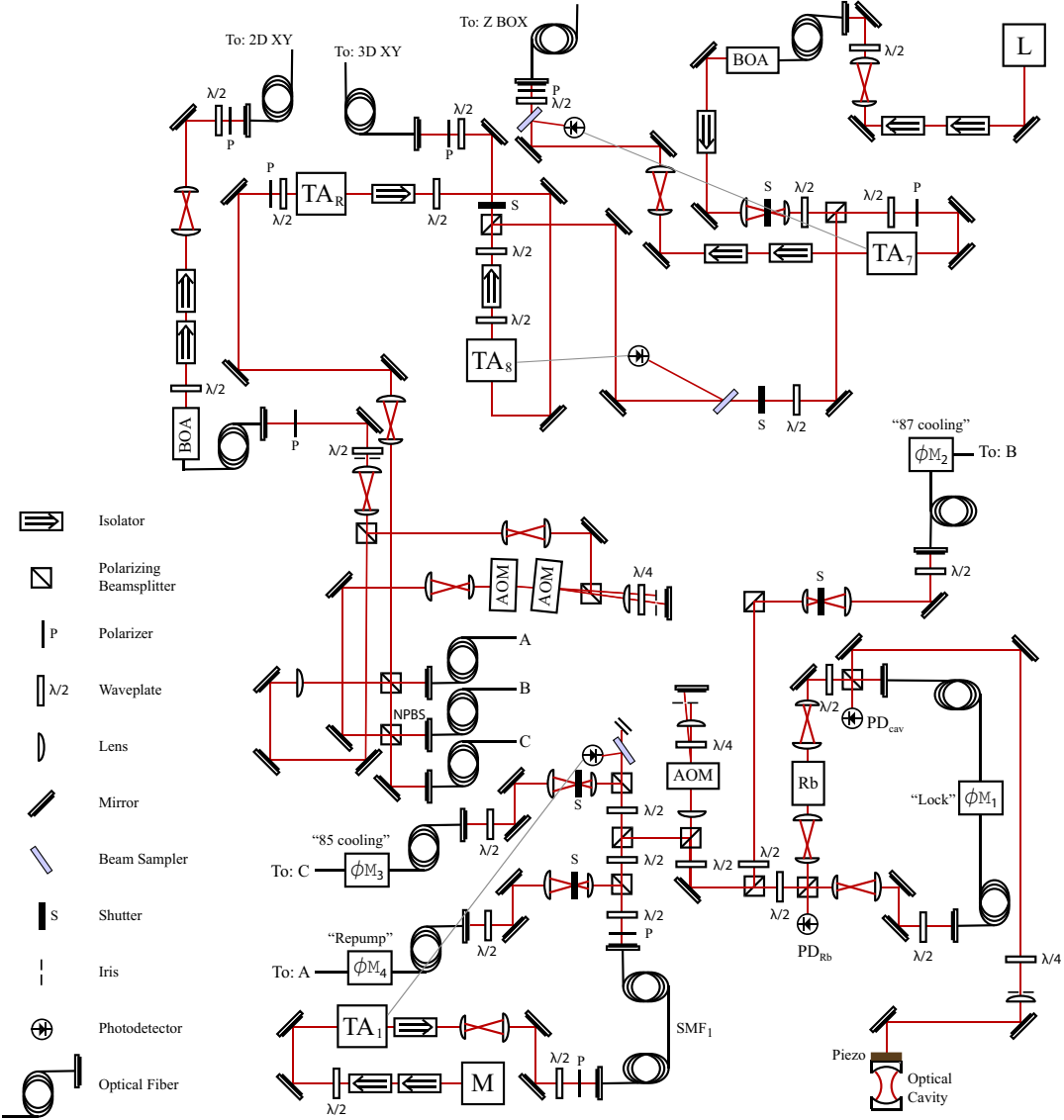


Figure 2.13: Cooling and trapping lasers. A master laser (M, lower left) is locked to Rb (lower right, the laser linewidth can also be narrowed with a cavity lock [80]). Fiber phase modulators ($\phi M_{2,3,4}$) generate sidebands at the repump and cooling frequencies for ^{87}Rb and ^{85}Rb . Tapered amplifiers (TAs) and booster optical amplifiers (BOAs) amplify the optical power before it is sent to the 2D and 3D MOTs over optical fibers (upper left). Photodetectors enable intensity feedback. A second seed laser (L, upper right) generates light ~ 90 GHz blue-detuned from the cooling transition. Thus, the input to the “Z Box” (Fig. 2.14) can be switched from cooling light to lattice light. Updated from [20].

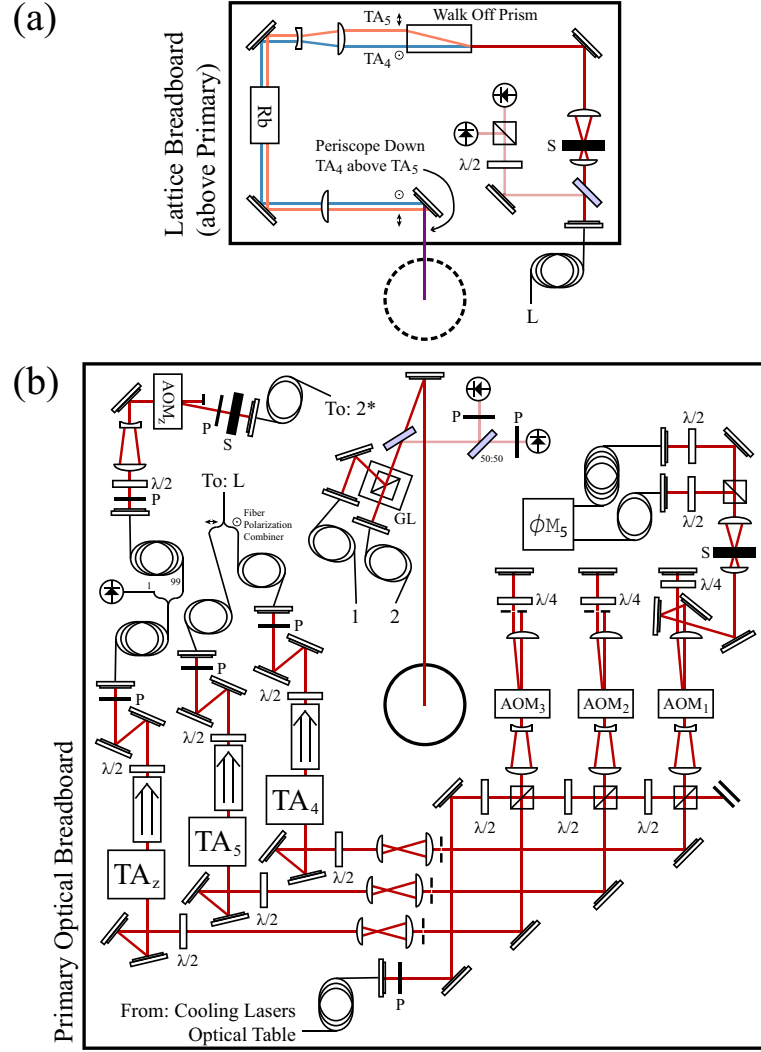


Figure 2.14: Vertical axis beam delivery (“Z Box,” see Fig. 2.1). (b) Lower, primary level; (a) secondary lattice breadboard mounted above the primary level. A central hole in the primary breadboard allows for light to be sent down towards the interferometer region. *Atom optics* light is delivered via optical fibers (1 and 2, Fig. 2.15), combined on a Glan-laser (GL) prism, and then sent through the primary telescope [Fig. 2.7(a)]. *MOT* light is delivered via optical fiber (Fig. 2.13), amplified by TA_z , and coupled into the primary beam axis (2^* , Fig. 2.15). The *lattice* light is split, frequency shifted by $AOM_{1,2}$, amplified by $TA_{4,5}$, and brought up to the lattice breadboard (a) in fiber. The beams are then displaced, cleaned with a hot Rb-cell frequency notch filter, and delivered to the atoms [Fig. 2.7(b)]. Updated from [20]; for optical component key see Fig. 2.13.

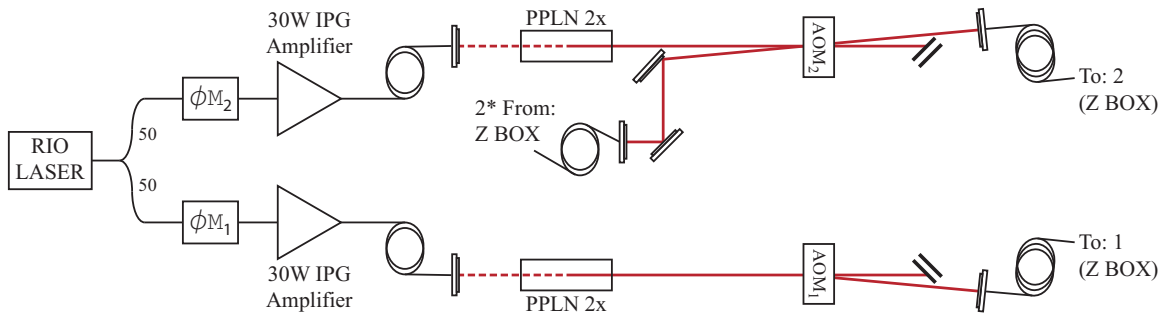


Figure 2.15: High power laser system used to generate ~ 3 W per beam for lensing and LMT interferometry (Chapters 5 and 6; shown here in the LMT configuration). Light from a 1560 nm RIO Orion laser (linewidth < 1 kHz) is split and sent through two fiber phase modulators. These phase modulators are driven to yield the necessary sidebands for Raman interferometry and AC Stark shift compensation. Each path then passes through a 30 W fiber laser amplifier (IPG Photonics EAR-30K-C-LP-SF) and a PPLN frequency doubling crystal (Coveshion MSHG1550-1.0-40). A pair of AOMs provides amplitude control of each beam. (The AOMs also break degeneracies such that only one pair of frequencies from the fiber phase modulators can drive Raman transitions, thus preventing undesirable spatial modulation of the Rabi frequency.) MOT light from the “Z Box” optics enclosure (Fig. 2.14) is introduced along an undiffracted path through AOM₂, so that the primary beamline can be switched rapidly between MOT and atom optics light. The outputs of the AOMs are delivered to the “Z Box” in short 2 m optical fibers (to avoid stimulated Brillouin scattering). See also [81].

the cooling lasers and quickly increasing ∇B .³⁰ In the ~ 30 ms prior to the sudden increase of ∇B , we increase the detuning of the cooling laser and reduce the cooling power, repump power, and quadrupole gradient. This procedure is empirically found to improve the initial phase space density in our magnetic trap.

Over the following 15-20 s, a microwave knife progressively removes the hottest atoms from the trap by driving them from $|F = 1, m_F = -1\rangle$ to $|F = 2, m_F = -2\rangle$ (which is not trapped by the magnetic potential) [63].³¹ This microwave field is supplied by two counterpropagating microwave horns, phase tuned for maximum standing-wave amplitude at the center of the trap. Further details on the evaporation procedure can be found in [29].

After ~ 10 s of evaporation, the atoms are cold and localized enough to spend a substantial amount of time near the field zero of the quadrupole trap. This would lead to a large loss rate via non-adiabatic Majorana spin flips. We therefore prevent the atoms from reaching the field zero with one of two common methods: an optically plugged trap (OPT; Section 2.3.3) or a time orbiting potential (TOP) trap (Section 2.3.4).

2.3.3 Optically Plugged Quadrupole Trap

An optically plugged trap uses a focused blue-detuned laser to repel atoms from the region of field zero (Fig. 2.16) [82]. The combined plugged-quadrupole potential has two new local minima at non-zero magnetic field [63]. The trap shape is asymmetric, but the plug can effectively block Majorana loss even for large quadrupole gradients, allowing for tight traps and fast evaporation. We use a 6 W, 532 nm laser (Lighthouse Photonics Sprout), focused to $20\ \mu\text{m}$. With this OPT we can make BECs with 4×10^6 atoms and time-of-flight temperatures of $1.4\ \mu\text{K}$, dominated by chemical

³⁰This is facilitated by an LC resonator circuit [29]. A short depump pulse on the $|F = 2\rangle \rightarrow |F' = 1\rangle$ transition is used to transfer residual $|F = 2\rangle$ atoms to $|F = 1\rangle$. Only $\sim 1/3$ of the atoms are then in the trapped $|F = 1, m_F = -1\rangle$ state, though this can be improved somewhat with random tweaks [75].

³¹In the middle of the microwave ramp, ∇B is reduced to prevent excessive three-body losses in the denser cloud. At the end of evaporation (and for the magnetic lens) the power supply driving the quadrupole coils is switched to constant current mode for better magnetic field stability.

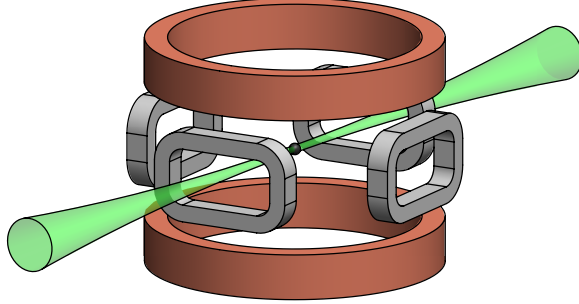


Figure 2.16: Simplified schematic of the atom source, including the quadrupole coils, TOP coils, and optical plug. Note that the optical plug and TOP coils are not generally used simultaneously. From [29].

potential in the tight trap.³² However, the OPT trap geometry varies with the plug laser alignment, and the velocity of atoms released from the trap depends strongly on the relative dynamics of the plug and magnetic field turn-off. Further, a harmonic trap is desirable for magnetic lensing. The TOP trap is therefore preferred for several of the experiments that follow.

2.3.4 TOP Trap

The TOP trap facilitates both evaporation without Majorana loss and magnetic lensing in a harmonic potential (see Section 5.2) [83]. It is created by adding a spinning horizontal bias field

$$\mathbf{B}_{\text{bias}} = B_0 \cos(2\pi\nu t) \hat{\mathbf{x}} + B_0 \sin(2\pi\nu t) \hat{\mathbf{y}} \quad (2.11)$$

to the quadrupole trap (Eq. 2.10). The spinning frequency $\nu = 2.6$ kHz is chosen to be much greater than the atoms' oscillation frequency in the trap. As a result, we can consider a time-averaged effective potential where the atoms never reach the spinning field zero (the circle of death), though micro-motion still occurs at the spinning frequency.

³²This is the evaporative source used for instance for Fig. 3.3(b) and as the input in Fig. 5.5.

Combining the quadrupole and TOP fields (Eqs. 2.11 and 2.10), yields a potential

$$U = \mu \sqrt{(B_0 \cos(2\pi\nu t) - (\nabla B)x)^2 + (B_0 \sin(2\pi\nu t) - (\nabla B)y)^2 + (2(\nabla B)z)^2} \quad (2.12)$$

Taking the time average³³ and expanding to second order about the trap minimum yields the radial and vertical trap frequencies:

$$m\omega_\rho^2 = \frac{\mu(\nabla B)^2}{2B_0} \quad (2.13)$$

$$m\omega_z^2 = \frac{4\mu(\nabla B)^2}{B_0}. \quad (2.14)$$

In the absence of gravity, the ratio between the trap frequencies is irrational $\omega_z/\omega_\rho = 2\sqrt{2}$ (Eqs. 2.13 and 2.14). This is undesirable for three-dimensional magnetic lensing because it makes perfect synchronization of the vertical and radial oscillations impossible. Earth's gravitational field, however, modifies the potential [84], pulling the atoms below the location of zero quadrupole field, yielding [29]

$$\frac{\omega_z}{\omega_\rho} = 2\sqrt{2} \sqrt{\frac{1-\chi^2}{1+\chi^2}} \quad \chi \equiv \frac{mg}{2\mu\nabla B}. \quad (2.15)$$

Thus it is possible to synchronize the oscillations with an appropriate choice of ∇B (see Section 5.2).

To evaporate in the TOP trap, we turn on a spinning field of $B_0 = 4.2$ G after ~ 6 s of evaporation, with $\nabla B = 110$ G/cm. Over the next ~ 8 s, a microwave knife is still applied, but we also reduce the spinning field gradually to $B_0 = 0.30$ G. Hotter atoms at the periphery of the trap are then removed by the circle of death (as well as by the microwave knife). At the end of evaporation in the TOP trap, we typically obtain a ~ 15 μ m, 30 nK BEC with 2×10^5 atoms.³⁴

³³The deepest trap (highest oscillation frequency) used has $\nabla B = 110$ G/cm and $B_0 = 0.30$ G, so $\frac{(\omega_\rho)_{\text{max}}}{2\pi} \approx 128$ Hz $\ll \nu = 2.6$ kHz, justifying the time averaging.

³⁴This is the evaporative source used for instance for Fig. 3.3(a) and (after magnetic lensing), as the 1.6 nK source to input to the optical dipole lens (Section 5.1).

TOP Coil Drive Circuit

The spinning bias field is created by two orthogonal pairs of Helmholtz coils (see Fig. 2.12). The coils are driven by a high-power stereo audio amplifier at 2.6 kHz, with the pairs out of phase by 90° [Fig. 2.17(b)]. A microwave circuit generates the balanced, amplitude-controlled quadrature audio signals [Fig. 2.17(a)]. An external trigger resets the absolute phase at the beginning of each experimental cycle. This makes micro-motion in the time-varying TOP trap (as the atoms follow the field zero) consistent from shot to shot.

To maximize power transmission to the Helmholtz coils, we add $C = 4.4 \mu\text{F}$ of capacitance to make an RLC resonator. Figure 2.17(c) shows the amplitude of the signal transmitted to a coil pair as a function of frequency. The theoretical fits correspond to a simple RLC model for the voltage across the Helmholtz coils (with inductance L and series resistance R for the pair):

$$V_{\text{coils}} = \sqrt{\frac{C^2\omega^2(R^2 + L^2\omega^2)}{1 - 2CL\omega^2 + C^2\omega^2(R^2 + L^2\omega^2)}} V_{\text{in}} \quad (2.16)$$

where $\omega = 2\pi f$ is the driving frequency. In free space, the resonance is at 1.9 kHz. Constraining $C = 4.4 \mu\text{F}$, we find that for a coil pair, $L = 1.6 \text{ mH}$ and $R = 2.2 \Omega$ (consistent with the value of R measured at DC). With the coils mounted on the steel vacuum chamber, eddy currents cause substantial losses at audio frequencies. This shifts the resonance to 2.6 kHz with reduced amplitude. With the chamber, the fit yields $L_{\text{eff}} = 0.9 \text{ mH}$ and $R_{\text{eff}} = 7.4 \Omega$. A similar shift is apparent in the phase of the transmitted signal [Fig. 2.17(d)].

As the coils and chamber heat up over the course of several repeated trials, R_{eff} increases, changing the current driven through the coils. This changes B_0 , and in turn affects the trap geometry, in particular affecting the lensing stage and the momentum imparted during trap turnoff. We observe steady-state thermalization after ~ 7 experimental trials at our current 30 s cycle time. This can be mitigated somewhat by measuring the voltage across the $4.4 \mu\text{F}$ capacitor and actuating the voltage controlled attenuator with a PID servo with a fast direct path (not shown in Fig. 2.17), but

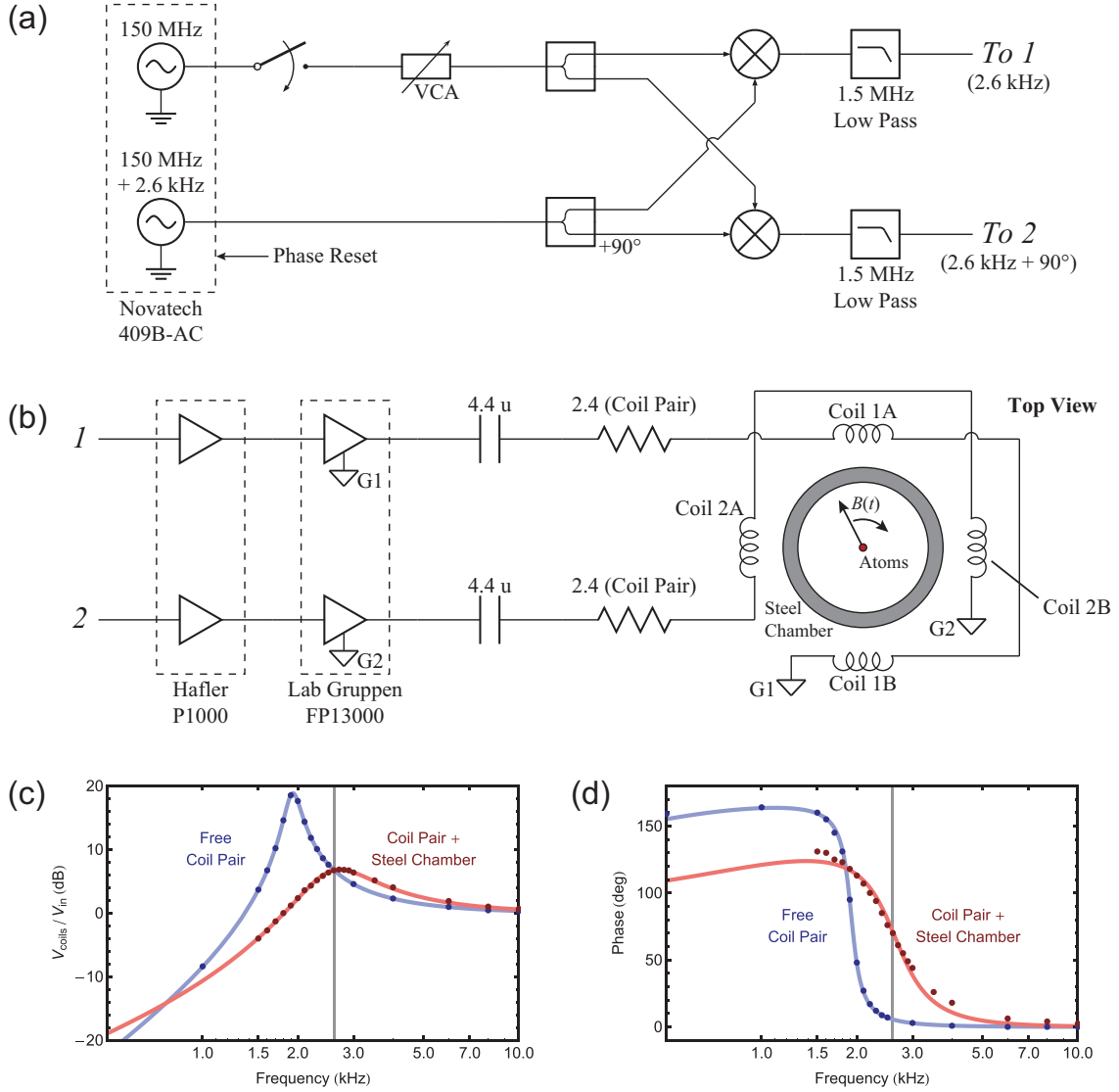


Figure 2.17: Circuit for driving the TOP coils at 2.6 kHz. (a) Generation of 2.6 kHz sine waves, offset by 90°, by mixing high-frequency inputs. The absolute phase and amplitude are controlled remotely with a phase reset trigger, a switch, and a voltage controlled attenuator (VCA). (b) The quadrature signals from (a) are amplified with audio amps and applied to Helmholtz coils, yielding a spinning magnetic field $\mathbf{B}(t)$ in the chamber. A $4.4 \mu\text{F}$ capacitor combines with the resistance and inductance of each coil pair to yield a free-space RLC resonance at 1.9 kHz. Eddy currents in the steel vacuum chamber shift the resonance frequency to 2.6 kHz, as seen in the amplitude (c) and phase (d) of the signal transmitted to the coils.

it has proven more effective to heat the coils to their steady-state value before an experimental run.

2.3.5 Magnetic Lens

This stage cools the atoms further prior to launch. It is a variant on delta-kick cooling [85–92]. The basic approach is to release a compact source of atoms into a shallow harmonic trap. Since oscillation frequency is independent of amplitude in a harmonic potential, all of the atoms will reach their turning points simultaneously after one quarter period. They have thus lost all of their kinetic energy in climbing the potential. By turning the trap off suddenly, we can release the atoms with a reduced temperature (at the cost of an increased size). In practice, the temperature is limited by the finite initial extent of the atom distribution (how perfect of a point source it is) and by anharmonicities of the potential (aberrations). For the magnetic lens, we use a weak TOP trap for the harmonic potential. Lensing is a faster alternative to adiabatic relaxation [93], with many benefits. For the evaporated sources discussed in Sections 2.3.3 and 2.3.4 it yields launched clouds at temperatures ranging from 1 to 50 nK. For details on the magnetic lens, see Section 5.2.

2.3.6 State Preparation

After evaporation and the magnetic lens, we transfer the atoms into a magnetically insensitive state to minimize the impact of Zeeman phase shifts (Section 2.2.2). We use a microwave pulse to transfer the atoms from the trapped state $|F = 1, m_F = -1\rangle$ to $|F = 2, m_F = 0\rangle$. Due to the large size of the steel atom source vacuum chamber, substantial currents are needed for the quadrupole trap and large time-varying eddy currents persist after trap release. We therefore wait 60 ms for the eddy currents to decrease before applying the microwaves. We also chirp the microwaves over a range of ~ 10 kHz to accommodate magnetic field inhomogeneities. Despite the eddy currents and magnetic field inhomogeneities, the transfer efficiency into $|F = 2, m_F = 0\rangle$ is typically $\sim 75\%$. We use a short blow-away pulse on the $|F = 1\rangle \rightarrow |F' = 0\rangle$ transition to remove the untransferred $|F = 1\rangle$ atoms.

2.4 Launch

We collect and cool atoms at the bottom of the tower and then launch them upwards with an optical lattice. This introduces some complexity to the system (compared with dropping the atoms from the top of the tower), but it affords several benefits. Compared with dropping, launching yields twice the maximum free-fall time, which in turn quadruples the interferometer phase shift ($k_{\text{eff}}gT^2$) and sensitivity (Section 1.2). Perhaps more important, the launch parameters can be adjusted. For instance, it is possible to run interferometers with different initial velocities.³⁵ This facilitates exploration of velocity-dependent phase shifts, including that resulting from the gravitation of the atoms' kinetic energy (Section 1.2.2). Many systematic errors can also be understood through the velocity dependence of their phase shifts [14].

Launching the atoms with different velocities also allows us to vary the free-fall time and peak height of the atoms' trajectory. Adjusting the free-fall time, and in turn the time-of-flight (TOF) to imaging, facilitates measurements of the TOF temperature, imaging system aberrations, and other diagnostics. There are similar benefits to being able to image the atoms as they travel upwards or downwards past a given camera. Launching the atoms to different heights changes the amount of time that they spend in different regions in the vacuum tower. This facilitates improved spatial resolution for *in situ* atom interferometric measurements of magnetic fields and gravity gradients. It also allows for measurements of the spatially varying vacuum lifetime (Fig. 2.5).

2.4.1 Coherent Optical Lattice Launch

We use a chirped optical lattice to launch the atoms. Conventional atomic fountains typically launch with moving optical molasses [19, 94]. However, this would reheat the ultracold atoms. An optical lattice launch is an alternative, coherent process [95].³⁶ The lattice acceleration results from repeated adiabatic rapid passage from $|p + 2n\hbar k\rangle$

³⁵An even greater range of velocities is made possible by imaging at the top of the interferometer (allowing $v_L > 14$ m/s).

³⁶Heating can still occur in a lattice [96, 97], but at a substantially lower level than in a moving molasses.

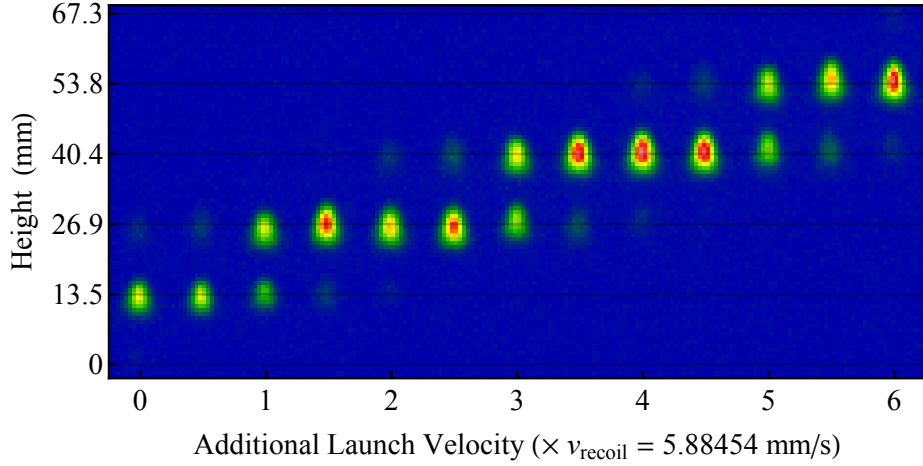


Figure 2.18: Sequence of images demonstrating the velocity quantization of the lattice launch. For the leftmost image, 1142 photon recoil momenta are imparted to the atoms, launching them to a height of 1.25 m. In all cases, imaging occurs 1.14 s after launch.

to $|p + 2(n + 1)\hbar k\rangle$ (similar to a multi-photon Bragg transition).³⁷ As a result, the launch velocity is quantized in increments of $2\hbar k/m$, as can be seen in Fig. 2.18. An attempt to launch by imparting anything but an even-integer multiple of photon recoils yields the desired mean velocity, but has the additional effect of a $2\hbar k$ beamsplitter. For instance, a $(2n + 1)\hbar k$ launch yields equal splitting into two clouds with momenta $(2n)\hbar k$ and $(2n + 2)\hbar k$.

We therefore restrict the launch velocity to an even-integer multiple of the recoil velocity $v_L = 2n\hbar k/m$. Nevertheless, imperfections in the lattice launch (incomplete adiabaticity, Landau-Zener tunneling, etc.) cause a small fraction of the atoms to be launched into the $\pm 2\hbar k$ momentum states (Fig. 2.18).³⁸ We can remove these side peaks with a Raman π -pulse with a velocity acceptance $\lesssim 2\hbar k/m$. For atoms prepared

³⁷There is also a satisfying classical picture. Consider a blue-detuned lattice with $\omega_1(t)$ the upward beam frequency and $\omega_2(t)$ the downward beam frequency. The atoms are trapped at the minima of the lattice intensity, which move in the lab frame at a velocity $v_{\text{lat}} = \frac{\omega_1 - \omega_2}{2k}$. (In a frame moving at velocity v_{lat} , the Doppler-shifted frequencies are equal, with $\omega_1 - kv_{\text{lat}} = \omega_2 + kv_{\text{lat}}$, and the lattice is at rest.) By chirping the frequency difference such that $\omega_1(t) - \omega_2(t) = 2kat$, the atoms can be accelerated with acceleration a . However, this picture doesn't explain the quantized launch velocities.

³⁸We refer to the side peaks as “friends” along for the ride. Or occasionally as “hoodlums out for a ride” in the event of recent exposure to German graduate students.

in state $|F = 2, m = 0\rangle$ prior to launch, this transfers only atoms in the central peak to $|F = 1, m = 0\rangle$, and the atoms in the side peaks can be removed with a subsequent blow-away pulse resonant with $|F = 2\rangle \rightarrow |F' = 3\rangle$.

The launch requires a deep lattice to reduce Landau-Zener tunneling while the atoms are accelerated. However, spontaneous emission losses also increase with the lattice depth. Appropriate intensities and detunings are therefore necessary to balance these effects (Section 2.4.3). Typical operating parameters for a full-tower launch are powers of $P_0 = 58$ mW per beam, a $1/e^2$ radial beam waist $\omega_0 = 1.5$ mm, and a single-photon detuning $\Delta = 2\pi \times 90$ GHz blue of the $|F = 2\rangle \rightarrow |F' = 3\rangle$ transition. These parameters yield a lattice depth of ~ 40 recoils.³⁹

To adiabatically load the lattice, we ramp up the beam intensity in 8 ms while the downward laser's frequency is chirped to compensate for gravity (the lattice is at rest in the atoms' freely-falling frame as the intensity is ramped up). For a full-height (8.5 m) launch,⁴⁰ we then chirp the upward laser's frequency at $50g$ for 29 ms to accelerate the atoms up to 13 m/s.⁴¹ We then ramp down the lattice intensity, again over 8 ms while the downward laser compensates for gravity. The total height needed for the acceleration phase is 20 cm.

2.4.2 Lattice Beam Geometry

The lattice beams are arranged in a “W” configuration, as shown in Fig. 2.7(b). This configuration has several benefits.⁴² First, since the lattice beams need only interact

³⁹For a lattice generated by retroreflection of a laser with a single-beam peak intensity $I_0 = \frac{2P_0}{\pi\omega_0}$, the spatially varying lattice intensity is $I(r, z) = 4I_0 e^{-2(r/\omega(z))^2} \cos^2(2\pi z/\lambda)$. This yields a potential $U(r, z) = \frac{\hbar}{4\Delta} \frac{\Gamma^2}{2} \frac{I(r, z)}{I_{\text{sat}}}$ via the Stark shift [74]. The lattice depth in recoils is then $U(0, 0)/E_r$, where the recoil energy is $E_r = \frac{(\hbar k)^2}{2m}$.

⁴⁰It is possible to launch the atoms up to ~ 9.5 m before they collide with the in-vacuum primary lens (Fig. 2.10), but they then leave the well-shielded interferometry region. Launching to 9.4 m or more is necessary for imaging with the upper camera (Fig. 2.1).

⁴¹Just prior to acceleration by the lattice, the atoms have a downward velocity of ~ 1 m/s, so the velocity change imparted by the lattice is actually 14 m/s. The downward initial velocity results from the downward velocity of the atoms at the end of the magnetic lens (Fig. 5.5) and from gravitational acceleration during the free-fall period before the lattice acceleration (this free-fall period includes the 60 ms delay for state preparation, Section 2.3.6).

⁴²One disadvantage to the “W” configuration is that there is a limited region of overlap of the downward- and upward-going beams [the diamond in Fig. 2.7(b)]. The opening angle of the lattice is

with the atoms at the bottom of the tower, they can have a smaller beam waist than the atom optics beams. Introducing them off-axis facilitates focusing the lattice beams to a $1/e^2$ radial waist of $\omega_0 = 1.5$ mm at the retroreflection mirror. This allows for high lattice depths with modest laser powers. Introducing the lattice beams off-axis also allows them to bypass the upper quarter-wave plate (Fig. 2.7) so that they can be linearly polarized while the primary beams are circularly polarized.

Another benefit to the “W” configuration is that there is no parasitic lattice. In a perfect retroreflection configuration with two beams input from above [see for example Fig. 2.7(a), ignoring the circular polarization], two lattices would be formed (beam 1 downwards interfering with beam 2 upwards, and vice versa). For atoms initially at rest, one of these lattices launches the atoms upwards, but the second, parasitic lattice would launch the atoms downwards. For atoms trapped in the correct lattice moving at a finite velocity, the parasitic lattice is Doppler detuned. However, whenever the atoms transition through being at rest in the lab frame, both lattices would become resonant, yielding an effective beamsplitter, and half of the atoms would be lost.

Furthermore, even when Doppler-detuned, the parasitic lattice would contribute to atom loss via spontaneous emission. The “W” configuration ensures that only one downward beam and one upward beam interact with the atoms. In particular, this facilitates the full benefits of blue-detuning suppression (Section 2.4.3). By operating the lattice with blue single-photon detunings, the atoms accumulate at the nodes of the lattice. As a result, the effective intensity is smaller, and spontaneous emission losses are reduced.

The “W” configuration maintains many of the benefits of a retroreflection configuration. The beams originate from the same fiber with crossed polarizations and are separated by a walk-off prism (Fig. 2.14). As a result, their beam profiles are nearly identical. Further, the launch angle is set by the normal vector to the retroreflection mirror and the relative angle between the two downward-going beams, but is insensitive

$\theta_{\text{lat}} = \frac{2 \text{ cm}}{10 \text{ m}} = 2 \text{ mrad}$. We can estimate the vertical height of the overlap region as $h_{\text{lat}} = \frac{\omega_0}{\theta_{\text{lat}}} = 75 \text{ cm}$, which is substantially longer than the 20 cm height needed for a typical launch. Similarly, the spacing between the beams at the bottom is $3.7 \text{ mm} \approx 2.5\omega_0$. Thus, at a distance of ω_0 from the center of the overlap region the beams on the outside of the “W” are reduced from their maximum intensity by $e^{-2(\frac{2.5\omega_0 - \omega_0}{\omega_0})^2} \approx 1\%$.

to the absolute alignment of the beam pair.⁴³ The mirror angle is set by in-vacuum closed-loop precision piezo actuators, and the input beam parallelism is set by the walk-off prism. Both therefore contribute to the stability of the launch angle.

2.4.3 Optimizing Lattice Launch Parameters

As with the atom optics lasers (Section 2.2.3), the detuning and intensity of the lattice lasers must be chosen to minimize atom losses during the launch. Again, there is a balance between Rabi frequency (the lattice depth and corresponding Landau-Zener losses) and spontaneous emission that favors large detunings and high intensities. Because the atoms are trapped in the deep lattice during launch, there is also a detuning-dependent suppression or enhancement of the spontaneous emission rate. For blue lattice detuning, the atoms are trapped at nodes of the standing wave, and spontaneous emission is suppressed. For red lattice detuning, the atoms are trapped at the regions of maximum intensity, and spontaneous emission is enhanced. While the full lattice launching process is somewhat complicated [96, 97], we can get a rough estimate of the loss rates as in [20].

The scattering rate due to spontaneous emission from a single beam with intensity I_0 and detuning Δ was given in Eq. 2.3, which I repeat here:

$$R_{\text{sc}} = \frac{\Gamma}{2} \frac{(I_0/I_{\text{sat}})}{(2\Delta/\Gamma)^2} \quad (\text{single beam, } \Delta \gg \Gamma). \quad (2.17)$$

For blue detuning, we can account for the suppression of spontaneous emission by finding the expectation value of the intensity $\langle I \rangle$ experienced by an atom in the lattice

⁴³This ignores dipole lensing from the AC Stark shift of the lattice beams, which can give the atoms a transverse kick if the “W” is not well centered. Imperfect alignment also changes the effective lattice depth, which is optimized to balance spontaneous emission and Landau-Zener tunneling (Section 2.4.3). We find that it is necessary to make daily adjustments to the lattice alignment with picomotor piezo linear actuators (Newport 8301NF) on the final lattice-delivery turning mirrors [Fig. 2.14(a)]. Recentering the beams on a quadrant photodiode below the retroreflection mirror is typically sufficient.

ground state. The suppression factor is⁴⁴

$$\eta_{\text{lat}} \equiv \frac{\langle I \rangle}{I_0} = \frac{2}{\Gamma} \frac{2\pi}{\lambda} \sqrt{\frac{\hbar\Delta}{m}} \sqrt{\frac{I_{\text{sat}}}{I_0}} \quad (\text{blue-detuned pure lattice}). \quad (2.18)$$

Our lattice is not a perfect standing wave. While the upward- and downward-going beam intensities were balanced to a few percent for the data presented in this section, the orientation of the linear polarizations of the two beams was not ideal (the polarization axes differ by $\theta = 29^\circ$, see Fig. 2.7).⁴⁵ As a result, the on-axis intensity profile has a traveling wave component in addition to the lattice:

$$I(z) = 4I_0 \sin^2\left(\frac{\theta}{2}\right) + 4I_0 \sin^2\left(\frac{2\pi}{\lambda}z\right) \left(\cos^2\left(\frac{\theta}{2}\right) - \sin^2\left(\frac{\theta}{2}\right)\right). \quad (2.19)$$

The spontaneous emission reduction factor (Eq. 2.18) is therefore slightly reduced:

$$\eta_{\text{tot}} = 4 \sin^2\left(\frac{\theta}{2}\right) + \eta_{\text{lat}} \sqrt{\cos^2\left(\frac{\theta}{2}\right) - \sin^2\left(\frac{\theta}{2}\right)} \quad (\text{blue detuning}). \quad (2.20)$$

A similar expression can be found for the red detuning spontaneous emission enhancement factor:

$$\eta_{\text{tot}} = 4 \sin^2\left(\frac{\theta}{2}\right) + (4 - \eta_{\text{lat}}) \sqrt{\cos^2\left(\frac{\theta}{2}\right) - \sin^2\left(\frac{\theta}{2}\right)} \quad (\text{red detuning}). \quad (2.21)$$

In either case, the fraction of the atoms surviving the launch without undergoing a spontaneous emission event is

$$f_{\text{sp}}^{\text{surv}} = \exp(-\eta_{\text{tot}} R_{\text{sc}} \delta t_{\text{lat}}) \quad (2.22)$$

where δt_{lat} is the duration of the lattice launch (accounting for the intensity ramp-up

⁴⁴Near a minimum of the lattice intensity, the lattice potential can be approximated as a simple harmonic oscillator: $U \approx \frac{1}{2}m\omega_{\text{osc}}^2 z^2$, where ω_{osc} can be determined from the Stark shift (Eq. 2.6) and a Taylor expansion of the lattice intensity profile. The expectation value of the potential is then $\langle U \rangle = \frac{1}{4}\hbar\omega_{\text{osc}}$. $\langle I \rangle$ can then be found from the Stark shift, $\langle U \rangle = \frac{\hbar}{4\Delta} \frac{\Gamma^2}{2I_{\text{sat}}} \langle I \rangle$. This analysis assumes both that there are no spectator beams (a benefit of the “W” geometry) and that the lattice beams are single-frequency.

⁴⁵In the future, a waveplate could be added [upper left of Fig. 2.7(b)] to rotate the input polarization to accommodate the fixed axis of the lower $\lambda/4$.

and ramp-down times).

Landau-Zener tunneling also contributes to atom losses. Classically, if the lattice depth is insufficiently large during the acceleration phase, the atoms can slip out of the lattice wells. Quantum mechanical tunneling allows this loss to occur even at larger lattice depths. The Landau-Zener loss rate can be estimated by considering the launch as a sequence of Bloch oscillations [20]. For a launch velocity of v_L , the atoms must pass through $N_L = \frac{mv_L}{2\hbar k}$ avoided crossings, each with a band gap energy of $\hbar\Omega_{\text{bg}} \sim \hbar\Omega_{\text{eff}}$.⁴⁶ The fraction of atoms surviving the launch without Landau-Zener tunneling is

$$f_{\text{LZ}}^{\text{surv}} = \left[1 - \exp \left(-\frac{\pi}{2} \frac{\Omega_{\text{bg}}^2}{\alpha} \right) \right]^{N_L} \quad (2.23)$$

where $\alpha = 2ka_L$ is the frequency chirp rate for a launch with acceleration a_L .

The total number of atoms surviving the launch without Landau-Zener tunneling or undergoing a spontaneous emission event is then

$$f_{\text{tot}}^{\text{surv}} = f_{\text{LZ}}^{\text{surv}} \times f_{\text{sp}}^{\text{surv}}. \quad (2.24)$$

For sufficiently long drift times after the launch, only $f_{\text{tot}}^{\text{surv}}$ of the atoms will remain in the final image. Figure 2.19 shows the theoretical predictions of Eq. 2.24 for three different blue detunings and various lattice intensities. The characteristic Landau-Zener cliff is apparent at low intensities, and spontaneous emission dominates at high intensities. The peak atom survival fraction $f_{\text{tot}}^{\text{surv}}$ increases with increasing detuning Δ , and occurs at higher intensities I_0 for larger detunings.

Figure 2.19 also shows experimental results for launches with several intensities and blue detunings. The data support the simple theoretical model, including blue-detuning suppression. In particular, the ratio of the peak heights predicted without spontaneous emission suppression (dashed curves) is greater than that observed in the data.⁴⁷ At higher intensities, the data fall more quickly than the theory would

⁴⁶The exact band gap can be calculated numerically by solving for the lattice band structure. This has been done in Fig. 2.19 and Fig. 2.20. See also [98].

⁴⁷The spontaneous emission suppression is greatest at smaller detunings where the spontaneous emission rate is higher.

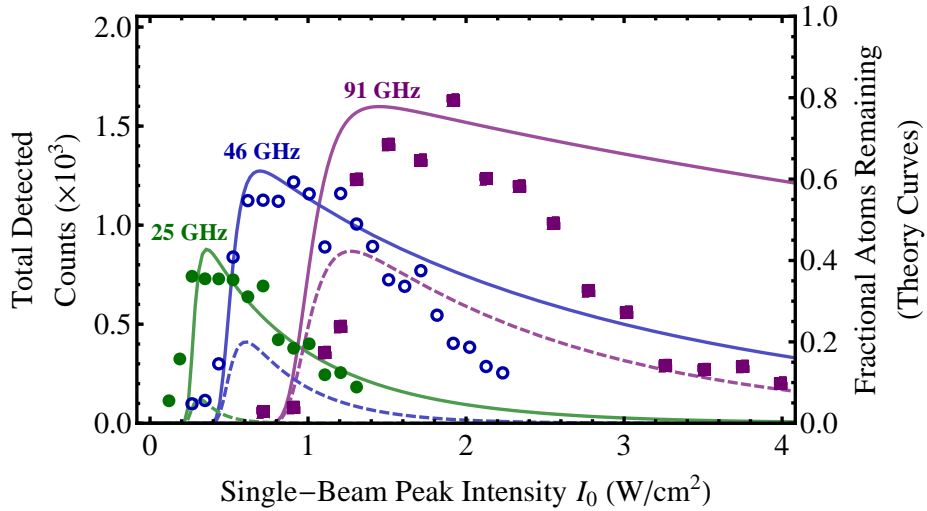


Figure 2.19: Atom number detected as a function of the lattice intensity and detuning. All indicated detunings are blue and are relative to the $|F = 2\rangle \rightarrow |F' = 3\rangle$ transition. Each point is the average of 5 separate experimental trials. A fluorescence imaging pulse 1 ms in duration yields the indicated number of total counts (the peak atom number for the 91 GHz data corresponds to $\sim 10^5$ atoms). The dashed curves are theoretical predictions accounting for Landau-Zener and spontaneous emission losses, but ignoring blue-detuning suppression. The solid curves account for blue-detuning suppression for a lattice in which the upward- and downward-going beam polarization axes differ by 29° . The relative vertical scales for the data and the theory are set by fitting the 25 GHz data to the corresponding solid curve. There are no other free parameters. The “W” configuration is used, and the upward and downward beam intensities are balanced to a few percent.

predict. It is possible that this results from a reduced frequency purity of the lattice beams as the tapered amplifiers (Fig. 2.14) are driven harder, but further study is needed to confirm this.

Figure 2.20 shows data and theoretical predictions for $f_{\text{tot}}^{\text{surv}}$ for 46 GHz red detuning and 46 GHz blue detuning. While the data do not agree perfectly with the model (and the imaging duration is different between the two data sets), it is clear that the red-detuned lattice launch is less effective. Figure 2.20(b) shows the detected atom distribution for red- and blue-detuned launches at optimized lattice intensities. The red-detuned launch yields a much broader distribution (broader than the camera’s viewing region). As a result, peak counts, rather than total counts, are used in Fig. 2.20(a). The broad profile could result in part from spontaneously emitted atoms that have yet to escape the imaging region. Dipole lensing from the lattice beams could also contribute to a change in the detected atom distribution. Since the magnetic lens was optimized for a blue-detuned launch (Section 5.2.3), this could broaden the red-detuned distribution. In this case, the use of peak counts in Fig. 2.20(a) is overly optimistic, and the spontaneous emission enhancement for red-detuning would not be as dramatic as shown.

2.5 Detection

We detect the atoms after they fall back to the bottom of the interferometer region. A vertical fluorescence beam excites the atoms, which radiate via spontaneous emission. Four 4” diameter vacuum viewports, situated above the atom source (see Fig. 2.1), provide substantial solid angle for high-efficiency detection of the radiated light. Spatially resolved imaging of the atom distribution is then achieved with two perpendicular CCD cameras.⁴⁸ The spatial resolution allows us to measure the atom population in both interferometer exit ports (see Fig. 3.3) simultaneously for each experimental trial. Thus, the detection protocol is inherently normalizable and immune to fluctuations in

⁴⁸The CCDs are Quantix Photometrics KAF 6303E. For each camera, a relay lens system is used to image the atom cloud onto the CCD (Fig. 2.21).

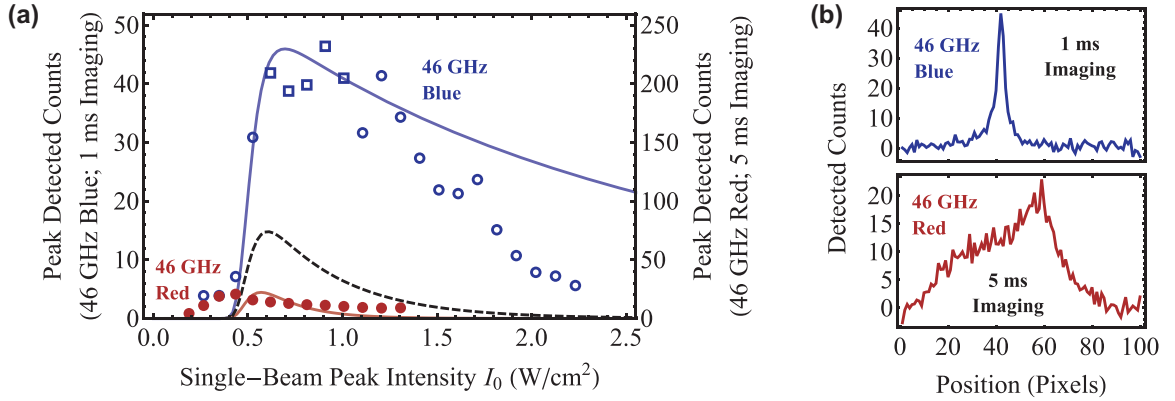


Figure 2.20: (a) Peak counts detected as a function of the lattice intensity for red and blue detunings. All indicated detunings are relative to the $|F = 2\rangle \rightarrow |F' = 3\rangle$ transition. The 46 GHz blue-detuned data are as in Fig. 2.19 (though peak counts are given instead of total counts). Each point is the average of 5 separate experimental trials (3 trials for the red-detuned data). The fluorescence imaging pulse duration is 1 ms for the blue-detuned data, but 5 ms for the red-detuned data (for improved signal-to-noise). As a result, the data are presented with their relative axes scaled by a factor of 5. The black dashed curve is a theoretical prediction accounting for Landau-Zener and spontaneous emission losses, but ignoring detuning suppression/enhancement. The solid curves account for detuning suppression/enhancement for a lattice in which the upward- and downward-going beam polarization axes differ by 29°. The vertical scale for the theory curves is adapted from Fig. 2.19 to account for the switch from total to peak counts (specifically the mean ratio of peak to total counts for the five square points is used). (b) Profiles of the detected atom distribution (the pixel size is 675 μm). For the blue-detuning profile, the lattice launch intensity is 0.62 W/cm². For the red-detuning profile, it is 0.43 W/cm². The full width of the CCD is shown, so vignetting likely contributes substantially to the shape of the red-detuning profile.

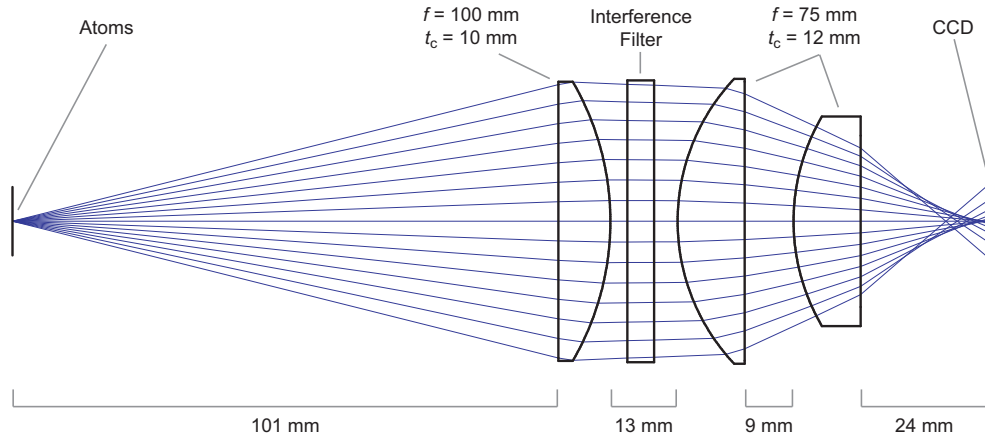


Figure 2.21: Imaging system used in the lower detection region (Fig. 2.1). All of the optics are 2" in diameter. From left to right, the lenses are Thorlabs LA1050-B, LA1145-B, and LA1145-B. The interference filter (Edmund Optics NT65-239) is a 10 nm wide bandpass filter at 780 nm. Spherical aberration is visible in the variation of focal length with input angle. Two identical systems are used to detect the atoms along perpendicular lines-of-sight. A similar system with slightly different lenses is used in the upper detection region.

the launched atom number. Spatial resolution also facilitates time-of-flight temperature measurements and measurements of spatially varying interferometer phase shifts (see Chapters 3 and 4).

The fluorescence imaging light is applied along the vertical axis with the MOT z beam path and lasers. A short repump pulse prior to imaging transfers atoms initially in $|F = 1\rangle$ to $|F = 2\rangle$. The primary fluorescence then results from light 2 MHz red-detuned from the $|F = 2\rangle$ to $|F' = 3\rangle$ cycling transition (cooling). As with the MOT, a small amount of repump light is simultaneously applied to return atoms from the dark state. As a result, atoms in both hyperfine state (both interferometer exit ports) are simultaneously visible.

For state-selective imaging, we apply a short (~ 50 photon recoils) “push” pulse nearly resonant with $|F = 2\rangle$ to $|F' = 3\rangle$. We wait 50 ms for the pushed $|F = 2\rangle$ atoms to spatially separate from the unpushed $|F = 1\rangle$ atoms before imaging. This technique

allows us to more easily resolve the output ports of the interferometer (Fig. 1.1).⁴⁹

The imaging pulse is typically 1-5 ms long. The MOT beams act somewhat like a molasses, nearly halting the atoms' motion during the pulse. For longer durations, the residual motion and heating of the atom cloud increases its apparent size [29], blurring fine features (see Chapter 4).

⁴⁹The output ports are separated by two photon recoils after the final beamsplitter. The push pulse yields splittings in excess of the cloud width in less time, effectively increasing the usable interrogation time T .

Chapter 3

Long-Time Atom Interferometry

In this chapter, I show that light-pulse atom interferometry with atomic point sources and spatially resolved detection enables multi-axis (two rotation, one acceleration) precision inertial sensing at long interrogation times [57]. Using this method, we demonstrate a light-pulse atom interferometer for ^{87}Rb with 1.4 cm peak wavepacket separation and a duration of $2T = 2.3$ s. The inferred acceleration sensitivity of each shot is $6.7 \times 10^{-12}g$, which improves on previous limits by more than two orders of magnitude. We also measure the Earth’s rotation rate with a precision of 200 nrad/s.

3.1 Point Source Interferometry (PSI)

Light-pulse atom interferometry enables precision tests of gravity [5, 14, 23] and electrodynamics [7] as well as practical applications in inertial navigation, geodesy, and timekeeping. Phase shifts for light-pulse atom interferometers demonstrate sensitivity to the initial velocity distribution of the atom source, often resulting in inhomogeneous dephasing that washes out fringe contrast [8]. We show that use of spatially resolved imaging in combination with an initially spatially localized atomic source allows direct characterization of these phase shifts. We refer to this technique as point source interferometry (PSI).

The contrast loss associated with such inhomogeneous dephasing is not fundamental, but is a consequence of atom detection protocols that average over velocity-dependent

Term	Phase Shift	Size (rad)
1	$k_{\text{eff}}g T^2$	2.1×10^8
2	$2\mathbf{k}_{\text{eff}} \cdot (\boldsymbol{\Omega} \times \mathbf{v}) T^2$	5.1
3	$k_{\text{eff}} v_z \delta T$	3.5
4	$\frac{\hbar k_{\text{eff}}^2}{2m} T_{zz} T^3$	0.44
5	$k_{\text{eff}} T_{zi} (x_i + v_i T) T^2$	0.18
6	$\frac{1}{2} k_{\text{eff}} \alpha (v_x^2 + v_y^2) T^2$	0.04

Table 3.1: Velocity-dependent phase shifts and their sizes assuming the following: $k_{\text{eff}} = 2k = 2 \cdot 2\pi/780$ nm, $T = 1.15$ s, initial velocity spread $v_i = 2$ mm/s (50 nK), initial positions $x_i = 200$ μm, $|\boldsymbol{\Omega}| = 60$ μrad/s, gravity gradient tensor components $T_{zi} = 3075$ E, interferometer pulse timing asymmetry $\delta T = 100$ μs, and wavefront curvature $\alpha = (\lambda/10)/\text{cm}^2$. Note that for $T_{zx}, T_{zy} = 50$ E the size of term 5 is significantly smaller. The acceleration (term 1) and gravity curvature (term 4) phase shifts are shown for reference.

phase shifts. With PSI we establish a correlation between velocity and position and use spatially-resolved detection to form an image of the ensemble that reveals its velocity-dependent phase structure. A simple way to realize this correlation is through ballistic expansion of the ensemble. In the limit that the ensemble size at detection is much larger than its initial size, each atom's position is approximately proportional to its initial velocity. Consequently, any initial velocity-dependent phase shift results in a spatial variation of the interferometer phase, yielding a position-dependent population difference between the two output ports of the interferometer.

An important example of velocity sensitivity is due to rotation of the interferometer laser beams [10, 14]. Rotation at a rate $\boldsymbol{\Omega}$ leads to a phase shift (Table 3.1, term 2) that depends on (v_x, v_y) , the initial transverse velocity of the atom. In a rotating frame, this effect may be interpreted as a Coriolis acceleration. PSI also allows observation of longitudinal velocity-dependent phase shifts in asymmetric atom interferometers [99] (e.g., Table 3.1, term 3 and Section 4.6; in this chapter, $\delta T = 0$ μs).

To demonstrate PSI, we induce a velocity-dependent phase shift in a ^{87}Rb Raman light-pulse atom interferometer. We launch cold atoms from the bottom of a 10-meter tall vacuum enclosure [Fig. 3.1(a)] and apply a three-pulse accelerometer sequence $(\pi/2 - \pi - \pi/2)$ [100]. The first pulse serves as an atom beamsplitter, coherently driving

the atoms into a superposition of states $|F = 1; p\rangle$ and $|F = 2; p + \hbar k_{\text{eff}}\rangle$, where p is the initial momentum, F is the hyperfine level, and $\hbar k_{\text{eff}} = 2\hbar k$ is the momentum difference between the two states. Over the subsequent $T = 1.15$ s interrogation interval, the two parts of the atom's wave function separate vertically by $\frac{\hbar k_{\text{eff}}}{m}T = 1.4$ cm [Fig. 3.1(b)], at which time a mirror pulse reverses the relative momenta and internal states. After an identical drift time, a final beamsplitter pulse interferes the atom wave packets. We then image the atom fluorescence using a pair of CCD cameras located below the interferometry region [Fig. 3.1(c)]. By the time of imaging, 2.6 s after launch, the 50 nK atomic source has expanded to 30 times its original size, establishing the position-velocity correlation necessary for PSI.

We imprint a velocity-dependent phase shift by rotating the atom interferometer laser beam axis at a tunable rate $\delta\Omega$. Figure 3.2 shows typical detected atom distributions for several different values of $\delta\Omega_x$.

The velocity-dependent phase gradient we observe in Fig. 3.2 is proportional to the applied rotation rate (Fig. 3.4). For faster rates, the phase shift is large enough that multiple fringe periods appear across the ensemble. Without spatially resolved detection, averaging over these fringes would yield negligible contrast. With PSI, we realize record duration light-pulse atom interferometry, even in the presence of large rotation rates.

3.2 Apparatus and Methods

3.2.1 Creation of the Atomic Point Source

To create the cold atomic source, we load 4×10^9 atoms from a magneto-optical trap into a plugged quadrupole trap, where we evaporate with a microwave knife [82, 101]. A magnetic lensing sequence in a time-orbiting potential (TOP) trap collimates the atom source in 3D, cooling and expanding the cloud while maintaining high phase space density.¹ The final cloud contains 4×10^6 atoms at 50 nK with an initial radius

¹The procedure is similar in principle to δ -kick cooling [86], but uses the atoms' continuous expansion over ~ 100 ms against a shallow (~ 5 Hz) harmonic trap [102] rather than a short (few ms) impulse [99]. The magnetic fields are rapidly turned off when the atoms have reached their minimum

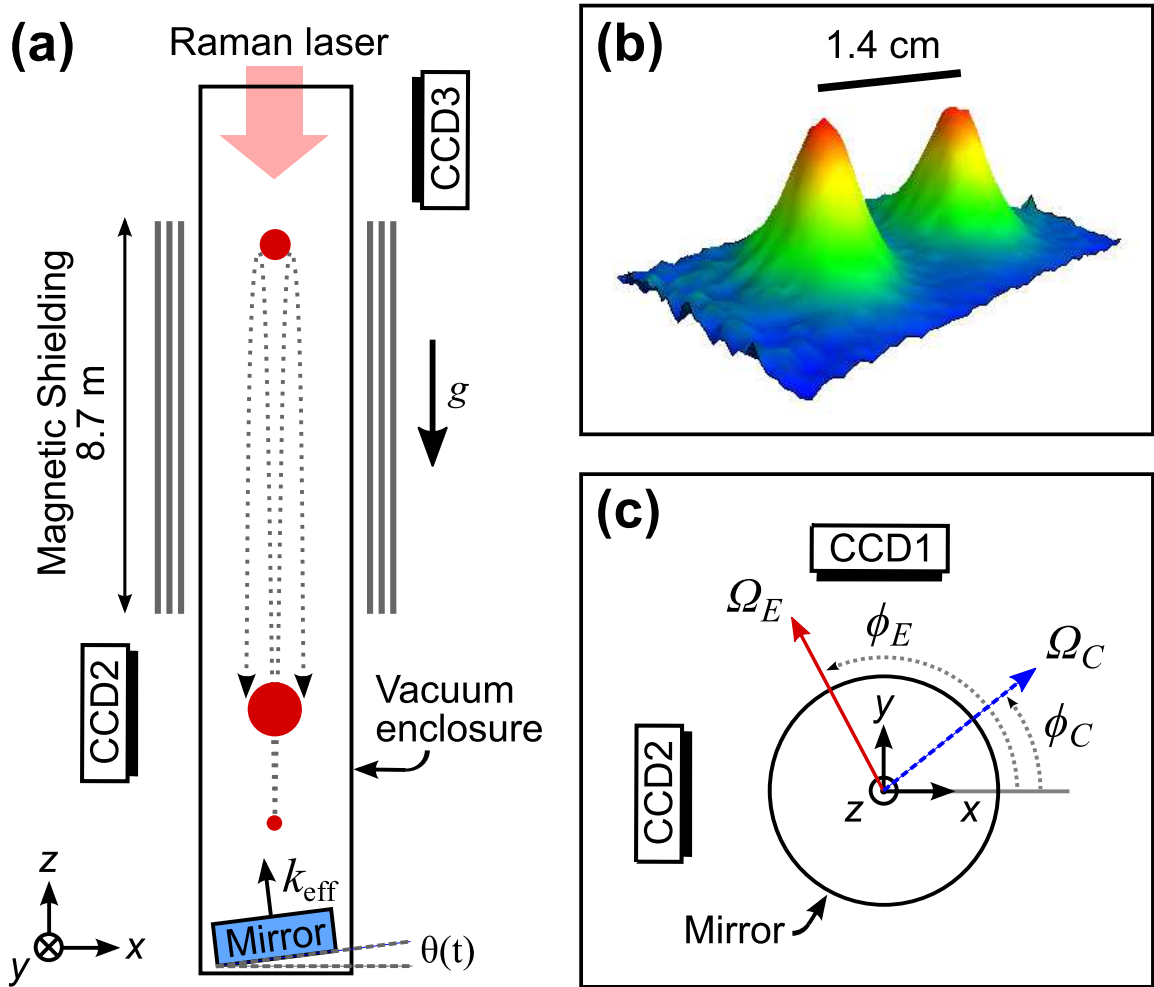


Figure 3.1: (a) Schematic diagram of the apparatus, viewed from the side. The atom cloud (red circle) is cooled and launched from below the magnetically-shielded interferometry region. The two interferometer output ports are imaged by both perpendicular cameras (CCD1 and CCD2). All interferometry pulses are delivered from the top of the tower and are retroreflected off a mirror (at angle $\theta(t)$) resting on a piezo-actuated tip-tilt stage. (b) Image of the ensemble after a beamsplitter pulse showing the separation between two halves of the atomic wavepacket. For this shot we launched the atoms with extra velocity to reach CCD3. (c) Top view of the tip-tilt stage and lower cameras with the direction and magnitude of the Earth rotation Ω_E and an (arbitrary) applied counter-rotation Ω_C . In our apparatus, $\phi_E \approx 105^\circ$.

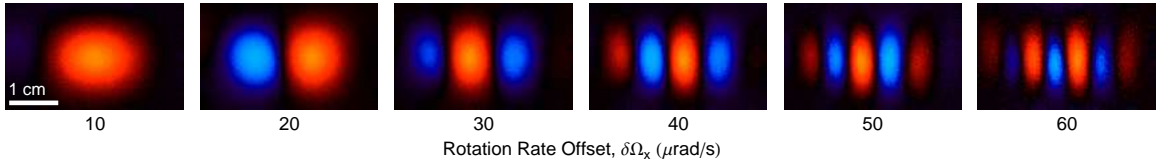


Figure 3.2: Spatial fringes on the atom population observed on CCD2 versus rotation rate offset $\delta\Omega_x$. Blue versus red regions show anti-correlation in atom population. The second output port, with fringes π rad out of phase, is not shown. Each image is the second-highest variance principle component arising from a set of 20 measurements (see Section 3.7).

of $200 \mu\text{m}$. Alternatively, we can produce clouds at 3nK with 10^5 atoms and an initial radius of $30 \mu\text{m}$ by evaporating in a TOP trap with a microwave knife prior to the magnetic lensing sequence.

A microwave pulse transfers the ultracold atoms into a magnetically-insensitive Zeeman sublevel. They are then coherently launched with an optical lattice [95], which transfers 2386 photon momenta with a peak acceleration of 75 g. They enter the interferometer region, a 10 cm diameter, 8.7 m long aluminum vacuum tube. A solenoid wound around the tube provides a bias magnetic field, and three layers of magnetic shielding suppress the environmental field to $< 1 \text{ mG}$ [62].

A small fraction of the atoms are launched into $\pm 2\hbar k$ momentum states. We purify the ensemble's vertical momentum with a $135 \mu\text{s}$ Raman π -pulse, which transfers a 25nK ($0.3 \hbar k$) subset of the ensemble into $|F = 1\rangle$. A short pulse resonant with $|F = 2\rangle \rightarrow |F' = 3\rangle$ blows away atoms that did not transfer.

3.2.2 Two-Photon Raman Atom Optics

A pair of fiber-coupled 1 W tapered amplifiers (TAs) generate the retroreflected interferometer pulses. The seeds for the two TAs are derived from a common source cavity-stabilized to a linewidth of $< 1 \text{ kHz}$ and detuned 1.0 GHz blue from the 780 nm D₂ line ($|F = 2\rangle \rightarrow |F' = 3\rangle$). The seed for one TA passes through a fiber phase modulator that generates the 6.8 GHz sideband necessary for Raman interferometry.

velocity (maximum expansion) in all three dimensions

An acousto-optic modulator (AOM) chirps the other seed to correct for the atoms' Doppler shift. The output of the TAs are combined on a polarizing beamsplitter cube, and the copropagating beams are diffracted by an AOM that acts as a fast optical switch. The beamsplitter and mirror pulses are $35\ \mu\text{s}$ and $70\ \mu\text{s}$ in duration, respectively. The beams have a $2\ \text{cm}$ $1/e^2$ intensity radial waist. The relative power of the two beams is chosen empirically to suppress intensity-dependent detunings by balancing AC Stark shifts (to $< 2\ \text{kHz}$).

3.2.3 Detection

Prior to detection, we spatially separate the output ports by applying a short pulse (~ 50 photon recoils) resonant with $|F = 2\rangle \rightarrow |F' = 3\rangle$. We wait $50\ \text{ms}$ before simultaneously halting and imaging the atoms with a $2\ \text{MHz}$ red-detuned beam. The atoms are nearly at rest after the first $300\ \mu\text{s}$ of the $5\ \text{ms}$ imaging time. The scattered light is collected by two orthogonal CCD cameras, each with a numerical aperture of 0.25 [Fig. 3.1(c)]. The time from initial atom loading to the final image is $20\ \text{s}$.

3.2.4 Rotation Compensation

We precisely control the direction of the interferometer beams with an in-vacuum, piezo-actuated tip-tilt stage onto which the retroreflection mirror is kinematically constrained. The stage has $1\ \text{nrad}$ measured precision and a range of $400\ \mu\text{rad}$. The stage platform is secured kinematically to three nanopositioners (Nano-OP30; Mad City Labs) by stiff springs. The nanopositioners are bolted to the vacuum enclosure, which is anchored to the vibrationally-quiet ($10^{-8}\ g/\sqrt{\text{Hz}}$) concrete floor.

The rotation of the Earth is a significant source of velocity-dependent phase shifts. At our latitude in Stanford, California, the effective rate is $\Omega_E = 57.9\ \mu\text{rad/s}$, which induces fringes of periodicity similar to the highest rotation rate in Fig. 3.2. With the tip-tilt stage we apply a compensating rotation of equal and opposite magnitude ($\boldsymbol{\Omega}_C = -\boldsymbol{\Omega}_E$) to eliminate these phase shifts [8, 14, 103]. We implement this rotation by incrementing the mirror's angle in discrete steps between each interferometer pulse. In Figs. 3.2 and 3.4 we add a variable rotation rate $\delta\Omega_x$ to this nominal rotation

compensation vector.

3.3 High-Contrast Interferometry

3.3.1 Rotation-Compensated Interferometer

Figures 3.3(a) and 3.3(b) show images of both output ports for a rotation-compensated interferometer using two atom source temperatures. The interferometer in Fig. 3.3(a) (3 nK) has an integrated interferometer contrast of 80% while that in Fig. 3.3(b) (50 nK) shows a contrast of 48%.² The contrast is reduced for the hotter source because of Rabi pulse area inhomogeneities due to larger horizontal cloud diameter (with respect to the spatially nonuniform laser beam intensity) and larger Doppler width.

3.3.2 Extended High-Contrast Regime with Spatial Imaging

With PSI, we maintain spatial fringe contrast even in the presence of large net rotation rates (Fig. 3.4). By comparison, the conventional integrated contrast for the same data decays rapidly with increasing rotation rate because a spatial average over the fringe pattern washes out the interference. The reduction in the PSI fringe contrast at higher rotation rates is not fundamental, but results from heating during imaging and imperfect alignment between the applied rotation $\delta\Omega$ and the camera line-of-sight.³

To compute spatial fringe contrast in Fig. 3.4, we divide the fitted amplitude of the population fringes by the fitted amplitude of the underlying cloud (see Section 3.7). While fringes are visible on each raw image, we use Principal Component Analysis (PCA) as a filter to isolate the population fringe from the cloud shape in a model-independent way for more robust fits [104]. The fitted fringe frequency provides the magnitude of the phase gradient.⁴

²Integrated contrast is calculated by summing image counts inside regions of interest around each output port and then forming the normalized population ratios r_i for a set. The contrast of the set is $c = [\text{Max}(r_i) - \text{Min}(r_i)]/[\text{Max}(r_i) + \text{Min}(r_i)]$

³Imaging integrates along the line-of-sight (LOS) of the camera (perpendicular to the CCD chip). For maximum fringe contrast, the spatial fringe wavevector must be perpendicular to the camera LOS, aligning the planes of the population variation with the LOS.

⁴With an optimized imaging protocol, the minimum detectable PSI fringe period is limited by the

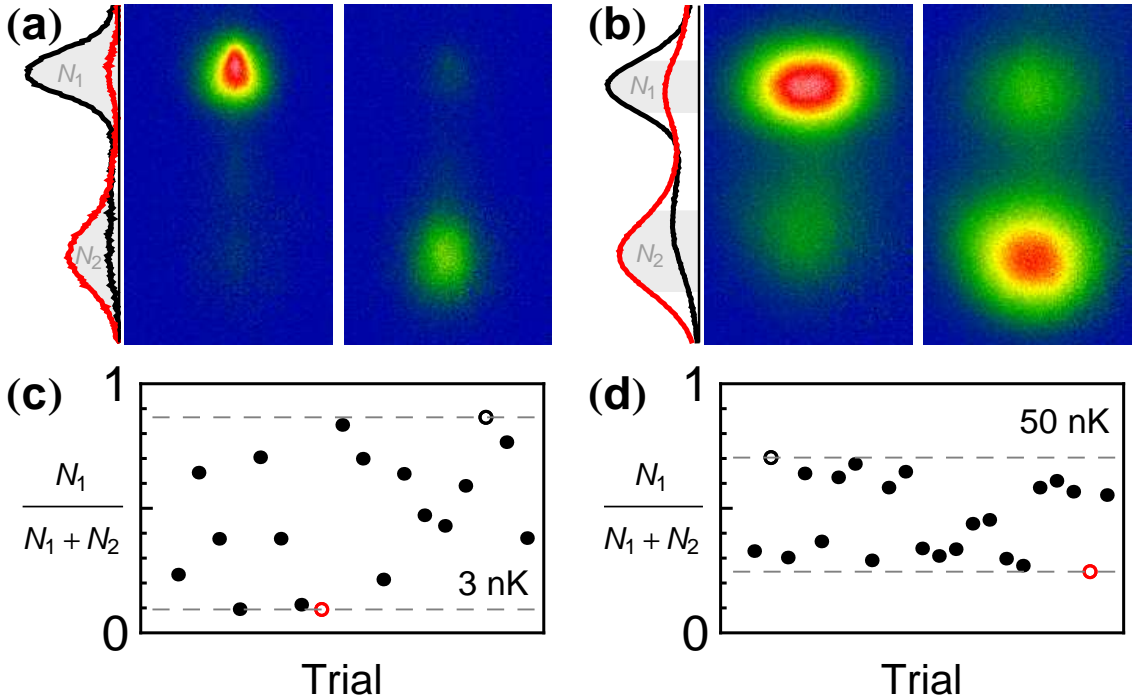


Figure 3.3: Images of the interferometer output ports using (a) 3 nK and (b) 50 nK atom sources with rotation compensation ($\Omega_C = -\Omega_E$). The upper (lower) port consists of N_1 (N_2) atoms in state $|F = 1\rangle$ ($|F = 2\rangle$). Each pair of images represents the two extremes in the observed population ratio, $N_1/(N_1 + N_2)$ (open circles in (c) and (d)). Population ratio variations between trials reflect interferometer phase variations caused by vibration of the retroreflection mirror. Also shown in (a) and (b) are the atom densities integrated horizontally for the two images (black and red curves), with the shaded regions used to determine the port atom numbers, N_i . The lower port has been optically pushed, resulting in a hotter cloud with fewer peak counts. Both ports are heated by a 5 ms imaging pulse. This heating is most evident for 3 nK clouds.

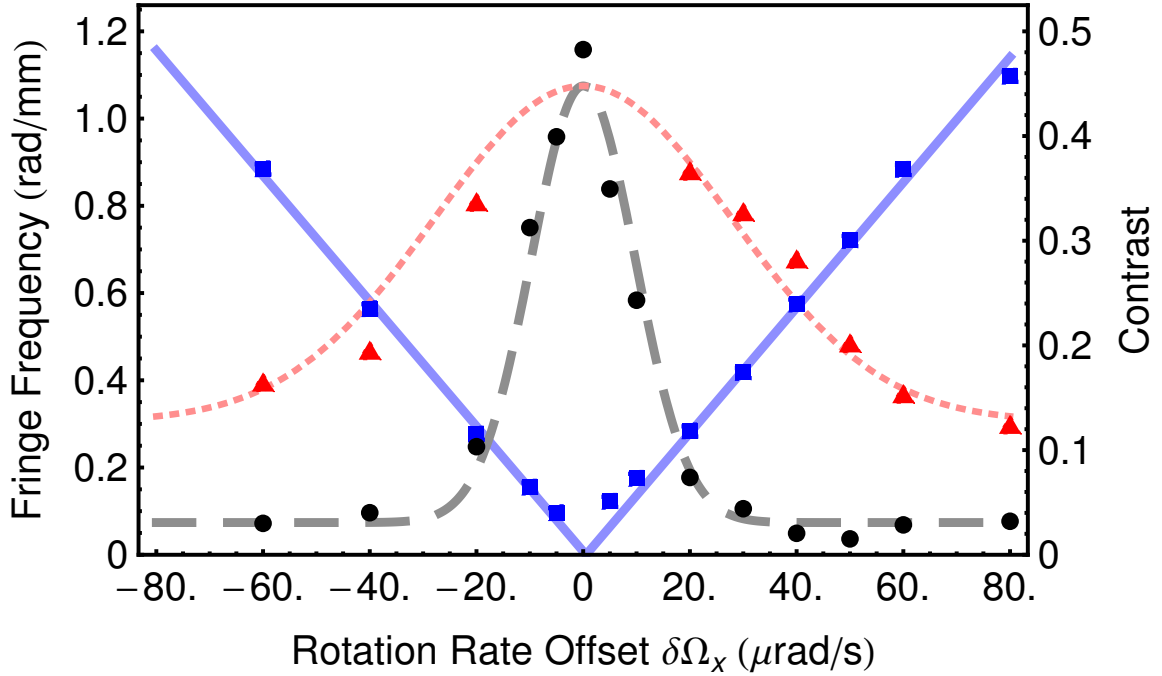


Figure 3.4: Fringe spatial frequency (blue squares, solid line) and contrast versus applied rotation for the data in Fig. 3.2. The fitted slope of the fringe spatial frequency is consistent with term 2 of Table 3.1 to < 10%. Fringe contrast is observed over a wide range of rotation rates (red triangles, dotted line), while the contrast from integration detection decays rapidly (black circles, dashed line). Both Gaussian fits are constrained to be centered at the observed point of zero phase gradient ($\delta\Omega_x \approx 0 \mu\text{rad/s}$), and the fringe contrast fit is further constrained to have the same peak value as the integrated contrast fit, since the methods should agree in the large wavelength limit.

3.4 Multi-Axis Gyroscope

We also measure the rotation rate of the Earth. After coarsely compensating for the Earth's rotation with the tip-tilt stage, we tune the applied rate by adding a small rotation $\delta\Omega_E \equiv \Omega_C - \Omega_E$ along the nominal direction of true North ($\phi_C \approx \phi_E + \pi$). We observe the resulting phase gradient simultaneously on CCD1 and CCD2. The magnitude of the observed phase gradient depends on the projection of the net rotation rate onto each camera [see Fig. 3.1(c)]. To detect small phase gradients that generate less than 2π radians of phase across the ensemble, we extract the differential phase $\Delta\Phi_{LR}$ by splitting each image about a vertical line and analyzing the left and right halves as independent interferometers.

Figure 3.5(a) shows $\Delta\Phi_{LR}$ as a function of $\delta\Omega_E$ as observed on CCD1 and CCD2. Each measurement is the result of 20 interferometer cycles. We parametrically plot the population ratio of the left half versus the right [e.g., Fig. 3.5(b)] and extract the differential phase and contrast using an ellipse fitting procedure [105].⁵ The horizontal intercept of a linear fit to this data provides a measurement of Earth's rotation rate with a precision of 200 nrad/s.

The difference in the intercepts observed by the two cameras indicates that the rotation compensation direction ϕ_C is slightly misaligned from true North ϕ_E such that $\Delta\phi \equiv \phi_C - (\phi_E + \pi) \neq 0$. This results in a spurious rotation ($\Delta\phi\Omega_E \sin\phi_E$) \hat{x} that imprints a phase gradient visible on CCD2 (see Table 3.1, term 2) independent of $\delta\Omega_E$. Likewise, a spurious rotation ($-\Delta\phi\Omega_E \cos\phi_E$) \hat{y} imprints a phase gradient visible on CCD1. The slopes for the two cameras in Fig. 3.5 are different because of unequal projection of Ω_E and small differences in the projected widths of the ensemble.

initial cloud size (300 μm in this work). Our imaging process limits the minimum detectable fringe period to ~ 1 mm (e.g., due to heating effects).

⁵Occasional trials (< 5%) that display no interference appear at the center of the ellipses and are rejected. These trials are clearly distinct from those on the ellipses, and result from experimental glitches (e.g., a loss of laser lock).

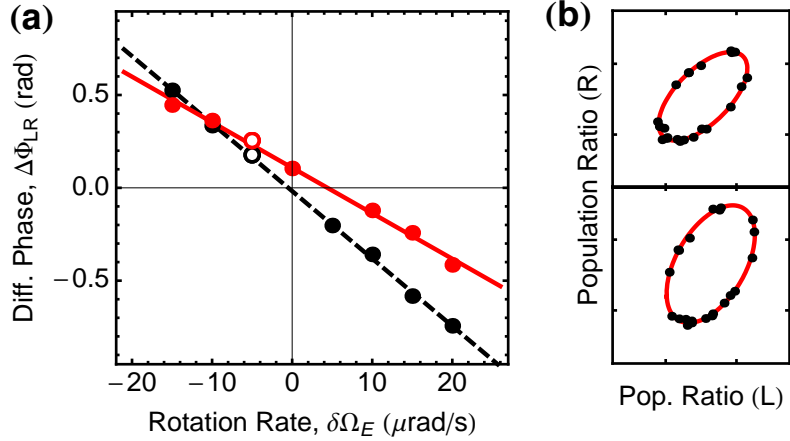


Figure 3.5: (a) PSI dual-axis gyroscope. We extract the differential phase $\Delta\Phi_{LR}$ between the left and right sides of the ensemble as a function of the rotation rate $\delta\Omega_E$, as measured on cameras CCD1 (black, dashed) and CCD2 (red, solid). (b) Sample ellipses emerging from the right-versus-left population ratios of CCD2 (upper) and CCD1 (lower), corresponding to the open circles of part (a).

3.5 Differential Accelerometer Sensitivity

Although the mean interferometer phase is dominated by seismic noise contributions at long T , we can infer an acceleration sensitivity using the observed differential phase noise between different parts of the imaged cloud. Rather than compare the left half versus the right half as we did in the gyroscope analysis, we instead divide the output ports in two using a checkerboard pattern and study the differential phase between the combined even and combined odd grid squares. Varying the grid size s in this analysis reveals correlated phase noise at different spatial scales.⁶ Analyzing 280 trials with $\Omega_C \approx -\Omega_E$, we find the differential even-odd phase noise is 2.0 mrad per shot for grid sizes from $s = 3$ mm down to 0.7 mm, the smallest size analyzed. Combined with the acceleration response (Table 3.1, term 1), this implies an acceleration sensitivity of $6.7 \times 10^{-12}g$ in one shot,⁷ an improvement of more than two orders of magnitude

⁶To ensure that results are independent of the initial grid registration, we compute two grid alignment quadratures (analogous to sine and cosine) for each dimension by offsetting the grid by $s/2$ in each direction. We then average over alignment using the root mean square of these four results.

⁷The sensitivity is $\delta a/g = \delta\phi/k_{\text{eff}}gT^2$, where $\delta\phi = (2.0 \text{ mrad})/\sqrt{2}$ is the absolute phase noise combining all the atoms from both the even and odd grid squares. Since a single trial takes 20 s, this

over previous limits [106]. By comparison, the atom shot-noise limit for the 4×10^6 atoms used in this interferometer at 50% contrast is $\sim 4 \times 10^{-12} g$ in one shot. Note that this grid analysis rejects low spatial frequency variations of the phase across the cloud that originate, for example, from fluctuations in initial kinematics. The results are applicable to measurements where these effects are expected to be common, such as for overlapped ensembles of two species of atoms in an equivalence principle test.

3.6 Applications

PSI does not require a 10-meter apparatus. A dual-axis gyroscope with shot-noise-limited rotation noise of $100 \mu\text{deg}/\sqrt{\text{hour}}$ can be realized with 10^6 atoms prepared at 3 mK in an interferometer with $T = 10 \text{ ms}$ and $4\hbar k$ atom optics cycling at 25 Hz (with atom recapture).

PSI can measure the interferometer beam optical wavefront in situ. This is desirable in precision atom interferometry applications, including gravitational wave detection [45]. Each atom in an expanding ensemble samples the laser phase at three locations, thereby measuring wavefront aberrations. Term 6 of Table 3.1 models the interferometer response to a parabolic wavefront curvature of the form $k\alpha(x^2 + y^2)/2$. Our measured phase noise implies a wavefront sensitivity of $\alpha \sim \frac{\lambda}{500}/\text{cm}^2$ in one shot.

Finally, PSI allows measurement of multiple components of the gravitational gradient tensor (Table 3.1, term 5). The sensitivity we report is also sufficient to observe the gravity curvature induced phase shift (Table 3.1, term 4) [107]. Such sensitivity enables precision tests of the equivalence principle and general relativity [14, 23].

3.7 Principal Component Analysis

Principal Component Analysis (PCA) is a statistical analysis procedure that can identify correlations within a data set in a model-independent way [104]. When applied to a set of images, the result is a basis of orthonormal image vectors that spans the initial image set. These basis image vectors are called the principle components, and

per-shot sensitivity corresponds to $3.0 \times 10^{-11} g/\sqrt{\text{Hz}}$

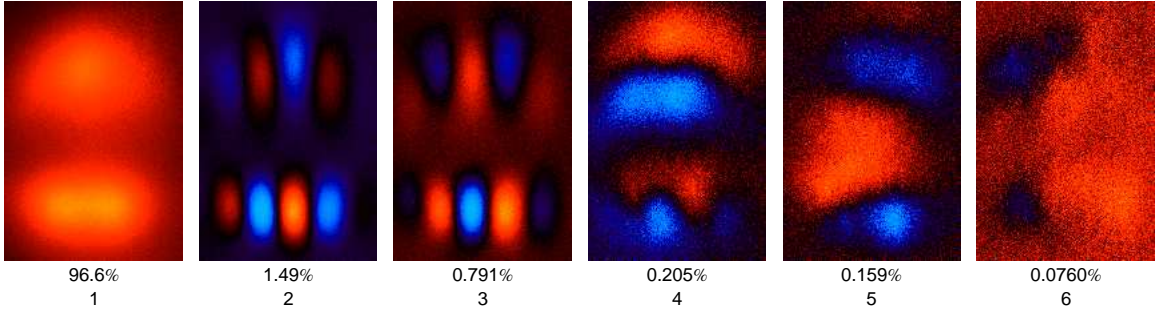


Figure 3.6: Normalized principal components, numbered according to their mean percentage overlap with the original images. These normalized basis images are colored to identify regions of correlation (same color) and anticorrelation (blue versus red). The upper port has been heated by the push used to spatially separate the two ports, resulting in a reduction of the contrast of the fringes in that port.

they are typically ordered by their variance. The higher the variance, or “strength,” the better the basis image accounts for the variability of the set of images as a whole. By projecting a particular image in the original set onto a subspace of the principal component basis, we can isolate different correlations of interest from other correlations or backgrounds [17, 104].

Since interference is an anti-correlation between atom populations between output ports and (in the case of spatially-dependent phase) between neighboring slices within an output port, we can use PCA to distinguish between the constant overall shape of the ports, the interfering atom populations, and sources of technical noise (e.g. camera electronic noise) and systematic noise (e.g. launch velocity or cloud shape jitter).

In Fig. 3.6 we show the first six of 20 principal components for a set of 20 images. For this set, a rotation of $40 \mu\text{rad/s}$ was applied in excess of what was required for rotation compensation. The lower (unpushed) port of the second principal component is also displayed in Fig. 3.2. The first component shows the features most common in all the images of the set: the overall envelope of the two output ports. The next pair of principal components are the two quadratures of the fringe (sine and cosine). Both quadratures emerge as principal components because the input image set consists of images with widely varying overall interferometer phase (the phase is scanned

randomly over multiple radians due to the vibrations of the retroreflection mirror). Any possible interferometer phase can be represented by a weighted sum of these two principal components. Note that given an infinite number of images with uniformly distributed phase, the variance of these two components should be identical; this is not the case for the specific finite data set used for Fig. 3.6 because in this set (by chance) there are more “sine-like” images than “cosine-like” images. Alternatively, given a set of images with a fixed interferometer phase (i.e., no vibration noise), the spatial fringes would appear on the first principal component as a common feature of all the images. Notice that a π phase shift between the two output ports of a single principal component is clearly visible in these images, a signature of interference. The depth of the fringes in the upper port is reduced due to heating from the optical push used to spatially separate the output ports.

PCA can be used as a filter by projecting each image into a subspace spanned by the strongest principal components. The projection onto the first three components (cloud shape, sine fringe, and cosine fringe) typically shows greater than 99% overlap with the original image. The higher principal components may nevertheless contain valuable information. The fourth component in Fig. 3.6, for example, shows a common-mode vertical correlation between the two output ports, indicative of a jitter in the vertical launch velocity of the initial cloud. For higher principal components, however, the spatial frequencies tend to increase until the basis images appear to consist of high-frequency noise (not shown).

We take advantage of the linearity of PCA to robustly estimate the fringe contrast. We project each image in the set both onto (1) the overall cloud envelope (principal component 1) and separately onto (2) the subspace of the cosine and sine quadratures (principal components 2 and 3). We then independently fit these two projections for the un-pushed port, binned vertically to reduce dimensionality. The contrast is then given by the ratio of the amplitudes of those two fits. Fitting the fringe and the envelope separately increases the robustness of the fit by reducing cross-talk between fitting parameters.

We model the general shape of the upper ($P_U(x, z)$) and lower ($P_L(x, z)$) output ports as Gaussians in two dimensions (we have already integrated over the third

dimension in the creation of the 2D image). The expected population distribution within each cloud depends on the interferometer phase, which we allow to vary transversely with x : $\Delta\phi(x) = k_x x + \phi$. If the clouds are well-separated, we can integrate (bin) over the vertical dimension, leaving to good approximation

$$P_U(x) = A_U e^{-\frac{x^2}{2\sigma_x^2}} \left(\frac{1}{2} + \frac{c}{2} \sin [k_x x + \phi] \right) \quad (3.1)$$

$$P_L(x) = A_L e^{-\frac{x^2}{2\sigma_x^2}} \left(\frac{1}{2} - \frac{c}{2} \sin [k_x x + \phi] \right) \quad (3.2)$$

The two output ports differ only by a π phase shift. When we use PCA, we fit each of the two terms in an output port separately. Considering just one port, the population in that port is modeled as

$$P_L(x) = P_1(x) + P_{\text{fringe}}(x) \quad (3.3)$$

$$P_1(x) = A_1 e^{-\frac{x^2}{2\sigma_x^2}} \quad (3.4)$$

$$P_{\text{fringe}}(x) = -A_{\text{fringe}} e^{-\frac{x^2}{2\sigma_x^2}} \sin [k_x x + \phi] \quad (3.5)$$

We then independently fit Eqs. 3.4 and 3.5 to the envelope and fringe projections, respectively. Comparing Eq. 3.3 to Eq. 3.2 we see that the contrast c can be recovered by A_{fringe}/A_1 , the ratio of the amplitude of the fringe to the amplitude of the envelope. The fit to the spatial frequency of the fringe, k_x , is a direct measurement of the phase gradient.

When the wavelength of the fringe is long compared to the cloud size, a fit to the fringe of a single output port cannot accurately determine the spatial frequency and the phase, leading to a mischaracterization of fringe amplitude and the contrast. In this small-gradient regime, ellipse analysis can provide more accurate information about the phase gradient.

Chapter 4

Phase Shear Readout (PSR)

In this chapter, I present a method for determining the phase and contrast of a single shot of an atom interferometer [58]. The application of a phase shear across the atom ensemble yields a spatially varying fringe pattern at each output port, which can be imaged directly. This method is broadly relevant to atom interferometric precision measurement, as we demonstrate in a 10 m ^{87}Rb atomic fountain by implementing an atom interferometric gyrocompass with 10 millidegree precision.

4.1 Atom Interferometry with Spatial Fringes

Light-pulse atom interferometers use optical pulses to split, redirect, and interfere freely-falling atoms [3]. They have proven widely useful for precision metrology. Atom interferometers have measured the gravitational [5, 6] and fine-structure [7] constants, are used in on-going laboratory tests of the equivalence principle [14] and general relativity [28, 35], and have been proposed for use in gravitational wave detection [18, 23]. They have also enabled the realization of high performance gyroscopes [8], accelerometers [9], gravimeters [10], and gravity gradiometers [11].

Current-generation light-pulse atom interferometers determine phase shifts by recording atomic transition probabilities [3]. These are inferred from the populations of the two atomic states that comprise the interferometer output ports. Due to experimental imperfections, interference contrast is not perfect – the dark port never

exhibits complete extinction. It is therefore necessary to independently characterize contrast prior to inferring phase. Typically, this is done with a sequence of multiple shots with different phases, such that the population ratio is scanned through the contrast envelope [16]. Such a protocol relies on the stability of the contrast envelope. In many cases, the contrast varies from shot to shot, introducing additional noise and bias in the phase extraction process.

We present a broadly applicable technique capable of resolving interference phase on a single experimental shot. This is accomplished by introducing a phase shear across the spatial extent of the atom ensemble. The shear is manifest in a spatial variation of the atomic transition probability, which, under appropriate conditions, can be directly observed in an image of the cloud [Fig. 4.1(b)]. Using this phase shear readout (PSR), it is no longer necessary to vary the phase over many shots to determine the contrast envelope. Instead, the contrast of each shot can be inferred from the depth of modulation of the spatial fringe pattern on the atom ensemble. The interferometer phase is directly determined from the phase of the spatial fringe.

PSR fringes reveal rich details about atom interferometer phase shifts and systematic effects, much as spatially varying optical interference patterns yield information about optical systems and their aberrations. The intentional application of a phase shear is analogous to the use of a wedged optical shear plate, where a large applied shear highlights small phase variations across a laser beam [108].

Previous work has employed spatial modulation of the atom population in a variety of atom interferometry experiments [99, 109–115]. Here we use beam pointing to introduce shear in a way that is broadly applicable to existing light-pulse interferometer configurations. In particular, this method does not require Bose-Einstein condensed or ultra-cold atomic sources. Moreover, manipulating and measuring the spatial population modulation facilitates measurements of small phase gradients, as we demonstrate by implementing a precise atom interferometric gyrocompass. Finally, we demonstrate arbitrary control over the phase shear axis by combining laser beam pointing and atom-optics pulse timing asymmetry.

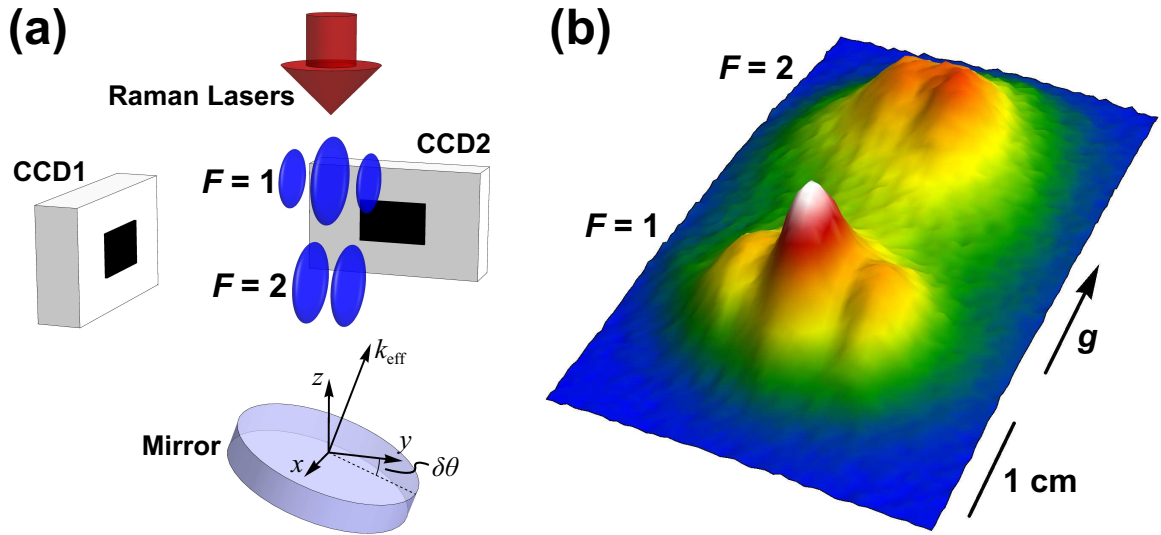


Figure 4.1: (a) Schematic diagram of the apparatus, showing beam-tilt phase shear readout. Atoms are cooled and launched upward into an interferometer region, not shown. Once they fall back to the bottom, the wavepackets are overlapped, yielding an interference pattern (blue fringes) imaged by two perpendicular cameras (CCD1,2). An additional optical pulse separates the output ports ($|F = 1\rangle$ and $|F = 2\rangle$) by pushing the $|F = 2\rangle$ atoms downwards. All atom-optics pulses are performed by lasers incident from above and retroreflected off of a piezo-actuated mirror. Tilting this mirror by an angle $\delta\theta$ for the third atom-optics pulse yields a phase shear. (b) A fluorescence image of the atomic density distribution taken with CCD2 after interference. Spatial fringes result from a third-pulse tilt $\delta\theta = 60 \mu\text{rad}$ about the x -axis. The pushed $|F = 2\rangle$ atoms are heated, yielding reduced apparent contrast, and we ignore the $|F = 2\rangle$ port in subsequent analysis.

4.2 Apparatus and Methods

The apparatus and methods are similar to Chapter 3 [57]. Using evaporative cooling followed by a magnetic lens, we obtain a cloud of 4×10^6 ^{87}Rb atoms with a radius of $200 \mu\text{m}$ and a temperature of 50 nK .¹ These atoms are prepared in the magnetically insensitive $|F = 2, m_F = 0\rangle$ state and launched vertically into an 8.7 m vacuum tube with a chirped optical lattice. They fall back to the bottom after 2.6 s, and we use a vertical fluorescence beam to image them onto two perpendicular CCD cameras (Fig. 4.1).

While the atoms are in free fall in a magnetically shielded region [62], we perform light-pulse atom interferometry with a $\pi/2 - \pi - \pi/2$ acceleration-sensitive configuration with a duration of $2T = 2.3$ s. The atom-optics pulses are applied along the vertical axis using two-photon Raman transitions between the $|F = 2, m_F = 0\rangle$ and $|F = 1, m_F = 0\rangle$ hyperfine ground states (the lasers are detuned 1.0 GHz blue of the $|F = 2\rangle \rightarrow |F' = 3\rangle$ transition of the D₂ line). The atom-optics light is delivered from above and retroreflected off of an in-vacuum piezo-actuated tip-tilt mirror.

The effective wavevector \mathbf{k}_{eff} of the Raman transitions is determined by the pointing direction of the retroreflection mirror [14], which is set for each atom-optics pulse with 1 nrad precision. The mirror has three independent piezo actuators in a tripod configuration that allow arbitrary 2-axis tip-tilt control. We compensate for phase shifts arising from Earth's rotation by applying appropriate tilts for each of the three pulses [14, 57], but additional mirror tilts can be used to induce shear for PSR.

4.3 Beam-Tilt Phase Shear

To generate a controlled phase shear, we tilt the piezo-actuated mirror for the final $\pi/2$ pulse by an angle $\delta\theta$ with respect to the initial two pulses (in addition to the tilts needed for rotation compensation). In the semi-classical limit, the phase shift for a

¹At this low density atomic collisions are negligible.

three-pulse interferometer is

$$\Delta\Phi = \mathbf{k}_1 \cdot \mathbf{x}_1 - 2\mathbf{k}_2 \cdot \mathbf{x}_2 + \mathbf{k}_3 \cdot \mathbf{x}_3 \quad (4.1)$$

where $\mathbf{k}_i \equiv \mathbf{k}_{\text{eff},i}$ is the effective propagation vector at the time of the i th pulse and \mathbf{x}_i is the classical position of the atom [3, 16]. For example, tilting \mathbf{k}_3 by an additional angle $\delta\theta$ about the x -axis yields a phase $\Phi_H = k_{\text{eff}} \delta\theta y_3$ across the cloud, where y_3 is the horizontal position at the third pulse [Fig. 4.1(a)]. This shear is independent of the details of the previous atom-laser interactions and of the implementation of the atomic source (in particular, its spatial extent, temperature, and quantum degeneracy).

Figure 4.1(b) shows an image of the interferometer output with horizontal phase shear. An optical “pushing” pulse, $5 \mu\text{s}$ long and resonant with the $|F = 2\rangle \rightarrow |F' = 3\rangle$ transition, spatially separates the interferometer output ports.² Complementary fringes appear across each port, corresponding to the spatial variation of the atomic transition probability. For linear shears, we can write the phase as $\phi(\mathbf{r}) = \boldsymbol{\kappa} \cdot \mathbf{r} + \phi_0$, where ϕ_0 is the overall interferometer phase and $\boldsymbol{\kappa}$ is the wavevector of the spatially varying component. This implies a spatial modulation of the atomic distribution given by

$$P(\mathbf{r}) = \frac{1}{2} + \frac{C}{2} \sin(\boldsymbol{\kappa} \cdot \mathbf{r} + \phi_0) \quad (4.2)$$

where C is the contrast.

Since the retroreflection mirror can be tilted about an arbitrary horizontal axis, beam-tilt PSR can yield fringe patterns with $\hat{\boldsymbol{\kappa}}$ anywhere in the xy plane, orthogonal to the laser beam axis [see Fig. 4.1(a)]. For instance, it is possible to choose a tilt axis parallel to the line-of-sight of either CCD. We then see a spatial fringe pattern with one camera, but no contrast with the other. Hereafter, we tilt about the x -axis, yielding fringes on CCD2.

The spatial frequency κ of beam-tilt PSR fringes is set by the tilt angle $\delta\theta$. Figure 4.2(b) shows the expected linear dependence. By appropriate choice of $\delta\theta$, the fringe period can be tuned to an arbitrary value (in practice, high spatial frequencies are limited by the depth of focus of the imaging system). Because we detect the atoms

²We spatially separate the output ports because the imaging procedure is not state selective.

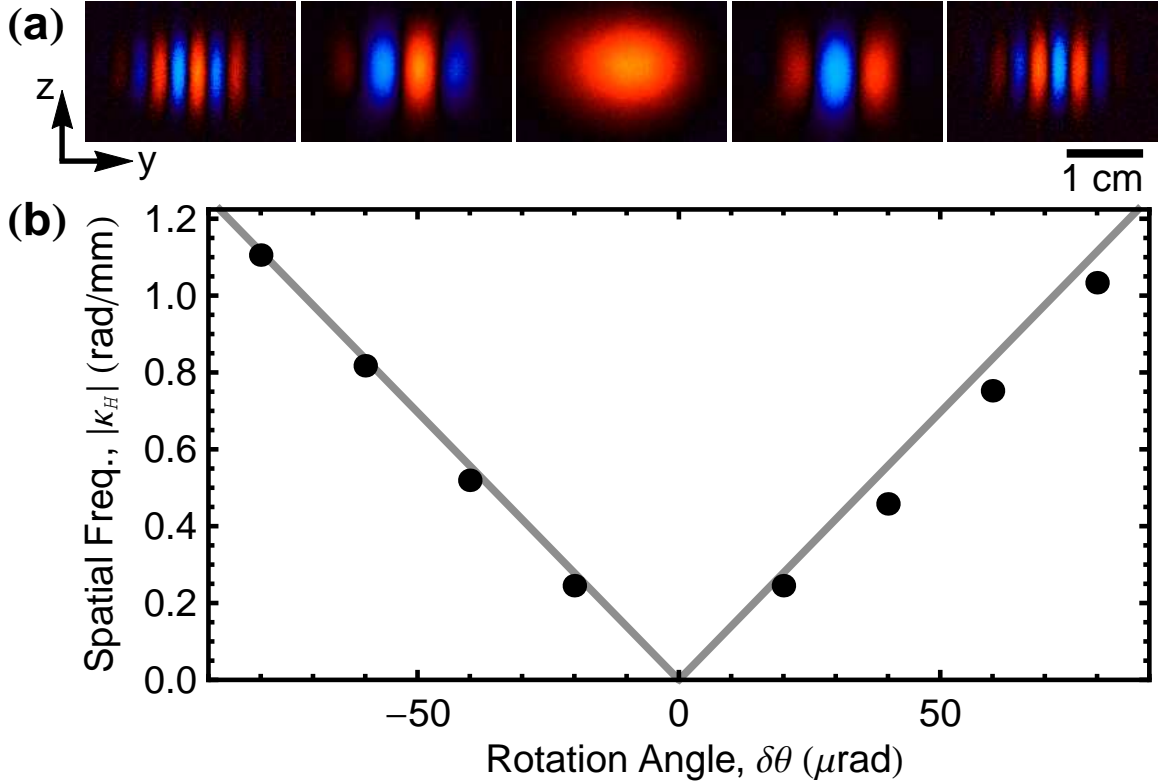


Figure 4.2: Horizontal fringes resulting from beam-tilt PSR in a $2T = 2.3$ s interferometer. (a) Spatial fringes observed on CCD2 with third-pulse tilt angles $\delta\theta = -80, -40, 0, +40, +80 \mu\text{rad}$ (left to right). Red versus blue regions show anti-correlation in atom population. Each image is the second-highest variance principal component arising from a set of 20 fluorescence images [57]. (b) Measured fringe spatial frequency $|\kappa_H|$, resulting from images filtered using principal component analysis [57, 104]. We bin the images vertically and fit a Gaussian modulated by the interference term $P(\mathbf{r})$. The curve is a prediction with no free parameters that includes a reduction in the measured wavelength from heating during imaging. We determine this correction factor with an independent measurement of the fringe spatial frequency versus imaging time. For horizontal fringes, the observed spatial frequency decreases by 5% for 5 ms imaging.

at a final drift time $t_d = 2.7$ s that is later than the third pulse time $t_3 = 2.5$ s (both measured from the time of trap release), we must correct for the continued motion of the atoms. In the limit where the initial size of the atomic source is much less than the final spatial extent of the cloud (point source limit [57]),³ the position at t_d of an atom with velocity v_y is $y \approx v_y t_d \approx y_3 t_d / t_3$. The detected horizontal fringe spatial frequency is then $\kappa_H \equiv \partial_y \Phi_H = k_{\text{eff}} \delta\theta t_3 / t_d$.

4.4 Single-Shot Phase Readout

We demonstrate single-shot phase readout by implementing a short interferometer sequence ($2T = 50$ ms) near the end of the 2.7 s drift time. In this case, the atom cloud has a large spatial extent for the entire pulse sequence. For each shot, we set the interferometer phase with an acousto-optic modulator and read it back using beam-tilt PSR with $\delta\theta = 60 \mu\text{rad}$. Figure 4.3 shows the expected correspondence between the applied and measured phases. The spread in the measured phase is due to technical noise associated with spurious vibrations of the Raman laser beam delivery optics. This spread exceeds 2π at longer interrogation times, but fringe fits still yield a precise phase for each shot.

4.5 Gyrocompass

To show how PSR can enable precision measurements, we implement an atom interferometric gyrocompass in a long interrogation time ($2T = 2.3$ s) configuration. In this case, the Raman laser axis is rotated to compensate Earth's rotation, keeping this axis inertially fixed throughout the interrogation sequence. At the latitude of our lab in Stanford, California, this corresponds to an effective rotation rate of $\Omega_E = 57.9 \mu\text{rad/s}$ about an axis along the local true North vector, which is at an angle $\phi_E \approx 15^\circ$ with respect to the negative x -axis (coarsely determined cartographically). However, a small misalignment $\delta\phi_E \ll 1$ between the rotation axis of the retroreflector mirror

³The point source limit is relevant here only as an imaging artifact, resulting from $t_d > t_3$. It is not necessary for beam-tilt PSR.

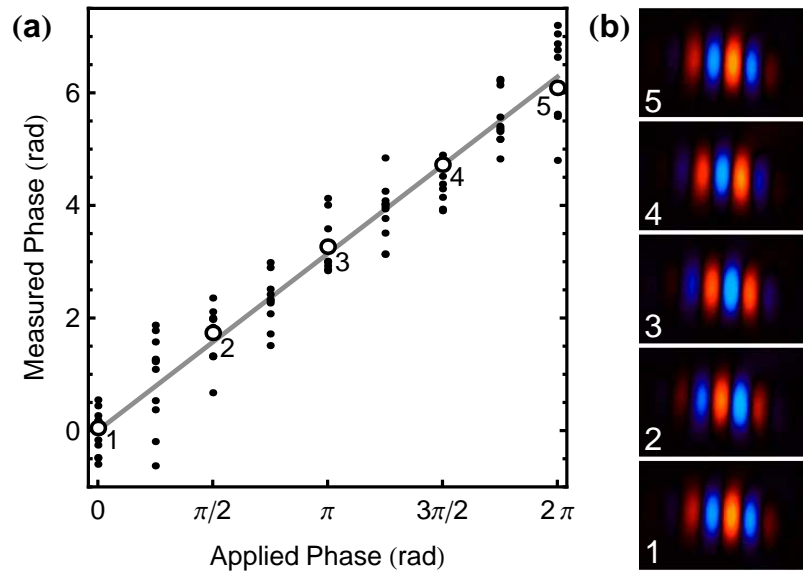


Figure 4.3: Single-shot phase readout with a $2T = 50$ ms interferometer. (a) Measured phase versus the applied phase of the final atom-optics pulse for 96 shots. A line with unity slope is shown for reference. The measured phase is fit from images like those in (b). The measurement scatter is dominated by vibrations of the Raman laser beam delivery optics. (b) Five sample interferometer shots [open circles in (a)], separated in measured phase by $\sim \pi/2$ rad. All images are filtered with principal component analysis.

and true North results in a residual rotation

$$\delta\Omega \approx \delta\phi_E \Omega_E (\sin \phi_E \hat{\mathbf{x}} - \cos \phi_E \hat{\mathbf{y}}) \quad (4.3)$$

that leads to a Coriolis phase shift

$$\Phi_C = 2\mathbf{k}_{\text{eff}} \cdot (\delta\Omega \times \mathbf{v}) T^2 \quad (4.4)$$

that varies across the cloud. As before, in the point source limit $v_y \approx y/t_d$, so the Coriolis phase gradient is

$$\kappa_{C,y} \equiv \partial_y \Phi_C = 2k_{\text{eff}} T^2 \delta\phi_E \Omega_E \sin \phi_E / t_d. \quad (4.5)$$

To realize a gyrocompass, we vary the axis of applied rotation by scanning $\delta\phi_E$, and identify true North with the angle at which $\kappa_{C,y} = 0$.

4.5.1 Differential Heterodyne Measurement

It can be challenging to measure small phase gradients with spatial frequencies $\kappa \ll 1/\sigma$, where σ is the width of the atom ensemble. In this limit, less than one fringe extends across the cloud, so the fringe fitting method in Fig. 4.2(b) cannot be used. Instead, the gradient can be estimated by measuring phase differences across the ensemble (e.g., with ellipse fits [57, 105]), but this procedure can be sensitive to fluctuations in the atomic density distribution (width, position, and shape).

To circumvent these issues, we take advantage of PSR by applying an additional shear that augments the residual Coriolis shear Φ_C . An additional tilt of $\delta\theta = \pm 60 \mu\text{rad}$ about the x -axis is added for the final interferometer pulse. This introduces a horizontal shear Φ_H with approximately 2.5 fringe periods across the cloud, enough to use fringe fitting to extract the spatial frequency. Subtracting off the known contribution of the additional tilt then yields a measurement of the small residual Coriolis shear. This technique of shifting a small phase gradient to a larger spatial frequency is analogous to a heterodyne measurement in the time domain. In both cases, the heterodyne

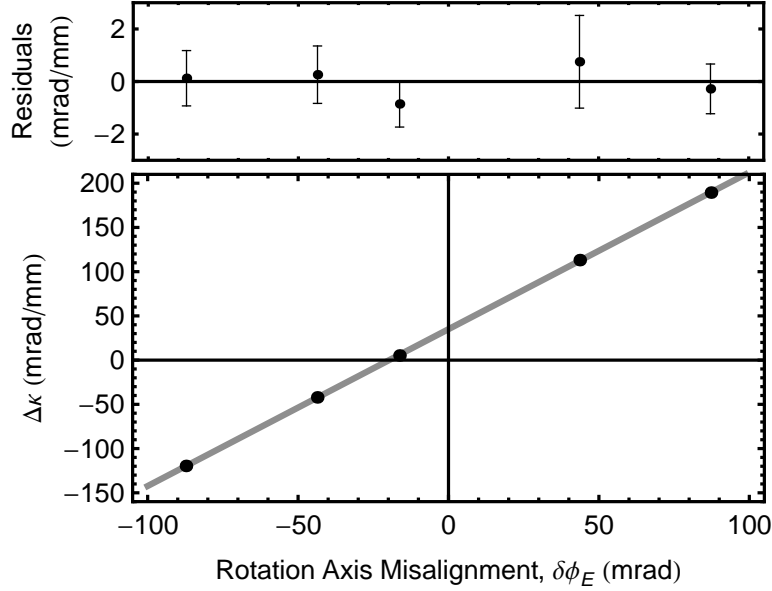


Figure 4.4: Gyrocompass using PSR. Each $\Delta\kappa$ point is the combination of 40 trials, 20 each at two applied tilt values ($\delta\theta = \pm 60 \mu\text{rad}$). The horizontal intercept of a linear fit gives the direction of true North.

process circumvents low frequency noise.

Depending on the sign of the tilt angle, the applied shear adds to or subtracts from Φ_C . The combined phase gradient is then $\kappa_{\pm} \equiv k_{\text{eff}} |\delta\theta| t_3/t_d \pm \kappa_{C,y}$. By alternating the sign of the additional $60 \mu\text{rad}$ tilt and subtracting the results, we realize a differential measurement whereby systematic uncertainty in the applied shear is mitigated: $\Delta\kappa \equiv \kappa_+ - \kappa_- = 2\kappa_{C,y}$, independent of $|\delta\theta|$.

Figure 4.4 shows the expected linear scaling of the differential spatial frequency $\Delta\kappa$ as a function of the applied rotation angle $\delta\phi_E$. A linear fit to the data yields a horizontal intercept that indicates the direction of true North with a precision of 10 millidegrees. An apparatus optimized for gyrocompass performance could achieve similar or better precision in a more compact form factor. Also, this method does not require a vibrationally stable environment since the measurement uses the fringe period, not the overall phase.

4.6 Timing-Asymmetry Phase Shear

Finally, we show how combining beam tilts and interferometer timing asymmetries provides arbitrary control over the spatial wavevector κ of the applied phase shear. While a beam tilt applies a shear transverse to the interferometer beam axis, timing asymmetry yields a shear parallel to the beam axis ($\kappa \parallel \mathbf{k}_{\text{eff}}$) in the point source limit [99]. To create an asymmetric interferometer, we offset the central π pulse by $\delta T/2$ such that the time between the first and second pulses ($T + \delta T/2$) is different from the time between the second and third pulses ($T - \delta T/2$). The resulting phase shift, $\Phi_V = k_{\text{eff}} v_z \delta T$, depends on the atoms' Doppler shift along the direction of \mathbf{k}_{eff} . The phase shear at detection is then $\kappa_V = \partial_z \Phi_V = k_{\text{eff}} \delta T / t_d$. Figure 4.5(a) shows the resulting vertical fringes, which are orthogonal to those from beam tilts [Fig. 4.2(a)] and are simultaneously visible on both CCD cameras. The fitted fringe frequency shown in Fig. 4.5(c) exhibits the expected linear dependence on δT , deviating at low spatial frequency due to the difficulty of fitting a fringe with $\kappa \sim 1/\sigma$.

For vertical fringes, the imaging pulse reduces the detected spatial frequency by stretching the cloud vertically. We independently characterize this stretch by measuring the fringe period as a function of imaging duration τ and extrapolating to $\tau = 0$. The results indicate a fractional stretch rate of $\alpha = 0.12 \text{ ms}^{-1}$. The modified prediction for the spatial frequency is $\tilde{\kappa}_V = \kappa_V / (1 + \alpha\tau)$. With the $\tau = 2 \text{ ms}$ imaging time used, this agrees well with the measurements of Fig. 4.5(c) with no free parameters.

4.6.1 Hybrid Phase Shears in 3D

By combining beam tilt shear κ_H with timing asymmetry shear κ_V , we can create spatial fringes at arbitrary angles. The composite shear is at angle

$$\Theta = \arctan(\kappa_V / \kappa_H) = \arctan[\delta T / (\delta\theta t_3)]. \quad (4.6)$$

Figures 4.5(b) and (d) show fringe images and extracted angles using a $\delta\theta = 40 \mu\text{rad}$ beam tilt combined with a range of timing asymmetries. To find the angles, we

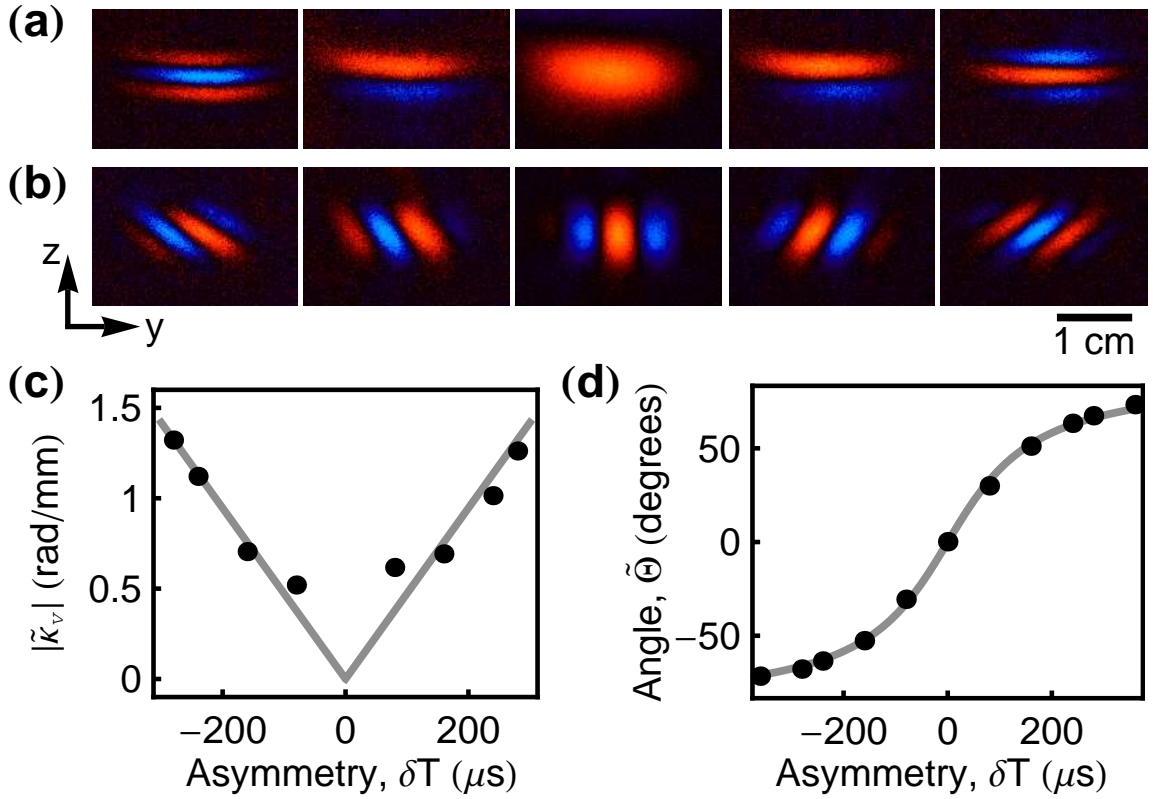


Figure 4.5: Arbitrary control of spatial fringe direction. (a) Second-highest variance principal components from sets of 20 trials with timing asymmetry $\delta T = -240, -160, 0, +160, +240 \mu\text{s}$ (left to right) (b) Comparable images for trials with both a beam tilt $\delta\theta = 40 \mu\text{rad}$ and $\delta T = -160, -80, 0, +80, +160 \mu\text{s}$. (c) Measured fringe spatial frequency extracted from fits to principal component filtered images with vertical fringes. (d) Measured fringe angle extracted from fits to images with tilted fringes. In both (c) and (d) the curves are predictions with no free parameters.

apply Fourier and principal component filters and fit with a two-dimensional Gaussian envelope modulated by an interference term $P(\mathbf{r})$. We again correct for stretching during detection, which affects the measured angles. The modified prediction, $\tilde{\Theta} = \text{arccot} [(1 + \alpha\tau) \cot \Theta]$, shows good agreement with the measured angles of Fig. 4.5(d) with no free parameters.

4.7 Applications

We have demonstrated a precision gyrocompass with PSR, but arbitrary control of the shear angle facilitates measurements of phase shifts and gradients from any origin. For example, a vertical gravity gradient T_{zz} induces a phase shear $k_{\text{eff}} T_{zz} v_z T^3$. This translates the measured angles of Fig. 4.5(d) such that $\Theta = \arctan [(\delta T - T_{zz} T^3) / (\delta \theta t_3)]$. For our parameters, this yields an effective asymmetry of 2 ns/E. PSR also enables measurements of nonlinear phase variations, including optical wavefront aberrations [57]. For precision measurements dependent on absolute phase (gravimetry, atomic recoil measurements, etc.), PSR can suppress systematic error by making phase measurements independent of drifts in the contrast envelope. Finally, we expect PSR to be enabling for future inertial sensors operating on dynamic platforms, where single shot estimation of phase and contrast is vital.

Chapter 5

Lens Cooling

Using a matter wave lens and a long time-of-flight, we cool an ensemble of ^{87}Rb atoms in two dimensions to an effective temperature of less than 50_{-30}^{+50} pK. A short pulse of red-detuned light generates an optical dipole force that collimates the ensemble. We also report a three-dimensional magnetic lens that substantially reduces the chemical potential of evaporatively cooled ensembles with high atom number. These cooling techniques yield bright, collimated sources for precision atom interferometry. By observing such low temperatures, we set limits on proposed modifications to quantum mechanics.

The development of techniques to produce colder atomic ensembles has driven numerous advances in atomic physics, including enhanced capabilities in precision measurement [4, 57, 116], quantum information [117], and quantum simulation [118]. A longstanding goal has been to demonstrate efficient cooling protocols to reach effective temperatures of tens of pK, enabling ultra-precise atomic sensors with applications including geodesy [45], tests of general relativity [22, 99, 106], gravitational wave detection [18, 45], and tests of quantum mechanics [55].

5.1 Optical Dipole Lensing

5.1.1 Delta-Kick Cooling

Evaporative cooling in an adiabatically relaxed trap offers one route to extremely low temperatures [119]. A powerful alternative cooling method,¹ often called delta-kick cooling, is to freely expand an atom cloud and then reduce its velocity spread with a collimating lens [85–92]. Compared to evaporation, lensing typically requires less time and avoids intrinsic atom loss. The lens is implemented by a transient harmonic potential, realized magnetically [87, 102], electrostatically [120], or optically [85]. In previous work, lensing has yielded effective temperatures as low as ~ 1 nK [99, 121].

The potential cooling performance of such a lens depends on the available expansion time. Consider an initial atom ensemble (condensate or thermal state) with RMS size Δx_o and velocity spread Δv_o , allowed to expand for a time t_o before application of the lens potential. The temperature ratio is $\eta \equiv (\Delta v_\ell / \Delta v_o)^2$, where Δv_ℓ is the RMS velocity after the lens is applied. For an ideal harmonic potential that has been tuned to minimize Δv_ℓ (the collimation condition), the expected temperature ratio is bounded by $\eta_c = (\Delta x_o / \Delta x_\ell)^2 \equiv \gamma^2$, where Δx_ℓ is the RMS size of the ensemble when the lens is applied and γ is the size ratio [85]. Correlations between position and velocity in the initial ensemble (e.g., arising from mean field interactions during expansion) can lead to temperatures that are lower than this bound.² Generally, to achieve low temperatures it is beneficial to have a long expansion time so that $\Delta x_\ell \approx \Delta v_o t_o \gg \Delta x_o$.

5.1.2 Optical Dipole Lens

In this work, we use a long expansion time $t_o > 1$ s in a 10 m vacuum tube to demonstrate long-time delta-kick cooling, continuously manipulating the RMS velocity of ensembles of ^{87}Rb atoms through a minimum value of < 70 $\mu\text{m/s}$. This corresponds

¹Here ‘cooling’ is understood to mean effective temperature reduction. The lens does not reduce the ensemble phase space density.

²An initially correlated ensemble corresponds to a virtual source with an effective initial size smaller than Δx_o .

to 50 pK effective temperatures at collimation (we define the effective temperature T by $\frac{1}{2}k_B T = \frac{1}{2}m\Delta v^2$, where m is the atom mass [74]). The dipole lensing potential [74, 85] is generated from the transverse intensity profile of a vertically-propagating Gaussian beam, providing cooling in two dimensions. As a pre-cooling stage, we implement three-dimensional lens cooling using a magnetic potential.

An ideal harmonic lens (frequency ω) exerts a force $F_H = -m\omega^2 x$, where x is the transverse position. For the dipole potential lens, the lens duration δt is short (thin-lens limit, $\omega\delta t \ll 1$), so we may approximate its effect as an impulse that changes the atom's velocity by $\delta v(x) = -\omega^2\delta t x$. The lens focal time is defined as $1/f \equiv \omega^2\delta t$ so that a point source of atoms expanding for time f would be perfectly collimated.

5.1.3 Refocusing to Analyze Pikokelvin Temperatures

At pK temperatures, the time necessary for the ensemble size to noticeably increase can be very long (> 10 s), making time-of-flight expansion an ineffective probe of temperature. To circumvent this, we extend the duration of the dipole-potential lens interaction beyond the collimation condition to refocus the ensemble. As in optics, the minimum achievable image size after refocusing is a measure of the degree of collimation. Thus, we can infer the collimated temperature of the atom ensemble from the refocused cloud size.³

To formalize this relationship, we solve the quantum Liouville equation for the evolution of an arbitrary initial state during the lensing sequence. In the delta-kick limit ($\omega\delta t \ll 1$) this reduces to solving the classical Liouville equation [60, 123, 124]. To account for aberration in the lens, we assume a general $F(x)$ for the lens force. Calculating the expectation values of the velocity width of the distribution after the lens and the position width at detection, we find that the minimum refocused size $(\Delta x_i)_{\min}$ sets a bound on the minimum velocity spread Δv_ℓ achievable at collimation. By this metric, the minimum velocity variance for the lens (including aberrations) can be inferred by:

$$(\Delta v_\ell)^2_{\text{bound}} \equiv \frac{(\Delta x_i)^2_{\min}}{t_i^2} = \Delta v_\ell^2 + \delta A \gtrsim \Delta v_\ell^2 \quad (5.1)$$

³An analogous method has been used to measure the temperature of electron beams [122].

where t_i is the time between the lens and detection ('image time'), and δA arises from lens aberrations present during refocusing. For a wide class of aberrations (including those encountered in this work), δA is positive, so $(\Delta v_\ell)_{\text{bound}}^2$ provides an upper bound on the collimated temperature.⁴

5.1.4 Apparatus and Methods

The cooling performance demonstrated here depends critically on an optics configuration that minimizes aberration by reducing spatial intensity perturbations on the dipole-lensing beam. The beam is spatially filtered by propagation through an optical fiber and collimated to a $1/e^2$ radial waist of $\sigma = 3.4$ mm. Intensity perturbations with spatial frequency κ lead to forces $\propto \kappa$, so high spatial frequency perturbations ($\kappa\sigma > 1$) are particularly detrimental [60]. For example, a 1% perturbation with $\kappa \sim (100 \mu\text{m})^{-1}$ can result in a spurious force comparable in magnitude to the lensing force, substantially heating the cloud. To avoid this, the beam propagates for 16 m or more from the collimation lens (retroreflected after 10.6 m) before interacting with the atoms [Fig. 5.1(b)], allowing high spatial frequencies to diffract from the beam (Fig. 5.2). With $\delta t = 30$ ms and $t_o = 1.1$ s, the lens substantially refocuses the atoms at a time $t_i = 1.8$ s later [Fig. 5.1(d)].

The atom source is a cloud of 10^5 ^{87}Rb atoms with initial RMS size $\Delta x_o = 56 \mu\text{m}$.⁵ and an effective temperature of 1.6 ± 0.1 nK [Fig. 5.1(c)]. To prepare this ultracold source, we evaporate in a time-orbiting potential (TOP) trap [Fig. 5.1(a)] The atoms are further cooled with a magnetic lens (details follow) and prepared in a magnetically-insensitive state. We then launch them upwards into a 10 m vacuum tube with a chirped optical lattice [57].⁶ After 2.8 s,⁷ the atoms fall back down, and we image them with a vertical fluorescence beam onto two CCD cameras (looking from North and West).

⁴Correlations between lens aberrations and the initial atom distribution can yield $\delta A < 0$, but even in the worst case the correction to $(\Delta v_\ell)_{\text{bound}}$ is within our stated uncertainty.

⁵Determined by Gaussian fits to absorption images.

⁶The lattice's depth is 40 times the recoil energy and its $1/e^2$ radial waist is 1.5 mm.

⁷The release from the magnetic trap occurs 100 ms before the end of the lattice launch.

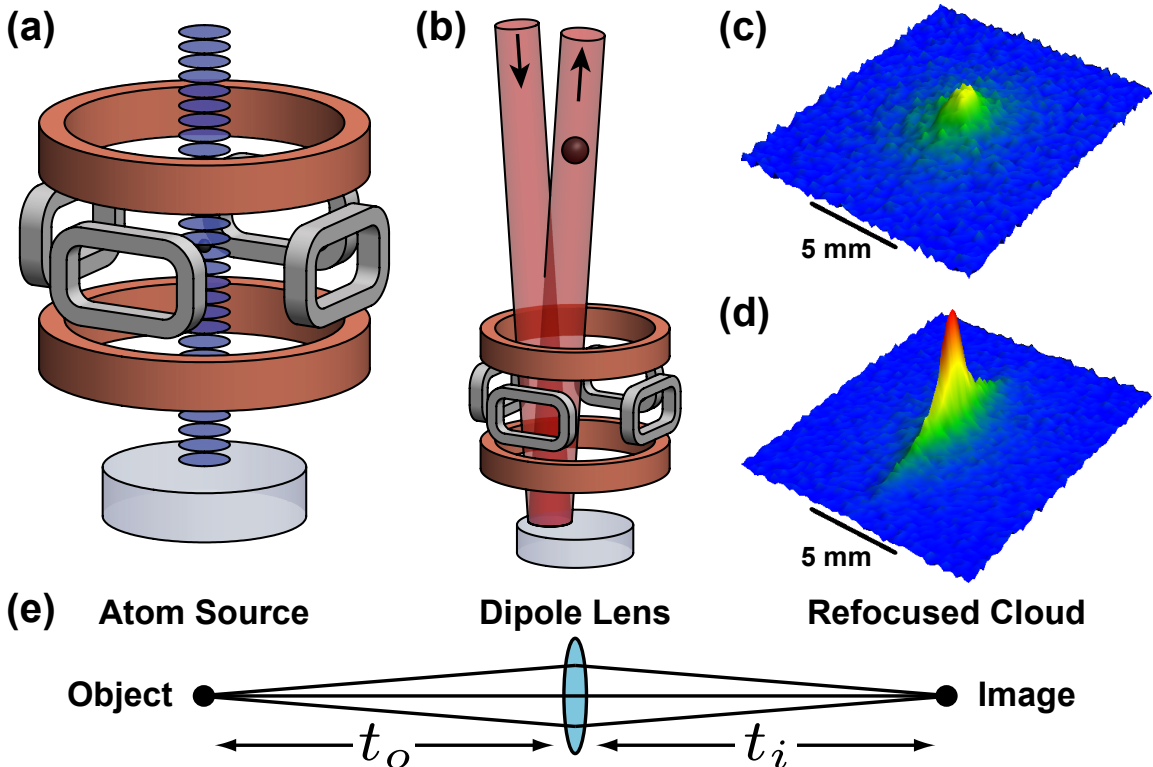


Figure 5.1: (a) Schematic of the apparatus (including vertically-oriented quadrupole trap, horizontal TOP coil pairs, and blue-detuned launching lattice). (b) A 3 W laser, 1.0 THz red-detuned from the ^{87}Rb D_2 line, acts on the atom cloud as a dipole lens (the ~ 1 mrad beam angle is exaggerated for clarity). (c) Fluorescence image of a 1.6 nK cloud after 2.8 s of free fall. (d) The distribution in (c) refocused using the dipole lens. There is no observed axial heating. (e) Optical analogy showing the object, lens, and image, with object distance t_o and image distance t_i .

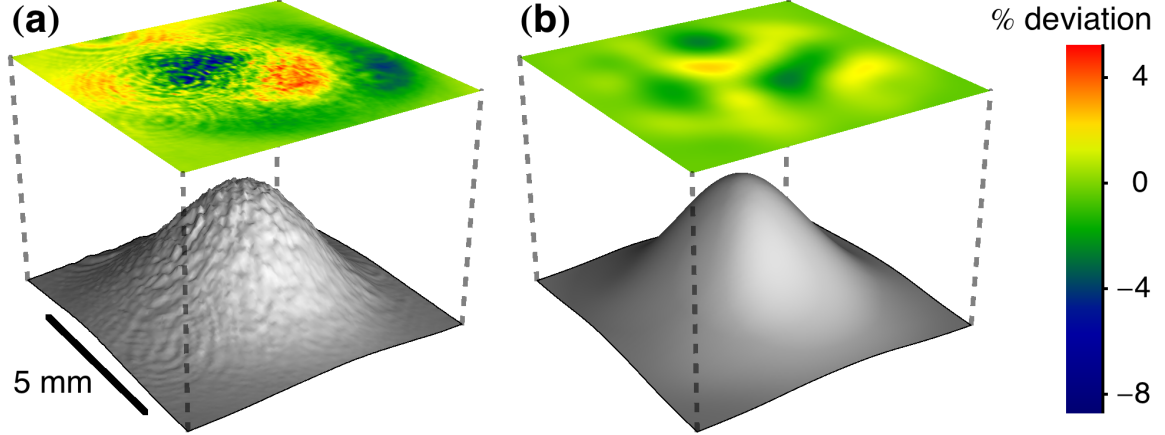


Figure 5.2: Comparison of the dipole lens beam intensity profile after numerical paraxial wave propagation of the measured profile by (a) 0.25 m and (b) 16.25 m. The residuals of fitting a 2D Gaussian are shown above each beam profile.

5.1.5 Refocusing Results

To evaluate the performance of the optical lens, we vary the lens duration and measure the width of the lensed cloud. As the lens acts only transversely, we bin the corresponding images in the vertical dimension and analyze in 1D. Extracting cloud widths requires accounting for the point spread function (PSF) of the imaging system. We fit all imaged clouds to a Gaussian profile convolved with a smooth representation of the PSF [60].

To characterize the PSF, we fit a cloud with a known, small size; this fixes the PSF parameters for subsequent analysis. We use a cloud imaged after a short drift time (100 ms; the time needed to reach the fluorescence imaging region) as the small source [Fig. 5.3(b)]. To directly measure this cloud's size, we image it with a low-aberration imaging system.⁸ The measured width of $90 \pm 10 \mu\text{m}$ is consistent with an extrapolation from the known cloud parameters at the end of the TOP sequence.

Figure 5.3(a) shows the fitted transverse cloud size Δx_i versus lens duration δt for the two camera axes, demonstrating the continuous variation of the atom cloud

⁸This imaging system was not used for primary data collection because of its comparatively poor photon collection efficiency.

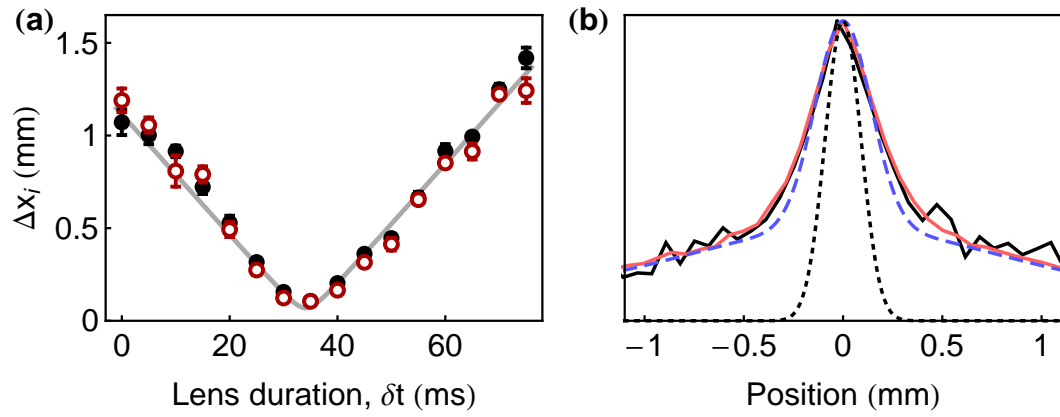


Figure 5.3: (a) Filled black (open red) points denote measured RMS cloud widths on the North (West) camera. Each point is the weighted mean of Gaussian fits to 6 experimental shots. The dashed gray curve is a simultaneous fit to the measurements from both cameras and reports a minimum size of 70 μm at a lens duration of 34 ms. (b) Vertically-binned images comparing the transverse size of a $90 \pm 10 \mu\text{m}$ cloud used to characterize the PSF (solid red/gray) to a cloud refocused 2.8 s later (solid black). The good overlap indicates high-fidelity refocusing. Dotted black: Gaussian profile extracted from a fit of the refocused cloud. The fit accounts for the broadening and distorting effects of the PSF (dashed blue).

through collimation and refocus. For this data, the lens is applied $t_i = 1.8$ s before detection. We fit the data with the predicted cloud size [60],

$$\Delta x_i^2 = (\Delta x_i)_{\min}^2 + \frac{1}{m^2} \Delta F^2 t_i^2 (\delta t - \delta t_{\min})^2 \quad (5.2)$$

where ΔF^2 is a fitting parameter characterizing the variance of the lensing force (including any aberrations), and δt_{\min} is the lens duration to refocus the cloud.

5.1.6 Temperature Bounds

The point at $\delta t = 35$ ms is nearest to the fitted refocusing time and sets the best bound on the achievable collimation temperature T . From Eq. 5.1, we find that $(\Delta v_\ell)_{\text{bound}} \equiv (\Delta x_i)_{\min}/t_i = 65 \pm 20 \mu\text{m/s}$ for the North axis and $70 \pm 25 \mu\text{m/s}$ for the West axis. These bound the effective temperature at collimation to below $T_{\text{bound}} \equiv m(\Delta v_\ell)_{\text{bound}}^2/k_B = 40^{+40}_{-20} \text{ pK}$ and $50^{+50}_{-30} \text{ pK}$ for the North and West axes, respectively. This T_{bound} estimate includes extra heating δA that arises between collimation time δt_c and refocus δt_{\min} . Since heating from aberrations scales as δt^2 , we can estimate T by multiplying the aberration contribution $((\Delta v_\ell)_{\text{bound}}^2 - \gamma^2 \Delta v_o^2)$ by $(\delta t_c/\delta t_{\min})^2 \approx (0.6)^2$, yielding effective temperatures of $30^{+10}_{-10} \text{ pK}$ and $35^{+15}_{-10} \text{ pK}$ for the North and West axes, respectively [60]. The temperature uncertainties result primarily from the standard deviation of the measured cloud sizes, likely caused by shot-to-shot fluctuations in the strength of the lens (e.g., due to fluctuations in optical power or alignment). Uncertainties in the measured PSF do not contribute significantly.

5.1.7 Limits from Initial Size and Gaussian Aberrations

Next, we measure the refocused cloud size $(\Delta x_i)_{\min}$ and corresponding lens duration δt_{\min} for various lens application times t_o , with the total atom drift time held constant (Fig. 5.4). Each point is the result of a fit of Eq. 5.2 to a scan of the lens duration [like Fig. 5.3(a)] at one of four fractional object times: $t_o/(t_o + t_i) = 0.32, 0.39, 0.60$, and 0.71 . Also shown is the ideal harmonic lens scaling for $(\Delta x_i)_{\min}$ and δt_{\min} . Neglecting x - v correlations, the focal time $f_{\min} \equiv (\omega^2 \delta t_{\min})^{-1}$ satisfies the thin lens

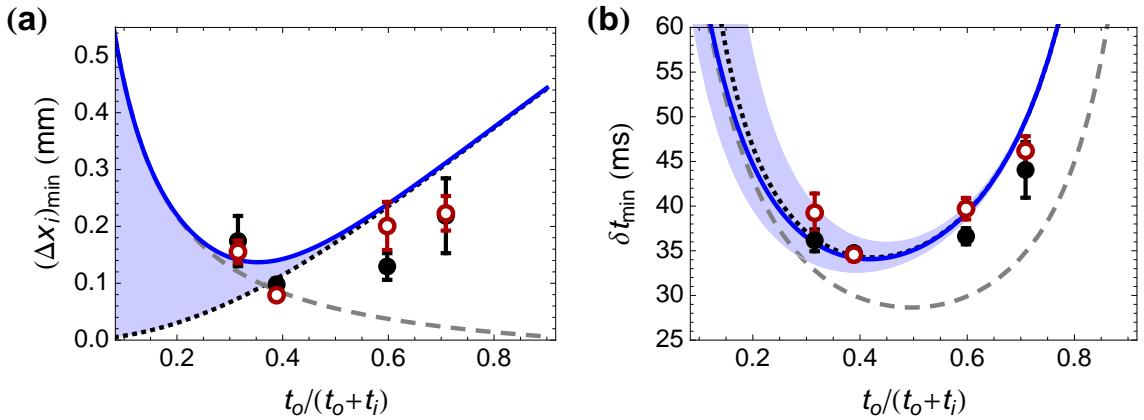


Figure 5.4: (a) Minimum RMS width of the cloud as a function of the fractional object time. (b) The lens duration required to refocus the atom cloud. The filled black (open red) points represent measurements on the North (West) camera. Solid blue: expected behavior for a cloud of finite initial size (56 μm) and no initial $x-v$ correlations in an optical beam with a Gaussian profile. The blue shaded regions represent the corresponding ranges possible with correlations. The curve in (a) has no free parameters. For (b), the optical power is a free parameter that fits to 2.8 W. Dashed gray: expected behavior for an ideal harmonic potential of the same strength as at the center of the beam [60]. Dotted black: expected behavior for a cloud with zero initial size subject to Gaussian aberrations.

formula from geometric optics $\frac{1}{f_{\min}} = \frac{1}{t_i} + \frac{1-\gamma^2}{t_o}$ (the γ correction results from finite velocity spread and vanishes in the point source limit $\gamma \ll 1$)⁹ and the image size $(\Delta x_i)_{\min} = \Delta x_o \frac{t_i}{t_o} \sqrt{1 - \gamma^2}$ scales as the magnification of the lens $\frac{t_i}{t_o}$.

The deviation of the data in Fig. 5.4 from the harmonic lens theory results primarily from large-scale aberrations due to the Gaussian profile of the optical potential. Modeling the lens potential as a 2D Gaussian, we calculate $(\Delta x_i)_{\min}$ and δt_{\min} assuming Gaussian initial ensemble velocity and position distributions (Fig. 5.4) [60]. Although the cooling performance of the lens is partially limited by the finite expansion time t_o , further extending t_o would not improve cooling performance, since a larger Δx_ℓ would increase the effect of Gaussian aberration.

5.1.8 Applications

The ability to transversely cool an atom cloud to very low effective temperatures and to precisely refocus the cloud after long drift times enables many atom optics applications [57, 99]. Refocusing the atoms allows us to extend the effective free-fall time to 5.1 s by relaunching the ensemble. Without refocusing, the cloud is larger than the launch lattice beams, and the relaunch is inefficient. Similarly, a series of relay lenses (or an initial collimation lens) could be integrated with light-pulse atom interferometry to maintain a small transverse cloud size at the beamsplitter pulses, even for very long interrogation times. This would ensure a homogeneous atom optics beam intensity across the cloud, which is critical for large momentum transfer atom interferometry [17].

5.2 Magnetic Lens Cooling

To minimize the impact of anharmonicities of the dipole lensing beam, we pre-cool the atoms with a magnetic lens. This increases the effective $f/\#$ of the dipole lens by reducing the duration δt required for collimation. It has the added benefit of cooling along the third axis not addressed by the dipole lens.

⁹An identical correction arises in optics with a finite source divergence (e.g., a Gaussian laser beam).

5.2.1 TOP Trap Thick Lens

The magnetic lens is performed by abruptly releasing tightly-confined atoms into a shallow harmonic potential provided by a 2.6 kHz TOP trap with spinning bias field B_0 and radial quadrupole gradient ∇B [Fig. 5.1(a)] [83]. Abruptly turning off the shallow trap when the ensemble has reached its maximum size yields a colder cloud [102].

A full expansion of the cloud occurs twice every trap period. Synchronizing the radial (ρ) and vertical (z) oscillations to optimize 3D cooling requires a trap frequency ratio of $\omega_z/\omega_\rho = (n_z + 1/2) / (n_\rho + 1/2)$ for integers n_z and n_ρ . In the absence of gravity, the irrational ratio $\omega_z/\omega_\rho = 2\sqrt{2}$ makes perfect synchronization impossible, but with gravity the ratio is tunable by selecting the appropriate gradient ∇B [84].

5.2.2 Magnetic Lens Oscillations

Figure 5.5(a) shows the evolution of the cloud while in the lens. The center of mass oscillates vertically because the atoms start above the minimum of the shallow trap. To better illustrate the effect of the magnetic lens on the cloud shape, we use a hotter evaporated source with a release temperature of $1.4 \mu\text{K}$ (dominated by chemical potential). We plot the evolution of the cloud widths (from 2D Gaussian fits) in Fig. 5.5(b).¹⁰ The peak of the third vertical expansion ($n_z = 3$) aligns with that of the second radial expansion ($n_\rho = 2$).¹¹

5.2.3 Temperature Results

To precisely tune the lens duration for minimum temperature, we launch the atoms to the top of the tower for a long-time-of-flight velocity measurement. A 162 ms lens duration gives a minimum effective temperature of $(T_\rho, T_z) = (50, 40) \text{ nK}$ and reduced chemical potential. With the same magnetic lensing sequence, but with a deeper evaporation cut, we produce the 1.6 nK source to input to the dipole lens.

¹⁰The cloud shape is in general non-Gaussian due to the anharmonicity of the trap.

¹¹With $n_z = n_\rho = 0$, the shallower trap allows for more expansion but has larger effective anharmonicities.

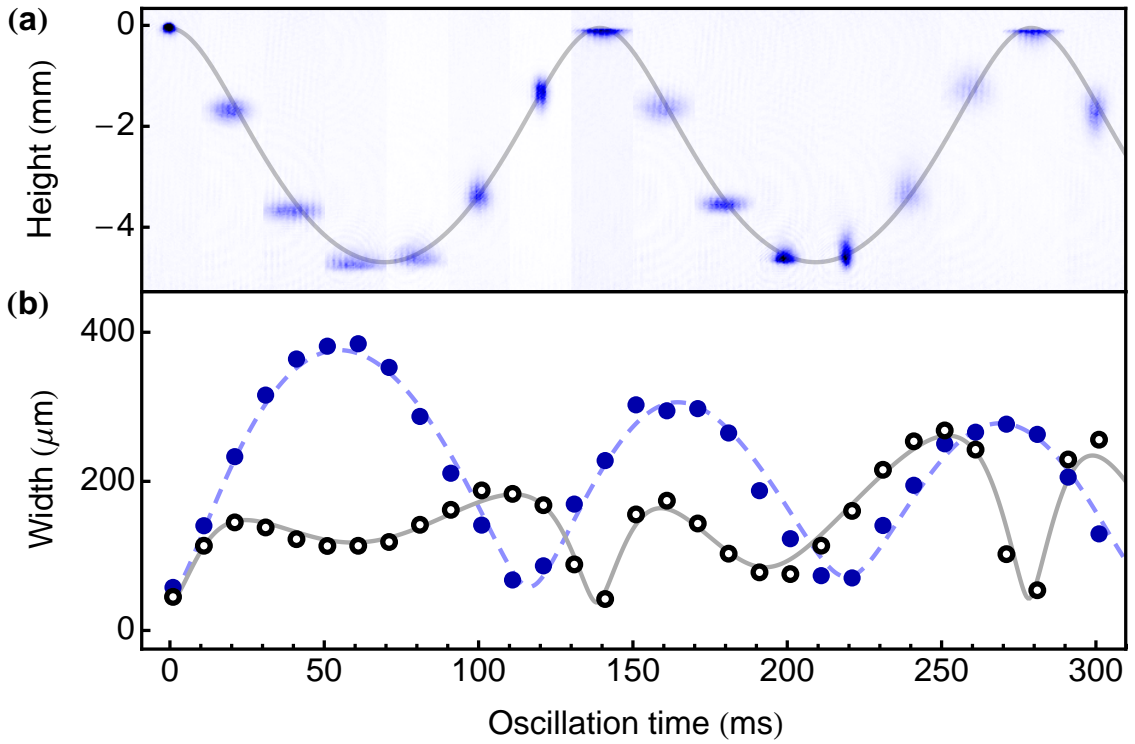


Figure 5.5: Magnetic lensing in the TOP trap. (a) Absorption images of the ensemble oscillating in the trap. (b) Radial (filled blue circles) and vertical (open black circles) RMS cloud widths. The curves, based on numerical solutions for trajectories of non-interacting particles in the exact TOP potential, closely match the cloud behavior. The solid grey curves are simultaneous fits to the center-of-mass trajectory and the vertical width with only seven physically-motivated free parameters. The dashed blue curve results from a 2D Monte Carlo simulation of the atom distribution using the fitted parameters (including $\nabla B = 20.9 \pm 0.1 \text{ G/cm}$, $B_0 = 6.9 \pm 0.3 \text{ G}$) but no free parameters. The initial radial size distribution is scaled from the measured initial cloud widths.

5.2.4 Lattice-Assisted Magnetic Lens Cooling

As an alternative method for 3D lensing in the TOP trap, we have synchronized the turning points by delaying the vertical expansion with an optical lattice.¹² As mentioned above, it is not possible to perfectly synchronize the vertical and radial expansions in a gravity-sagged TOP trap for arbitrary quadrupole gradients ∇B . For example, when we apply $\nabla B = 23 \text{ G/cm}$ the first turning points occur at approximately $(t_\rho, t_z) = (46, 19) \text{ ms}$. There are no coincident points of maximal radial and vertical expansion for many periods. However, by initially holding the atoms in a vertical optical lattice, the vertical expansion is delayed enough for both to reach their first maximum simultaneously. For this delay, we use the same lattice beam that later launches the atoms (Figure 1(a) of the main text).

In the presence of the optical lattice, t_ρ is approximately 5 ms smaller than without the lattice. The lattice holds the atoms closer to the location of the quadrupole field zero, where the radial trapping frequency is higher. In practice, we launch the atoms for a long time-of-flight temperature measurement and adjust the lattice hold time δt_{lat} and total oscillation time in the magnetic trap δt_{mag} for optimal temperature. For $\delta t_{\text{lat}} = 22 \text{ ms}$ and $\delta t_{\text{mag}} = 41 \text{ ms}$, the $1.4 \mu\text{K}$ source is cooled to $(T_\rho, T_z) = (70, 60) \text{ nK}$.

The lattice-assisted magnetic lens oscillations can be seen in Fig. 5.6. The slight radial COM oscillation results from imperfect alignment of the optical lattice. Some atoms are not well-trapped by the optical lattice and can be seen oscillating out of phase with the majority of the atoms.

5.3 Implications and Conclusion

Our dipole lensing results constrain modifications to quantum mechanics at macroscopic scales that predict spontaneous heating of a free gas [49, 55]. The measured cloud size $(\Delta x_i)_{\text{min}}$ constrains the heating rate for ^{87}Rb to $20 \pm 30 \text{ pK/s}$ (see Appendix A and Fig. 1.4).

This dipole lensing technique has the potential to reach even colder temperatures.

¹²Dipole lensing in 3D could be accomplished with crossed optical beams.

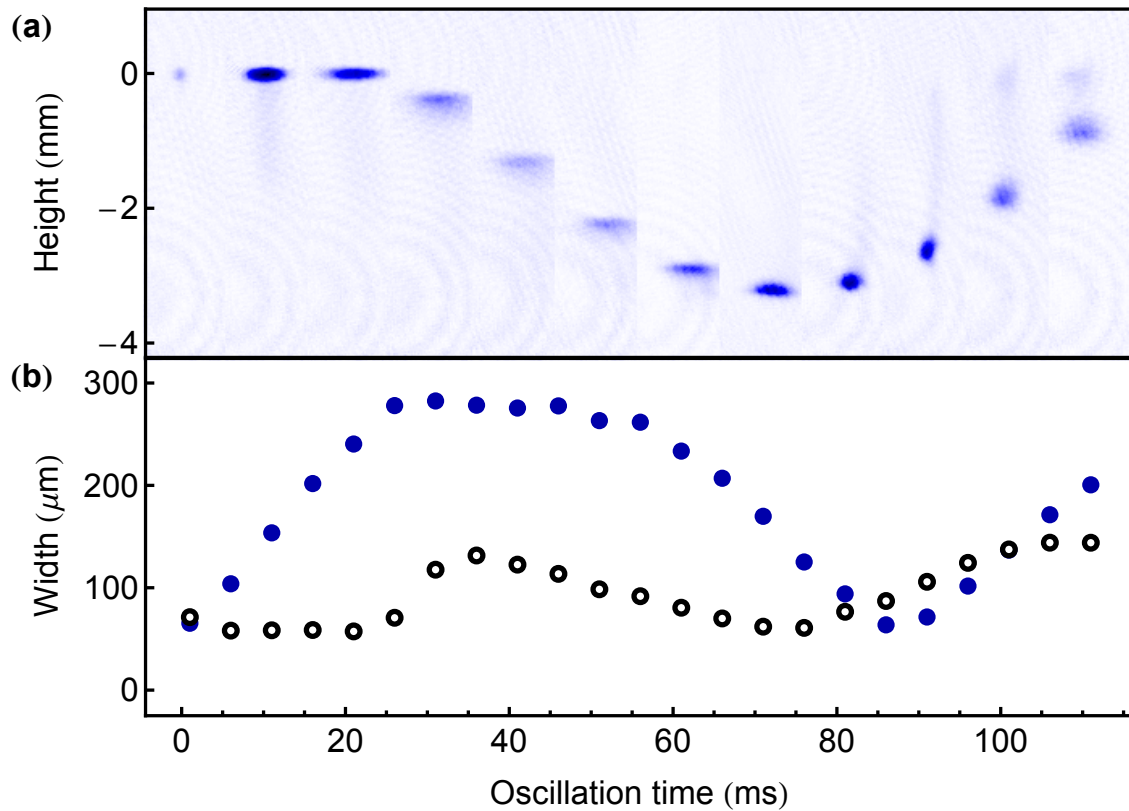


Figure 5.6: Oscillations of the ensemble in the anisotropic TOP trap with an optical lattice. (a) A sequence of absorption images of the cloud after oscillating in the TOP trap. (b) Radial (filled blue circles) and vertical (open black circles) RMS cloud widths as determined by Gaussian fits to the absorption images. The lattice prevents the atoms from falling or expanding vertically for the first 22 ms.

Fundamentally, the diffraction-limited collimation temperature for a wavepacket with size Δx_ℓ at the lens is determined by the minimum velocity width $\hbar/(2m\Delta x_\ell)$ allowed by the uncertainty principle (~ 10 fK for the $\Delta x_\ell \approx 400$ μm clouds used in this work). Reaching the diffraction limit requires an uncertainty-principle-limited source. After the magnetic lens and lattice launch, the atom cloud exceeds this limit by a factor of $m\Delta v_o\Delta x_o/(\hbar/2) \approx 60$ or less¹³ (possible heating during the lattice launch may contribute substantially to this excess). A larger lensing beam could reduce Gaussian aberrations, and the beam could be more strongly spatially filtered, perhaps by an optical cavity or a longer propagation distance. The cooling performance could be further enhanced by operating in space, allowing for longer expansion times.

¹³Again, an initially correlated ensemble corresponds to a virtual source with an effective initial size smaller than Δx_o .

Chapter 6

Large Momentum Transfer

As discussed in Section 1.2, the sensitivity of the interferometer can be increased using large momentum transfer (LMT) atom optics. Specifically, by switching from $2\hbar k$ atom optics to $2N\hbar k$ atom optics, the phase shift from a uniform gravitational field is increased from $2kgT^2$ to $2NkgT^2$. This yields an N -fold enhancement in sensitivity, which would, for instance, dramatically reduce the integration time needed to reach the 10^{-15} level for an equivalence principle test (Table 1.1). Also, the maximum wavepacket separation increases by the same factor, to

$$\Delta z = \frac{2N\hbar k}{m} T. \quad (6.1)$$

Thus, the macroscopicity of the superposition state is increased (Section 1.3). As I will show shortly, we have demonstrated LMT atom interferometry up to $12\hbar k$, with a maximum wavepacket separation of 8.2 cm.

LMT interferometry requires splitting the interferometer arms by more than two photon recoils. That is, beam splitters and mirrors are needed that impart more than $2\hbar k$ of momentum. Several such methods have been developed, including sequential Raman transitions [125], multiphoton Bragg transitions [17, 126, 127], and optical lattice manipulations [95, 98]. An interferometer has been demonstrated with 18% contrast at $102\hbar k$ in a small-scale system [17]. Combining LMT with long interrogation time in the 10 m tower is an ongoing research goal in our lab.

6.1 Sequential Raman LMT

Here I focus on sequential Raman LMT atom optics. The fundamental technique is demonstrated in Fig. 6.1, in a frame falling with gravity. For the initial LMT beamsplitter, consider an atomic wavepacket in state $|1\rangle$. A two-photon Raman $\frac{\pi}{2}$ pulse with \mathbf{k}_1 upwards and \mathbf{k}_2 downwards gives part of the atom a momentum kick $\hbar\mathbf{k}_{\text{eff},2\gamma} = \hbar(\mathbf{k}_1 - \mathbf{k}_2)$ upwards, while the untransferred part of the atom receives no momentum kick (as in Section 1.1.1). The two halves of the wavepacket are then separated in momentum by $2\hbar k$. The necessary frequency difference between the two lasers was given in Eq. 2.2, which I repeat here:

$$\omega_1 - \omega_2 = \frac{\hbar\mathbf{k}_{\text{eff},2\gamma}^2}{2m} + \mathbf{k}_{\text{eff},2\gamma} \cdot \mathbf{v} + (\omega_{|2\rangle}^a - \omega_{|1\rangle}^a), \quad (6.2)$$

where \mathbf{v} is the velocity before the pulse.

To increase the momentum splitting, a π pulse can be applied to advance the momentum of only the upper arm by an additional $2\hbar k$. With sufficiently low Rabi frequency, the width of the two-photon Raman transition is less than the recoil velocity, and the LMT pulse affects only one arm of the interferometer.¹ To kick the upper arm (in state $|2\rangle$) further up, it is necessary to switch the roles of the Raman beams, so that the atom first absorbs an upward-going \mathbf{k}'_2 photon, and then stimulated-emits a downward going \mathbf{k}'_1 photon [Fig. 1.1(c)]. The momentum kick is then $\hbar\mathbf{k}'_{\text{eff},2\gamma} = \hbar(\mathbf{k}'_2 - \mathbf{k}'_1) \approx \hbar(\mathbf{k}_1 - \mathbf{k}_2) = \hbar\mathbf{k}_{\text{eff},2\gamma}$ upwards, in the same direction as the initial momentum splitting. By analogy with Eq. 6.2, the resonant frequency difference between the lasers is now

$$\omega'_1 - \omega'_2 = -\frac{\hbar\mathbf{k}'_{\text{eff},2\gamma}^2}{2m} - \mathbf{k}'_{\text{eff},2\gamma} \cdot \mathbf{v}' + (\omega_{|2\rangle}^a - \omega_{|1\rangle}^a), \quad (6.3)$$

where \mathbf{v}' accounts for the momentum kick from the preceding pulse. For our retroreflection configuration, it is convenient to leave the $(\omega_{|2\rangle}^a - \omega_{|1\rangle}^a) \approx 6.8$ GHz shift on the same laser and switch to the other polarization pair,² accounting for the Doppler and

¹With a higher Rabi frequency, it is possible to drive the interferometer arms in opposite directions, but this is not sustainable for large N .

²As drawn in Fig. 2.7(a), \mathbf{k}'_1 and \mathbf{k}'_2 correspond to the dashed, σ^- polarization components.

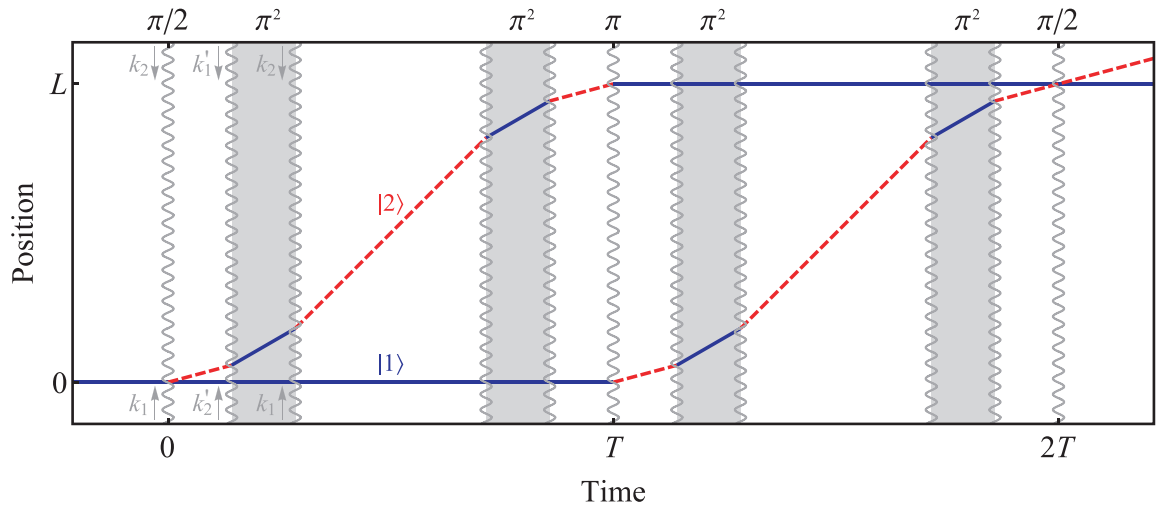


Figure 6.1: A $6\hbar k$ sequential Raman Mach-Zehnder light-pulse atom interferometer ($N = 3$). The wavevectors are labeled only for the first LMT beamsplitter; a similar alternating propagation reversal scheme is used for the other pulses. Additional π pulses can be added to the LMT zones (gray bands) to further increase the momentum separation (for $N > 3$). (In the LMT zones, one arm of the interferometer is not affected by the pulses because of the Doppler shift.) For comparison, see Fig. 1.1(d), but note that the axes are not to scale (the opening angle corresponding to $2\hbar k$ is smaller here).

recoil terms with AOMs.³ The momentum splitting can be increased further with a sequence of π pulses alternating between the unprimed (Eq. 6.2) and primed (Eq. 6.3) frequencies, accounting for the changing Doppler shift.

A $2N\hbar k$ LMT beamsplitter can therefore be composed from a conventional $2\hbar k \frac{\pi}{2}$ pulse followed by $(N - 1)$ LMT π pulses applied to only one arm of the interferometer. Likewise, an LMT mirror can be achieved with $(N - 1)$ π pulses on one arm, followed by a conventional mirror pulse acting on both arms, followed by $(N - 1)$ π pulses on the other arm. The interferometer is closed with a second LMT beamsplitter, an inversion of the first. The full $2N\hbar k$ LMT Mach-Zehnder pulse sequence is then

$$\left(\frac{\pi}{2} - \pi_{\text{upper}, \uparrow}^{N-1}\right) - T - \left(\pi_{\text{upper}, \downarrow}^{N-1} - \pi - \pi_{\text{lower}, \uparrow}^{N-1}\right) - T - \left(\pi_{\text{lower}, \downarrow}^{N-1} - \frac{\pi}{2}\right) \quad (6.4)$$

where for example $\pi_{\text{upper}, \uparrow}^{N-1}$ corresponds to $N - 1$ sequential Raman π pulses, each used to kick the upper arm upwards.⁴ A full $6\hbar k$ interferometer of this type is shown in Fig. 6.1.

6.2 $12\hbar k$ Interferometer with 8.2 cm Wavepacket Separation

A $2N\hbar k$ interferometer requires a total of $3 + 4 \times (N - 1)$ pulses (with a total duration of $(4N - 2) \times \delta t_\pi$). Compared to a $2\hbar k$ interferometer, the light is incident on the atoms $(2N - 1)$ times longer. This places more stringent demands on the Raman lasers, both because of increased spontaneous emission (Eq. 2.5) and the aggregation of imperfect pulse transfer over many repeated pulses. The latter contributes to our use of the coldest possible atom source for LMT interferometry [corresponding to the ~ 1 nK source of Fig. 3.3(a) and Section 5.2.3] to keep the cloud well localized at the time of the final beamsplitter for uniform intensity and Rabi frequency.

³We occasionally adjust the 6.8 GHz modulation slightly between pulses to reduce the bandwidth requirements on the AOMs.

⁴Other similar pulse sequences are possible, with the only constraint being that prior to the final $\pi/2$ pulse, the arms should overlap spatially and differ in momentum by $2\hbar k$. A simple symmetric version is presented in Eq. 6.4 and Fig. 6.1.

The increased spontaneous emission losses can be mitigated by increasing the single-photon detuning Δ (see Eq. 2.5). This in turn requires increasing the laser intensity I to maintain sufficient Rabi frequency Ω_{eff} . We therefore use the second-generation, high-power atom-optics laser system (Section 2.2.3 and Fig. 2.15) for LMT interferometry. Specifically, we operate with a single-photon detuning of $\Delta \sim 3$ GHz, total single beam powers of $P_0 \sim 3$ W, $1/e^2$ radial waists of $\omega_0 = 2$ cm, and AC Stark shifts compensated absolutely.⁵ Typical Rabi frequencies for this system correspond to $\delta t_\pi = 15$ μ s. The atom source uses evaporation in the TOP trap (Section 2.3.4), magnetic lensing to 1.6 nK (Section 5.2.3), and our typical full-tower lattice launch (Section 2.4). With this system, we have performed $2T = 2.3$ s atom LMT interferometry with momentum splittings of up to $12\hbar k$, as shown in Fig. 6.2(a). The contrast at $12\hbar k$ is $\sim 10\%$,⁶ and the peak wavepacket separation at the top of the interferometer is 8.2 cm. This large superposition state constrains the space of possible macroscopic modifications of quantum mechanics (Fig. 1.4).⁷

6.3 Sources of Contrast Loss and Ongoing Work

While Fig. 6.2(a) shows LMT interferometry with momentum splittings of up to $12\hbar k$, the contrast decays substantially with increasing LMT order. LMT interferometry beyond $12\hbar k$ proved difficult with this system. Several factors likely contribute to this loss of contrast, including spontaneous emission (Section 6.3.1), imperfect transfer during the LMT pulses (Section 6.3.2), and uncontrolled inhomogeneous interferometer phase shifts (Section 6.3.3).

⁵We measure single-beam relative compensation. By symmetry of the modulation scheme, this roughly corresponds to absolute compensation. See Section 2.2.3 and [29].

⁶With the upgraded $\Delta \sim 3$ GHz laser system, the contrast at $2\hbar k$ is $\sim 90\%$, a 10% improvement over Fig. 3.3(c).

⁷Accounting for expected contrast loss would yield improved limits for the “unexplained” contrast loss. This is the relevant figure of merit for tests of macroscopicity (Fig. 1.4). For instance, at $12\hbar k$, the expected contrast loss due to spontaneous emission is 30% [29], so $f_{12\hbar k} = \frac{0.10}{1-0.30} = 0.15$ would yield a slightly less conservative bound in Fig. 1.4. Accounting for other “mundane” contrast loss mechanisms would further improve the constraint on macroscopic modifications of quantum mechanics.

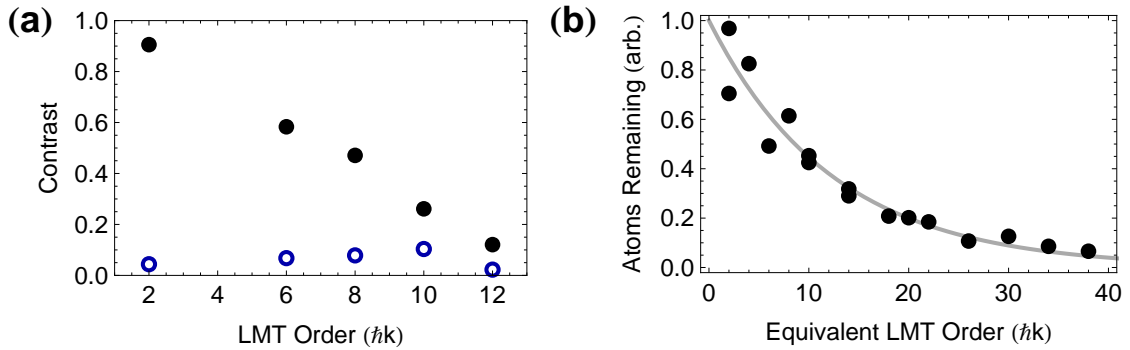


Figure 6.2: (a) Large momentum transfer (LMT) atom interferometry. (a) Interferometer contrast vs. LMT order. The black (closed) circles are the interferometer data, and the contrast has been measured as in Fig. 3.3. The blue (open) circles correspond to control measurements in which the second $\frac{\pi}{2}$ pulse has been delayed by $600 \mu\text{s}$ ($1800 \mu\text{s}$ for $2\hbar k$). (This creates an unresolved high-frequency vertical spatial fringe (Section 4.6), which yields no interferometer contrast - the ports should have roughly equal atom number after every shot.) (b) Normalized atom loss due to spontaneous emission. A full interferometer sequence was run with a two-photon Raman detuning of 1 MHz to suppress population transfer during the atom optics pulses. Atoms undergoing spontaneous emission during the first beamsplitter or the mirror (including the associated LMT zones) are removed from the cloud by the time of imaging. Atoms undergoing spontaneous emission during the final beamsplitter are detected as a diffuse background. As a result, we determine the unscattered atom number by cropping closely and fitting a Gaussian to the main cloud to remove the background. The gray curve is an exponential fit to the data, with a $1/e$ decay “time” of $12.4\hbar k$. See also [29].

6.3.1 Spontaneous Emission

Fig. 6.2(b) shows that the initial implementation of the high-power laser system with $\Delta \sim 3$ GHz suffers from excessive spontaneous emission. Only 37% of the atoms have not undergone a spontaneous emission event after the full $12\hbar k$ pulse sequence. Atoms that undergo spontaneous emission are given a velocity kick of $\sim v_r = \hbar k/m = 5.9$ mm/s. Atoms lost to spontaneous emission during the first beamsplitter or the mirror (including the associated LMT zones) have $\gtrsim 1$ s to drift with this velocity, and are removed from the cloud. The loss of these atoms therefore corresponds to a decreased atom number \mathcal{N} .⁸ Atoms lost to spontaneous emission during the final beamsplitter only have ~ 100 ms to drift before imaging, and form a diffuse background. These atoms contribute to a loss of contrast f . In either case, spontaneous emission reduces the effective atom flux $n = f\mathcal{N}q\tau^{-1}$ (Section 1.2), which in turn reduces the sensitivity of a phase measurement.

While spontaneous emission doesn't explain all of the loss of contrast in Fig. 6.2(a) [29], it is clear from Fig. 6.2(b) that interferometers with $100\hbar k$ or more are not possible with $\Delta \sim 3$ GHz. It is therefore necessary to increase the single-photon detuning Δ to reduce spontaneous emission (Section 2.2.3). Since the ground state hyperfine splitting is 6.8 GHz, this requires driving the Raman transition with both lasers red of both transitions or both blue of both transitions ($\omega_1, \omega_2 < \omega_{2e}$ or $\omega_{1e} < \omega_1, \omega_2$, see Section 2.2.3). To maintain single-beam absolute Stark compensation, we center the RIO carrier frequency between the transitions, and modulate the two paths (Fig. 2.15) at Δ_{ss} and $\Delta_{ss} + 6.8$ GHz respectively to drive the transition with sidebands. While it is necessary to leave some power in the carriers for Stark shift compensation, spontaneous emission is again reduced for increased Δ_{ss} [29]. Initial work with $\Delta_{ss} \sim 30$ GHz has shown sufficiently reduced spontaneous emission, but with excessively low Rabi frequency ($\delta t_\pi \gtrsim 100$ μ s). Ongoing work therefore explores intermediate detunings with 3 GHz $< \Delta < 30$ GHz.

⁸For low atom number, the signal-to-noise ratio at detection is reduced. Statistical variations could then yield a measured variation in the relative atom number at the output ports. This likely explains the increase in the “contrast” of the control points in Fig. 6.2(a) with increasing LMT order. For LMT order $\gtrsim 12\hbar k$, the signal-to-noise is sufficiently low that this effect could explain much of the measured contrast.

6.3.2 Rabi Frequency and Detuning Variations

Any spatial variation in the Rabi frequency or detuning yields a dephasing between atoms in different parts of the cloud during the atom optics pulses. The time δt_π will not be uniform over the cloud. This reduces the overall pulse efficiency, such that only a fraction of the atoms are transferred, reducing the ultimate interferometer contrast. This is especially pernicious in sequential Raman LMT interferometry, in which even a small loss to each unintended exit port⁹ can yield large aggregate losses.

For both $\Delta \sim 3$ GHz and $\Delta \sim 30$ GHz, the transfer efficiency of a π pulse can be as low as $\sim 90\%$ in our system (especially for the final beamsplitter, where the atom cloud has expanded to its maximal size). This can be improved with composite pulse sequences, which broaden the effective Raman resonance to accommodate inhomogeneous Rabi frequencies and/or detunings [128]. The transfer efficiency could also be improved by incorporating atom lensing to reduce the cloud size at the atom optics pulses (Section 5.1.8). Finally, we could switch from sequential Raman atom optics to sequential multi-photon Bragg atom optics [17].¹⁰ This approach requires fewer pulses for a given momentum splitting, reducing losses from both spontaneous emission and pulse inefficiencies.¹¹ Ongoing research in our lab explores all of these possibilities.

6.3.3 Inhomogeneous Interferometer Phase

The enhanced sensitivity of LMT interferometry increases the potential for contrast loss due to uncontrolled inhomogeneous interferometer phase shifts. As discussed in Chapters 3 and 4, these position- or velocity-dependent phases create a spatially-varying fringe pattern at each output port. The increased LMT sensitivity would yield fringes of higher spatial frequency. This could reduce our ability to resolve the spatial fringe, and we would report a reduced effective contrast. It might therefore be necessary to improve the resolution of the imaging system (Fig. 2.21), or to employ a

⁹These additional exit ports correspond to continuations of all of the line segments in Fig. 6.1, not shown.

¹⁰We are also exploring lattice manipulations [98].

¹¹As an added benefit, the reduced frequency difference between the two Bragg paths could yield reduced phase noise (Fig. 2.15). This would improve the effectiveness of composite pulse sequences.

novel imaging approach that facilitates single-shot 3D imaging of atomic clouds [129].

Potential sources of inhomogeneous dephasing have been discussed throughout this thesis, and include rotations, gravity gradients, magnetic field gradients, and wavefront errors. Their effects may need to be further reduced or studied not only as systematics for the equivalence principle measurement, but also to enable high-contrast, long-baseline LMT interferometry.

Chapter 7

Conclusion

This thesis shows the substantial progress of the Stanford 10 m atom interferometer in the last half-decade. We have demonstrated record-duration $2T = 2.3$ s atom interferometry with a nearly shot-noise-limited sensitivity of $6.7 \times 10^{-12}g$ per shot. Combined with ongoing work with LMT interferometry, this sensitivity is a giant leap towards an atomic test of the equivalence principle at the $10^{-15}g$ level.

We have also demonstrated techniques to control and mitigate systematic effects, especially those from magnetic fields and rotations. These techniques include the development of both advanced hardware (the long-aspect-ratio magnetic shield and the rotation compensation system) and new methods to read out the interferometer phase (PSR and PSI). All of these advances will benefit not only the equivalence principle test, but also future long-baseline atom interferometric precision tests of fundamental physics, possibly including gravitational wave detection.

Finally, we have cooled ^{87}Rb atoms to an unprecedented effective temperature of 50_{-30}^{+50} pK and achieved a record atomic wavepacket separation of 8.2 cm. These results provide some of the best constraints to date on possible modifications to quantum mechanics in the macroscopic regime.

Ongoing and Future Work

Work is ongoing to increase the LMT momentum splitting in the 10 m tower. Potential improvements to meet this goal have been outlined in Sections 6.3.2 and 6.3.3. It

should be possible to combine $100\hbar k$ LMT atom optics with $2T = 2.3$ s interrogation times (both already demonstrated) to achieve high-contrast atom interferometry with a wavepacket separation of 1 m. Further improvements might even enable the creation of superposition states at the full 10 m scale of the tower.

Another major avenue of continued research is the addition of the second isotope, ^{85}Rb , to enable the dual species test of the equivalence principle. The manipulation, cooling, and interferometry of neutral atoms is generally a sequential process, both for a single experimental shot and for experimental progress in the lab. Each step must work (at least somewhat) before the next can be attempted. Progress with ^{85}Rb will therefore likely follow a similar roadmap to ^{87}Rb . The ^{85}Rb atoms must be laser-cooled, evaporated, lensed, state-prepped, launched, interfered, and detected. Evaporation is harder with ^{85}Rb in general, and many of these steps will be more challenging because of the need to achieve simultaneous kinematic overlap between both isotopes. Nevertheless, much experimental and theoretical progress has already been made [20, 29], and most of the necessary hardware is in place. Combined with the EP team’s experience with ^{87}Rb in the 10 m apparatus, this should make it possible to incorporate ^{85}Rb fairly quickly.

Further in the future, the 10 m apparatus could be adapted to a variety of other applications. These have been discussed throughout this thesis, and include making a fountain clock, measuring \hbar/m , measuring G , testing atom and neutron neutrality, measuring the gravitational Aharonov-Bohm effect, testing GR in the lab, and making a prototype gravitational wave detector.¹

These varied scientific applications, combined with the growth of companies developing cold atom sensors (AOSense, μ QuanS, ColdQuanta, etc.), highlight atom interferometry’s potential as a disruptive technology that could see far-ranging use in the future. As the field continues to mature, the question isn’t why we should use atom interferometry for these applications, but rather, “why would we *not* use atom interferometry?”

¹Many of these experiments require only minor hardware modifications to our current apparatus.

Appendix A

Spontaneous Heating Rate Limit

The dipole lensing results in Chapter 5 constrain possible spontaneous heating rates for a free gas of Rb atoms. In particular, many proposed classicalizing modifications to quantum mechanics predict such fundamental heating [49,55]. Our results therefore restrict the parameter space of these theories (see also Section 1.3). In the following sections, we first outline some similarities between a classical stochastic heating model and the heating that arises from the classicalizing modification to quantum mechanics presented in [55]. We then analyze the effect that this heating would have on the atom refocusing sequence and find that the refocusing data constrain the heating rate for ^{87}Rb to 20 ± 30 pK/s.

A.1 Heating from a Classicalizing Modification to Quantum Mechanics

In [55] and [54], the authors present a general classicalizing modification to quantum mechanics and show that it leads to fundamental heating. We summarize the relevant results here to motivate the form of the heating rate that we analyze in subsequent sections. A linear modification of the quantum Liouville equation is considered, such

that

$$\frac{\partial \rho}{\partial t} = -\frac{i}{\hbar} [H, \rho] + \mathcal{L}\rho, \quad (\text{A.1})$$

where ρ is the density matrix and \mathcal{L} is a Lindblad operator corresponding to the classicalizing modification. This causes off-diagonal terms in the density matrix to decay over time, such that the state evolves into a classical mixture. For the form of \mathcal{L} considered in [55], interference effects beyond a critical length scale \hbar/σ_q or a critical momentum scale \hbar/σ_s decay in a characteristic time τ .

The time evolution of the expectation value of an observable \hat{A} under the classicalizing modification is [54]

$$\partial_t \langle \hat{A} \rangle = \frac{i}{\hbar} \langle [\hat{H}, \hat{A}] \rangle + \langle \mathcal{L}^\dagger \hat{A} \rangle. \quad (\text{A.2})$$

This corresponds to the Ehrenfest theorem, but with an additional term. For the form of \mathcal{L} considered in [55], the additional term affects the time evolution of expectation values of the position and momentum operators only at second order and above. Specifically, for the free space evolution and harmonic lens of the delta-kick cooling sequence, the time evolution of the relevant operators is [54]

$$\partial_t \langle \hat{\mathbf{r}} \rangle = \frac{\langle \hat{\mathbf{p}} \rangle}{m} \quad (\text{A.3})$$

$$\partial_t \langle \hat{\mathbf{p}} \rangle = -m\omega^2 \langle \hat{\mathbf{r}} \rangle \quad (\text{A.4})$$

$$\partial_t \langle \hat{\mathbf{r}}^2 \rangle = \frac{1}{m} (\langle \hat{\mathbf{p}} \cdot \hat{\mathbf{r}} + \hat{\mathbf{r}} \cdot \hat{\mathbf{p}} \rangle) + \frac{\sigma_s^2}{\tau} \quad (\text{A.5})$$

$$\partial_t \langle \hat{\mathbf{p}} \cdot \hat{\mathbf{r}} \rangle = \partial_t \langle \hat{\mathbf{r}} \cdot \hat{\mathbf{p}} \rangle = \frac{1}{m} \langle \hat{\mathbf{p}}^2 \rangle - m\omega^2 \langle \hat{\mathbf{r}}^2 \rangle \quad (\text{A.6})$$

$$\partial_t \langle \hat{\mathbf{p}}^2 \rangle = -m\omega^2 \langle \hat{\mathbf{p}} \cdot \hat{\mathbf{r}} + \hat{\mathbf{r}} \cdot \hat{\mathbf{p}} \rangle + \frac{\sigma_q^2}{\tau} \quad (\text{A.7})$$

The terms with ω are nonzero only during the lens application time. The classicalizing modification causes deviation from the original equations of motion by introducing an additional diffusion in both momentum and position space, characterized by a constant heating rate $\frac{\sigma_q^2}{2m\tau}$ ($\frac{J}{s}$) and a spreading rate $\frac{\sigma_s^2}{\tau}$ ($\frac{m^2}{s}$).

A.2 Analogous Classical Model: Fokker-Planck Equation with a Stochastic Force

In parallel to the results of Sec. A.1, the classical Fokker-Planck model produces unmodified equations of motion for first moments of a phase space distribution, and an additional constant rate of increase in second moments. This model describes the altered evolution of an otherwise deterministic system due to stochastic white noise forces.

We work in terms of the one-dimensional variables x and v for a single particle's parameter space. Under the Fokker-Planck model, a set of generalized stochastic forces η_x and η_v continuously alter deterministic phase space trajectories via

$$\frac{d}{dt} \begin{bmatrix} x(t) \\ v(t) \end{bmatrix} = \begin{bmatrix} v(t) \\ -\frac{1}{m} \partial_x V \end{bmatrix} + \begin{bmatrix} \eta_x(t) \\ \eta_v(t) \end{bmatrix} \quad (\text{A.8})$$

The curly bracket notation $\{g(\eta(t))\}$ will be used to define the noise-averaged value of a stochastic variable, where “stochastic variable” is defined as the variable $\eta(t)$ itself or any function g which depends on the stochastic term. The angle bracket notation retains its meaning as an expectation value over the phase space distribution.

As Gaussian white noise terms, the forces η have the following properties:

1. The distributions $\eta_x(t)$ and $\eta_v(t)$ at a given time t each have a mean value of zero: $\{\eta_v(t)\} = \{\eta_x(t)\} = 0$.
2. The distribution η_v is delta-correlated in time: $\{\eta_v(t_1)\eta_v(t_2)\} = D_v \delta(t_2 - t_1)$.
3. The distribution η_x is also delta-correlated: $\{\eta_x(t_1)\eta_x(t_2)\} = D_x \delta(t_2 - t_1)$.
4. The separate distributions are uncorrelated: $\{\eta_v(t_1)\eta_x(t_2)\} = 0$.

Here D_x and D_v are constants characterizing the strengths of the stochastic forces. Due to the stochastic forces, the first moments of a noise-averaged trajectory evolve according to the original equations of motion given by Hamilton's equations, and a modifying term is added to the time evolution of the second moments. Taking first the

phase-space ensemble average and next the noise average of Eq. A.8 for a harmonic potential, and applying the noise-average properties of η :

$$\{\partial_t \langle x \rangle\} = \{\langle v \rangle\} \quad (\text{A.9})$$

$$\{\partial_t \langle v \rangle\} = -\omega^2 \{\langle x \rangle\} \quad (\text{A.10})$$

$$\{\partial_t \langle x^2 \rangle\} = 2 \{\langle x \cdot v \rangle\} + D_x \quad (\text{A.11})$$

$$\{\partial_t \langle x \cdot v \rangle\} = \{\langle v^2 \rangle\} - \omega^2 \{\langle x^2 \rangle\} \quad (\text{A.12})$$

$$\{\partial_t \langle v^2 \rangle\} = -2\omega^2 \{\langle x \cdot v \rangle\} + D_v \quad (\text{A.13})$$

Again, the terms with ω are only nonzero during the lens application time. Eqs. A.3 through A.7 (for the effect of the Lindblad operator), and Eqs. A.9 through A.13 (for the classical Fokker-Planck model model of diffusion) therefore form an analogous set of differential equations for moments up to second order of a distribution. The connection is made concrete by setting $D_x = \frac{\sigma_s^2}{\tau}$, and $D_v = \frac{\sigma_q^2}{m^2 \tau}$.

An expression can now be derived for final width of the cloud in terms of D_v and D_x by considering evolution of classical trajectories. Given a particular initial value of both Δx_o and Δv_o , we can compare the modeled minimized final width $(\Delta x_i)_{\min}$ under a perfect harmonic lens to the measured value. If the error between the two values is ascribed fully to the modifications introduced by stochastic diffusive terms, then a maximum heating rate is set.

A.3 Stochastic Modifications of the Trajectories

Terms that couple to η_v and η_x will be expressed in terms of their noise averages. The total change in the trajectory from its deterministic $(x(t), v(t))$ at a time t due to η_v is labeled $(\delta x_{\eta_v}(t), \delta v_{\eta_v}(t))$, and the change due to η_x is $\delta x_{\eta_x}(t)$. Due to the form of Hamilton's equations of motion, η_x does not directly couple to the variable $v(t)$. The

changes are given in integral form by

$$\delta v_{\eta_v}(t_1, t_2) = \int_{t_1}^{t_2} \eta_v(t') dt' \quad (\text{A.14})$$

$$\delta x_{\eta_v}(t_1, t_2) = \int_{t_1}^{t_2} \int_{t_1}^{t'} \eta_v(t'') dt'' dt' \quad (\text{A.15})$$

$$\delta x_{\eta_x}(t_1, t_2) = \int_{t_1}^{t_2} \eta_x(t') dt' \quad (\text{A.16})$$

Using these definitions, the results of Table A.1 follow from the fact that the stochastic force is independent of phase space trajectory. The results of Table A.2 can be shown from repeated integration of Eq. A.8. Table A.2 lists results for fully overlapping time intervals; for nonoverlapping time intervals, the noise-average product of all stochastic terms in the table is zero.

Table A.1: Stochastic Variable Correlations with Initial Distribution

$\{\langle \delta x_{\eta_{v,x}}(t_1, t_2)x_o \rangle\} = 0$	$\{\langle \delta v_{\eta_v}(t_1, t_2)x_o \rangle\} = 0$
$\{\langle \delta x_{\eta_{v,x}}(t_1, t_2)v_o \rangle\} = 0$	$\{\langle \delta v_{\eta_v}(t_1, t_2)v_o \rangle\} = 0$

Table A.2: Noise Averages of Stochastic Variable Correlations

$\{\langle \delta v_{\eta_v}(t_1, t_2)\delta v_{\eta_v}(t_1, t_2) \rangle\} = D_v(t_2 - t_1)$	$\{\langle \delta x_{\eta_x}(t_1, t_2)\delta x_{\eta_x}(t_1, t_2) \rangle\} = D_x(t_2 - t_1)$
$\{\langle \delta x_{\eta_v}(t_1, t_2)\delta x_{\eta_v}(t_1, t_2) \rangle\} = \frac{1}{3}D_v(t_2 - t_1)^3$	$\{\langle \delta v_{\eta_v}(t_1, t_2)\delta x_{\eta_v}(t_1, t_2) \rangle\} = \frac{1}{2}D_v(t_2 - t_1)^2$

A.4 Delta-Kick Sequence with Stochastic Modification

In the following sections, we assume $\langle v_o x_o \rangle = 0$ and that the lens provides a perfect harmonic potential.

A.4.1 Object to Lens

Directly before the lens (ℓ^-) and immediately after (ℓ^+), the noise average position and velocity of a trajectory in phase space are

$$x_{\ell^-} = x_{\ell^+} = x_o + v_o t_o + \delta x_{\eta_v}(0, t_o) + \delta x_{\eta_x}(0, t_o) \quad (\text{A.17})$$

$$v_{\ell^-} = v_o + \delta v_{\eta_v}(0, t_o) \quad (\text{A.18})$$

$$v_{\ell^+} = v_o + \delta v_{\eta_v}(0, t_o) - \omega^2 \delta t x_{\ell^-} \quad (\text{A.19})$$

It is assumed that the cooling rate during the lens application is much larger than the heating rate due to diffusion, $\langle v_{\ell^+}^2 \rangle - \langle v_{\ell^-}^2 \rangle \gg D_v \delta t$, so that the effect of the stochastic modification can be neglected during the time that the atom spends in the harmonic potential. The noise-averaged and ensemble-averaged position and velocity variance after the lens become

$$\{\langle \Delta x_{\ell^+}^2 \rangle\} = \Delta x_o^2 + \Delta v_o^2 t_o^2 + \frac{D_v t_o^3}{3} + D_x t_o \quad (\text{A.20})$$

$$\begin{aligned} \{\langle \Delta v_{\ell^+}^2 \rangle\} &= \Delta v_o^2 + D_v t_o - 2\omega^2 \delta t \left(\Delta v_o^2 t_o + \frac{D_v t_o^2}{2} \right) \\ &\quad + \omega^4 \delta t^2 \left(\Delta v_o^2 t_o^2 + \Delta x_o^2 + \frac{D_v t_o^3}{3} + D_x t_o \right) \end{aligned} \quad (\text{A.21})$$

The results from Table A.1 and Table A.2 have been applied to eliminate or reduce relevant terms.

A.4.2 Lens to Image

The single-particle position and velocities at the image are

$$v_i = v_{\ell^+} + \delta v_{\eta_v}(t_o, t_o + t_i) \quad (\text{A.22})$$

$$x_i = t_i v_{\ell^+} + x_{\ell^+} + \delta x_{\eta_v}(t_o, t_o + t_i) + \delta x_{\eta_x}(t_o, t_o + t_i) \quad (\text{A.23})$$

After neglecting terms with an average value of zero, the noise-averaged, ensemble-averaged position variance at the image takes the form

$$\{\langle \Delta x_i^2 \rangle\} = t_i^2 \{\langle \Delta v_{\ell+}^2 \rangle\} + \{\langle \Delta x_{\ell+}^2 \rangle\} + 2t_i \{\langle \Delta x_{\ell+} \Delta v_{\ell+} \rangle\} + \frac{D_v t_i^3}{3} + D_x t_i \quad (\text{A.24})$$

Next, the expressions from Eqs. A.20 and A.21 are substituted into A.24. The cross-correlation term between position and velocity directly after the lens takes the form

$$\{\langle \Delta x_{\ell+} \Delta v_{\ell+} \rangle\} = \Delta v_o^2 t_o + \frac{D_v t_o^2}{2} - \omega^2 \delta t \left(\Delta v_o^2 t_o^2 + \Delta x_o^2 + \frac{D_v t_o^3}{3} + D_x t_o \right). \quad (\text{A.25})$$

A.4.3 Constraining the Heating Rate with Refocusing Data

Next, we assume that in an experiment, the lens application time will be chosen to minimize the final cloud width. This time is found symbolically as the solution to

$$\frac{\partial \{\langle \Delta x_i^2 \rangle\}}{\partial (\delta t)} = 0. \quad (\text{A.26})$$

In an ideal deterministic case with an uncorrelated position-velocity distribution, the cloud size at the lens is $\Delta x_{\ell}^2 = \Delta x_o^2 + t_o^2 \Delta v_o^2$, and the minimum cloud width after refocusing is given by

$$(\Delta x_i)_{\min} = \frac{t_i^2 \Delta v_o^2 \Delta x_o^2}{\Delta x_{\ell}^2} \quad (\text{A.27})$$

The minimized cloud size at the image plane using the expression for δt from Eqn. A.26 becomes

$$(\Delta x_i)_{\min} = \frac{t_i^2 \Delta v_o^2 \Delta x_o^2 + a D_x + b D_v + c D_x D_v + d D_x^2 + e D_v^2}{\Delta x_{\ell}^2 + \frac{D_v t_o^3}{3} + D_x t_o} \quad (\text{A.28})$$

where

$$\begin{aligned} a &= t_i \Delta x_\ell^2 \left(1 + \frac{t_i}{t_o} (1 - \gamma^2) \right) \\ b &= \frac{1}{3} t_i^2 t_o \Delta x_\ell^2 \left(1 + \frac{t_i}{t_o} + 2\gamma^2 \right) \\ c &= \frac{1}{3} t_i t_o (t_i^2 + 3t_i t_o + t_o^2) \\ d &= t_i t_o \\ e &= \frac{1}{36} t_i^2 t_o^3 (4t_i + 3t_o) \end{aligned} \quad (\text{A.29})$$

Given experimentally measured distributions Δx_o^2 , and Δv_o^2 , and parameters t_o and t_i , there is in general a discrepancy between the ideal Δx_i^2 given in Eq. A.27 for a lens application time that minimizes the width, and the experimentally measured final cloud width. Here we consider spontaneous heating attributed solely to D_v and set $D_x = 0$ (this is the case for spontaneous localization theories) [55]. In this case, the larger solution to the quadratic equation defined by Eq. A.28 for D_v is given by $D_v = \frac{-B+\sqrt{B^2-4AC}}{2A}$, where

$$\begin{aligned} A &= t_i^2 t_o^3 (4t_i + 3t_o) \\ B &= 12 \left(t_i^3 \Delta x_\ell^2 \left(1 + \frac{t_o}{t_i} (1 + 2\gamma^2) \right) - t_o^3 (\Delta x_i)_{\min}^2 \right) \\ C &= 36(t_i^2 \Delta v_o^2 \Delta x_o^2 - (\Delta x_i)_{\min}^2 \Delta x_\ell^2) \end{aligned} \quad (\text{A.30})$$

In the present experiment, the evolution times were $t_o = 1.1\text{s}$ and $t_i = 1.8\text{s}$. The initial cloud effective temperature was $1.6 \pm 0.1\text{ nK}$ (corresponding to $\Delta v_o = 0.39\text{ mm/sec}$). The initial cloud width is $\Delta x_o = 56\text{ }\mu\text{m}$ and the final refocused cloud width is $(\Delta x_i)_{\min} = 120 \pm 40\text{ }\mu\text{m}$. Based on these parameters, we set a bound on the spontaneous heating rate of $mD_v/k_B = 20 \pm 30\text{ pK/s}$. As discussed in [55], this limit on a fundamental heating rate can be compared to other experiments that test quantum mechanics in the macroscopic regime using the relation $D_v = \frac{\sigma_q^2}{m^2 \tau}$ (Fig. 1.4).

Appendix B

Miniatrization

While much of this thesis has focused on long-baseline atom interferometry for improved sensitivity (see Section 1.2), many applications require compact portable sensors of acceleration, rotation, or gravity [14, 15].¹ Therefore, I have undertaken a design study of miniaturizing the Stanford 10 m atom interferometer (Fig. B.1).

¹Despite their small size, a variety of techniques can improve the sensitivity of these devices (LMT, lattice manipulations, interleaved measurements, etc.). In principle, these techniques can be implemented in the 10 m tower as well, and it will generally be more sensitive because of its larger size and longer interrogation time.

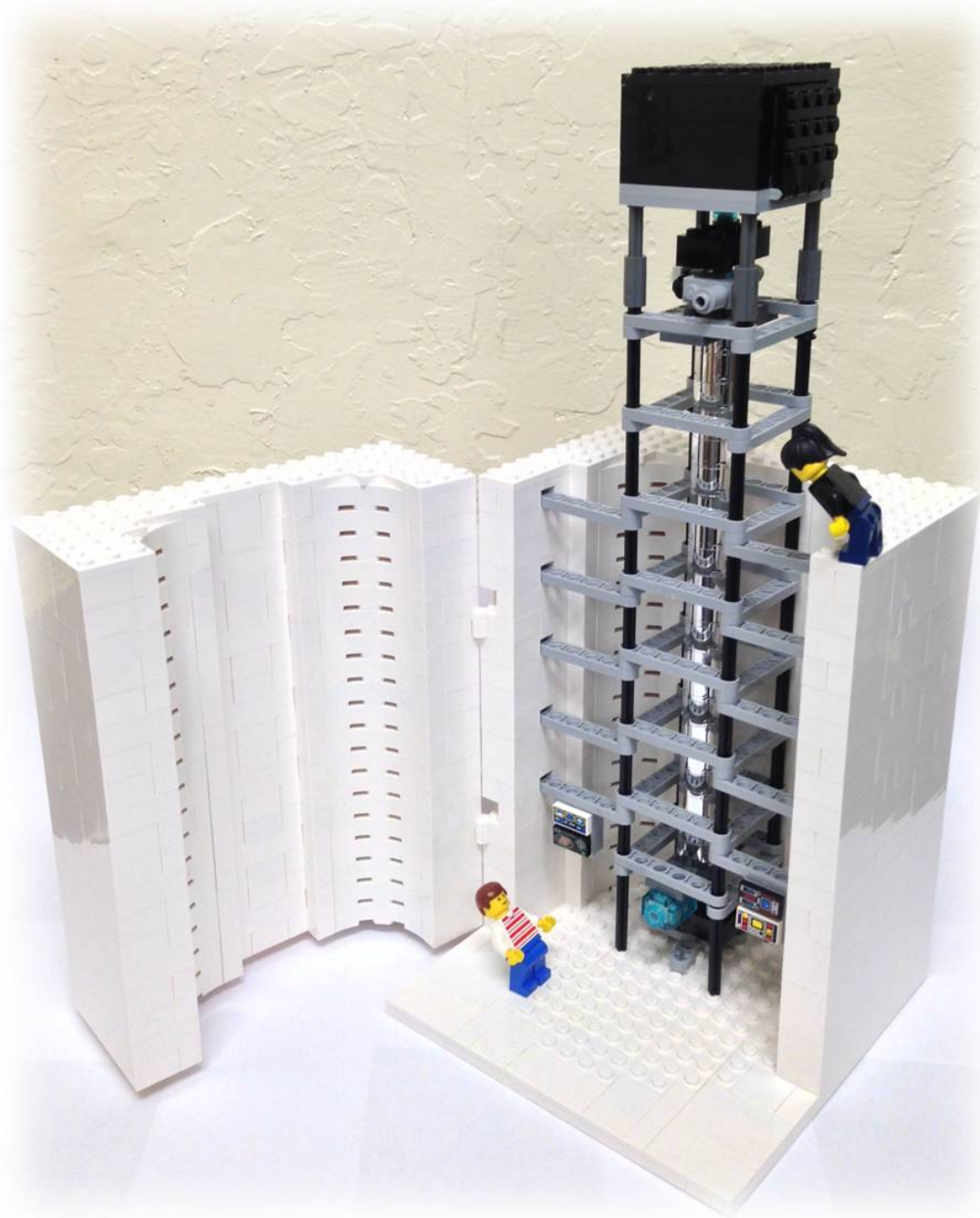


Figure B.1: A scale model of the Stanford 10 m atom interferometer. 927 pieces.

Bibliography

- [1] J. Adams, et al. Experimental and theoretical challenges in the search for the quark-gluon plasma: The STAR Collaboration’s critical assessment of the evidence from RHIC collisions. *Nuclear Physics A*, 757(1-2):102–183, August 2005.
- [2] Trong-Kha Truong, Donald W. Chakeres, Douglas W. Scharre, David Q. Beversdorf, and Petra Schmalbrock. Blipped multi gradient-echo slice excitation profile imaging (bmGESEPI) for fast T_2^* measurements with macroscopic B_0 inhomogeneity compensation. *Magnetic Resonance in Medicine*, 55(6):1390–5, June 2006.
- [3] Paul R. Berman, editor. *Atom Interferometry*. Academic Press, San Diego, 1997.
- [4] Alexander D. Cronin, J. Schmiedmayer, and David E. Pritchard. Optics and interferometry with atoms and molecules. *Reviews of Modern Physics*, 81(3):1051–1129, July 2009.
- [5] J. B. Fixler, G. T. Foster, J. M. McGuirk, and M. A. Kasevich. Atom interferometer measurement of the Newtonian constant of gravity. *Science*, 315(5808):74–7, January 2007.
- [6] G. Lamporesi, A. Bertoldi, L. Cacciapuoti, M. Prevedelli, and G. M. Tino. Determination of the newtonian gravitational constant using atom interferometry. *Physical Review Letters*, 100(5):050801, February 2008.

- [7] Rym Bouchendira, Pierre Cladé, Saïda Guellati-Khélifa, François Nez, and François Biraben. New determination of the fine structure constant and test of the quantum electrodynamics. *Physical Review Letters*, 106(8):080801, February 2011.
- [8] T. L. Gustavson, P. Bouyer, and M. A. Kasevich. Precision rotation measurements with an atom interferometer gyroscope. *Physical Review Letters*, 78(11):2046–2049, March 1997.
- [9] R. Geiger, et al. Detecting inertial effects with airborne matter-wave interferometry. *Nature Communications*, 2:474, January 2011.
- [10] A. Peters, K. Y. Chung, and S. Chu. High-precision gravity measurements using atom interferometry. *Metrologia*, 38(1):25–61, February 2001.
- [11] J. M. McGuirk, G. T. Foster, J. B. Fixler, M. J. Snadden, and M. A. Kasevich. Sensitive absolute-gravity gradiometry using atom interferometry. *Physical Review A*, 65(3):033608, February 2002.
- [12] D. A. Braje, S. A. DeSavage, C. L. Adler, J. P. Davis, and F. A. Narducci. A frequency selective atom interferometer magnetometer. *Journal of Modern Optics*, 61(1):61–71, January 2014.
- [13] N. Poli, C. W. Oates, P. Gill, and G. M. Tino. Optical atomic clocks. *Rivista del Nuovo Cimento*, 36(12):555–624, 2013.
- [14] Jason M. Hogan, David M. S. Johnson, and Mark A. Kasevich. Light-pulse atom interferometry. In E. Arimondo, W. Ertmer, and W. P. Schleich, editors, *Proceedings of the International School of Physics “Enrico Fermi” on Atom Optics and Space Physics*, volume 0806, pages 411–447, Amsterdam, June 2009. IOS Press.
- [15] Brenton Young, et al. AOSense, Inc. (<http://aosense.com/>).

- [16] M. Kasevich and S. Chu. Measurement of the gravitational acceleration of an atom with a light-pulse atom interferometer. *Applied Physics B*, 54(5):321–332, May 1992.
- [17] Sheng-wei Chiow, Tim Kovachy, Hui-Chun Chien, and Mark A. Kasevich. $102\hbar k$ Large Area Atom Interferometers. *Physical Review Letters*, 107(13):130403, September 2011.
- [18] Peter W. Graham, Jason M. Hogan, Mark A. Kasevich, and Surjeet Rajendran. New method for gravitational wave detection with atomic sensors. *Physical Review Letters*, 110(17):171102, April 2013.
- [19] G. Biedermann. *Gravity tests, differential accelerometry and interleaved clocks with cold atom interferometers*. PhD thesis, Stanford University, 2007.
- [20] Jason Hogan. *Towards precision tests of general relativity using an atom interferometer*. PhD thesis, Stanford University, 2010.
- [21] K. Bongs, R. Launay, and M. A. Kasevich. High-order inertial phase shifts for time-domain atom interferometers. *Applied Physics B*, 84(4):599–602, August 2006.
- [22] Savas Dimopoulos, Peter W. Graham, Jason M. Hogan, and Mark A. Kasevich. General relativistic effects in atom interferometry. *Physical Review D*, 78(4):042003, August 2008.
- [23] Savas Dimopoulos, Peter W. Graham, Jason M. Hogan, Mark A. Kasevich, and Surjeet Rajendran. Atomic gravitational wave interferometric sensor. *Physical Review D*, 78(12):122002, December 2008.
- [24] J. G. Bohnet, K. C. Cox, M. A. Norcia, J. M. Weiner, Z. Chen, and J. K. Thompson. Reduced spin measurement back-action for a phase sensitivity ten times beyond the standard quantum limit. *Nature Photonics*, July 2014.

- [25] Ian D. Leroux, Monika H. Schleier-Smith, and Vladan Vuletić. Implementation of cavity squeezing of a collective atomic spin. *Physical Review Letters*, 104(7):073602, February 2010.
- [26] D. J. Wineland, J. J. Bollinger, W. M. Itano, F. L. Moore, and D. J. Heinzen. Spin squeezing and reduced quantum noise in spectroscopy. *Physical Review A*, 46(11):R6797, 1992.
- [27] Onur Hosten, Nils J. Engelsen, Rajiv Krishnakumar, and Mark A. Kasevich. Quantum metrology frontiers with highly squeezed quantum states of atomic ensembles. *DAMOP 2014*, (<http://meetings.aps.org/Meeting/DAMOP14/Session/K1>), 2014.
- [28] Savas Dimopoulos, Peter W. Graham, Jason M. Hogan, and Mark A. Kasevich. Testing general relativity with atominterferometry. *Physical Review Letters*, 98(11):111102, March 2007.
- [29] Susannah Dickerson. *Long-time atom interferometry for precision tests of fundamental physics*. PhD thesis, Stanford University, 2014.
- [30] James G. Williams, Slava G. Turyshev, and Dale H. Boggs. Progress in lunar laser ranging tests of relativistic gravity. *Physical Review Letters*, 93(26):261101, December 2004.
- [31] S. Schlamminger, K.-Y. Choi, T. A. Wagner, J. H. Gundlach, and E. G. Adelberger. Test of the equivalence principle using a rotating torsion balance. *Physical Review Letters*, 100(4):041101, January 2008.
- [32] Sebastian Fray, Cristina Alvarez Diez, Theodor W. Hänsch, and Martin Weitz. Atomic interferometer with amplitude gratings of light and its applications to atom based tests of the equivalence principle. *Physical Review Letters*, 93(24):240404, December 2004.
- [33] D. Schlippert, J. Hartwig, H. Albers, L. L. Richardson, C. Schubert, A. Roura, W. P. Schleich, W. Ertmer, and E. M. Rasel. Quantum test of the universality of free fall. *Physical Review Letters*, 112(20):203002, May 2014.

- [34] M. G. Tarallo, T. Mazzoni, N. Poli, D. V. Sutyrin, X. Zhang, and G. M. Tino. Test of Einstein equivalence principle for 0-Spin and half-integer-spin atoms: Search for spin-gravity coupling effects. *Physical Review Letters*, 113(2):023005, July 2014.
- [35] Michael A. Hohensee, Steven Chu, Achim Peters, and Holger Müller. Equivalence principle and gravitational redshift. *Physical Review Letters*, 106(15):151102, April 2011.
- [36] R. V. Pound and G. A. Rebka Jr. Apparent weight of photons. *Physical Review Letters*, 4(7):337–341, April 1960.
- [37] C. W. Chou, D. B. Hume, T. Rosenband, and D. J. Wineland. Optical clocks and relativity. *Science*, 329(5999):1630–1633, September 2010.
- [38] Charles W. Misner, Kip S. Thorne, and John Archibald Wheeler. *Gravitation*. W.H. Freeman and Company, 1973.
- [39] Stanley E. Whitcomb. Ground-based gravitational-wave detection: now and future. *Classical and Quantum Gravity*, 25(11):114013, June 2008.
- [40] Matthew Pitkin, Stuart Reid, Sheila Rowan, and Jim Hough. Gravitational wave detection by interferometry (ground and space). *Living Reviews in Relativity*, 14:5, 2011.
- [41] J. Abadie, et al. Directional limits on persistent gravitational waves using LIGO S5 science data. *Physical Review Letters*, 107(27):271102, December 2011.
- [42] J. Aasi, et al. Improved upper limits on the stochastic gravitational-wave background from 2009-2010 LIGO and Virgo data. (arXiv:1406.4556v1 [gr-qc]), 2014.
- [43] P. A. R. Ade, et al. Detection of B-mode polarization at degree angular scales by BICEP2. *Physical Review Letters*, 112(24):241101, June 2014.

- [44] Pau Amaro-Seoane, et al. Low-frequency gravitational-wave science with eLISA/NGO. *Classical and Quantum Gravity*, 29(12):124016, June 2012.
- [45] Jason M. Hogan, et al. An atomic gravitational wave interferometric sensor in low earth orbit (AGIS-LEO). *General Relativity and Gravitation*, 43(7):1953–2009, May 2011.
- [46] Savas Dimopoulos, Peter W. Graham, Jason M. Hogan, Mark A. Kasevich, and Surjeet Rajendran. Gravitational wave detection with atom interferometry. *Physics Letters B*, 678(1):37–40, July 2009.
- [47] J. M. Hogan, S. M. Dickerson, T. Kovachy, A. Sugarbaker, and M. A. Kasevich. Detecting gravitational waves with atom interferometry. In G. M. Tino and M. A. Kasevich, editors, *Proceedings of the International School of Physics “Enrico Fermi” on Atom Interferometry*, page (Submitted), 2014.
- [48] Paul McNamara. Overview of LISA Pathfinder (LISA-LPF-RP-0001). (1), 2009.
- [49] Angelo Bassi, Kinjalk Lochan, Seema Satin, Tejinder Singh, and Hendrik Ulbricht. Models of wave-function collapse, underlying theories, and experimental tests. *Reviews of Modern Physics*, 85(2):471–527, April 2013.
- [50] Markus Arndt and Klaus Hornberger. Testing the limits of quantum mechanical superpositions. *Nature Physics*, 10(4):271–277, April 2014.
- [51] Gian Carlo Ghirardi, Philip Pearle, and Alberto Rimini. Markov processes in Hilbert space and continuous spontaneous localization of systems of identical particles. *Physical Review A*, 42(1):78–89, 1990.
- [52] Roger Penrose. On gravity’s role in quantum state reduction. *General Relativity and Gravitation*, 28(5):581–600, 1996.
- [53] Ertan Göklü and Claus Lämmerzahl. Fluctuations of spacetime and holographic noise in atomic interferometry. *General Relativity and Gravitation*, 43(7):2065–2088, January 2011.

- [54] Stefan Nimmrichter. *Macroscopic matter-wave interferometry*. PhD thesis, Universität Wien, 2013.
- [55] Stefan Nimmrichter and Klaus Hornberger. Macroscopicity of mechanical quantum superposition states. *Physical Review Letters*, 110(16):160403, 2013.
- [56] T. Banks, L. Susskind, and M. E. Peskin. Difficulties for the evolution of pure states into mixed states. *Nuclear Physics B*, 244:125–134, 1984.
- [57] Susannah M. Dickerson, Jason M. Hogan, Alex Sugarbaker, David M. S. Johnson, and Mark A. Kasevich. Multiaxis inertial sensing with long-time point source atom interferometry. *Physical Review Letters*, 111(8):083001, August 2013.
- [58] Alex Sugarbaker, Susannah M. Dickerson, Jason M. Hogan, David M. S. Johnson, and Mark A. Kasevich. Enhanced atom interferometer readout through the application of phase shear. *Physical Review Letters*, 111(11):113002, September 2013.
- [59] Tim Kovachy, Jason M. Hogan, Alex Sugarbaker, Susannah M. Dickerson, Christine A. Donnelly, Chris Overstreet, and Mark A. Kasevich. Matter wave lensing to picokelvin temperatures. *Submitted to PRL*, (arXiv:1407.6995v1 [physics.atom-ph]), 2014.
- [60] Tim Kovachy, Jason M. Hogan, Alex Sugarbaker, Susannah M. Dickerson, Christine A. Donnelly, Chris Overstreet, and Mark A. Kasevich. Matter wave lensing to picokelvin temperatures (supplemental materials). (Supplemental Materials from arXiv:1407.6995v1 [physics.atom-ph]), 2014.
- [61] J. M. Hogan, J. Hammer, S.-w. Chiow, S. Dickerson, D. M. S. Johnson, T. Kovachy, A. Sugarbaker, and M. A. Kasevich. Precision angle sensor using an optical lever inside a Sagnac interferometer. *Optics letters*, 36(9):1698–700, May 2011.
- [62] Susannah Dickerson, Jason M. Hogan, David M. S. Johnson, Tim Kovachy, Alex Sugarbaker, Sheng-wei Chiow, and Mark A. Kasevich. A high-performance

- magnetic shield with large length-to-diameter ratio. *The Review of Scientific Instruments*, 83(6):065108, June 2012.
- [63] David Marvin Slaughter Johnson. *Long baseline atom interferometry*. PhD thesis, Stanford University, 2011.
- [64] G. W. Biedermann, K. Takase, X. Wu, L. Deslauriers, S. Roy, and M. A. Kasevich. Zero-dead-time operation of interleaved atomic clocks. *Physical Review Letters*, 111(17):170802, October 2013.
- [65] Steven Chu. The manipulation of neutral particles. *Reviews of Modern Physics*, 70(3):685–706, 1998.
- [66] C. N. Cohen-Tannoudji. Manipulating atoms with photons. *Reviews of Modern Physics*, 70(3):707–719, 1998.
- [67] W. D. Phillips. Laser cooling and trapping of neutral atoms. *Reviews of Modern Physics*, 70(3):721–741, 1998.
- [68] E. A. Cornell and C. E. Wieman. Nobel lecture: Bose-Einstein condensation in a dilute gas, the first 70 years and some recent experiments. *Reviews of Modern Physics*, 74(3):875–893, 2002.
- [69] Wolfgang Ketterle. Nobel lecture: When atoms behave as waves: Bose-Einstein condensation and the atom laser. *Reviews of Modern Physics*, 74(4):1131–1151, 2002.
- [70] Umakant D. Rapol, Ajay Wasan, and Vasant Natarajan. Loading of a Rb magneto-optic trap from a getter source. *Physical Review A*, 64(2):023402, June 2001.
- [71] Daniel A. Steck. Rubidium 87 D line data. Available online at <http://steck.us/alkalidata>. (revision 2.1.4, 23 December 2010).
- [72] Daniel A. Steck. Rubidium 85 D line data. Available online at <http://steck.us/alkalidata>. (revision 2.1.6, 20 September 2013).

- [73] Kathryn Moler, David S. Weiss, Mark Kasevich, and Steven Chu. Theoretical analysis of velocity-selective Raman transitions. *Physical Review A*, 45(1):342–348, 1992.
- [74] H. J. Metcalf and P. van der Straten. *Laser Cooling and Trapping*. Springer-Verlag, New York, 1999.
- [75] H. J. Lewandowski, D. M. Harber, D. L. Whitaker, and E. A. Cornell. Simplified system for creating a Bose-Einstein condensate. *Journal of Low Temperature Physics*, 132(5/6):309, 2003.
- [76] Daryl W. Preston. Doppler-free saturated absorption: Laser spectroscopy. *American Journal of Physics*, 64(11):1432, 1996.
- [77] E. A. Donley, T. P. Heavner, F. Levi, M. O. Tataw, and S. R. Jefferts. Double-pass acousto-optic modulator system. *Review of Scientific Instruments*, 76(6):063112, 2005.
- [78] D. M. S. Johnson, J. M. Hogan, S.-w. Chiow, and M. A. Kasevich. Broadband optical serrodyne frequency shifting. *Optics letters*, 35(5):745–7, March 2010.
- [79] Ken Takase, John K. Stockton, and Mark A. Kasevich. High-power pulsed-current-mode operation of an overdriven tapered amplifier. *Optics letters*, 32(17):2617–9, September 2007.
- [80] Eric D. Black. An introduction to PoundDreverHall laser frequency stabilization. *American Journal of Physics*, 69(1):79, 2001.
- [81] Sheng-wei Chiow, Tim Kovachy, Jason M. Hogan, and Mark A. Kasevich. Generation of 43 W of quasi-continuous 780 nm laser light via high-efficiency, single-pass frequency doubling in periodically poled lithium niobate crystals. *Optics letters*, 37(18):3861–3863, September 2012.
- [82] R. Dubessy, K. Merloti, L. Longchambon, P.-E. Pottie, T. Liennard, A. Perrin, V. Lorent, and H. Perrin. Rubidium-87 Bose-Einstein condensate in an optically plugged quadrupole trap. *Physical Review A*, 85(1):013643, January 2012.

- [83] Vladimir G. Minogin, James A. Richmond, and Geoffrey I. Opat. Time-orbiting-potential quadrupole magnetic trap for cold atoms. *Physical Review A*, 58(4):3138–3145, October 1998.
- [84] E. Hodby, G. Hechenblaikner, O. M. Maragò, J. Arlt, S. Hopkins, and C. J. Foot. Bose-Einstein condensation in a stiff TOP trap with adjustable geometry. *Journal of Physics B: Atomic, Molecular and Optical Physics*, 33(19):4087–4094, October 2000.
- [85] S. Chu, J. E. Bjorkholm, A. Ashkin, J. P. Gordon, and L. W. Hollberg. Proposal for optically cooling atoms to temperatures of the order of 10^{-6} K. *Optics letters*, 11(2):73, February 1986.
- [86] Hubert Ammann and Nelson Christensen. Delta kick cooling: A new method for cooling atoms. *Physical Review Letters*, 78(11):2088–2091, March 1997.
- [87] E. Maréchal, S. Guibal, J.-L. Bossennec, R. Barbé, J.-C. Keller, O. Gorceix, E. Marechal, and R Barbe. Longitudinal focusing of an atomic cloud using pulsed magnetic forces. *Physical Review A*, 59(6):4636–4640, June 1999.
- [88] M. Morinaga, I. Bouchoule, J.-C. Karam, and C. Salomon. Manipulation of motional quantum states of neutral atoms. *Physical Review Letters*, 83(20):4037–4040, November 1999.
- [89] S. H. Myrskog, J. K. Fox, H. S. Moon, J. B. Kim, and A. M. Steinberg. Modified “ δ -kick cooling” using magnetic field gradients. *Physical Review A*, 61(5):053412, April 2000.
- [90] Pierre Meystre. *Atom Optics*. Springer-Verlag, New York, 2001.
- [91] Eric A. Cornell, Chris Monroe, and Carl E. Wieman. Multiply loaded, ac magnetic trap for neutral atoms. *Physical Review Letters*, 67(18):2439–2442, October 1991.

- [92] David A. Smith, Aidan S. Arnold, Matthew J. Pritchard, and Ifan G. Hughes. Experimental single-impulse magnetic focusing of launched cold atoms. *Journal of Physics B: Atomic, Molecular and Optical Physics*, 41(12):125302, June 2008.
- [93] Jean-François Schaff, Xiao-Li Song, Patrizia Vignolo, and Guillaume Labeyrie. Fast optimal transition between two equilibrium states. *Physical Review A*, 82(3):033430, September 2010.
- [94] L. Zhou, et al. Development of an atom gravimeter and status of the 10-meter atom interferometer for precision gravity measurement. *General Relativity and Gravitation*, 43(7):1931–1942, March 2011.
- [95] J. Hecker Denschlag, J. E. Simsarian, H. Häffner, C. McKenzie, A. Browaeys, D. Cho, K. Helmerson, S. L. Rolston, and W. D. Phillips. A Bose-Einstein condensate in an optical lattice. *Journal of Physics B: Atomic, Molecular and Optical Physics*, 35(14):3095–3110, July 2002.
- [96] H. Pichler, A. J. Daley, and P. Zoller. Nonequilibrium dynamics of bosonic atoms in optical lattices: Decoherence of many-body states due to spontaneous emission. *Physical Review A*, 82(6):063605, December 2010.
- [97] Fabrice Gerbier and Yvan Castin. Heating rates for an atom in a far-detuned optical lattice. *Physical Review A*, 82(1):013615, July 2010.
- [98] Tim Kovachy, Jason M. Hogan, David M. S. Johnson, and Mark A. Kasevich. Optical lattices as waveguides and beam splitters for atom interferometry: An analytical treatment and proposal of applications. *Physical Review A*, 82(1):013638, July 2010.
- [99] H. Müntinga, et al. Interferometry with Bose-Einstein condensates in microgravity. *Physical Review Letters*, 110(9):093602, February 2013.
- [100] Mark Kasevich and Steven Chu. Atomic interferometry using stimulated Raman transitions. *Physical Review Letters*, 67(2):181–184, July 1991.

- [101] K. B. Davis, M.-O. Mewes, M. R. Andrews, N. J. van Druten, D. S. Durfee, D. M. Kurn, and W. Ketterle. Bose-Einstein condensation in a gas of sodium atoms. *Physical Review Letters*, 75(22):3969–3973, November 1995.
- [102] C. Monroe, W. Swann, H. Robinson, and C. Wieman. Very cold trapped atoms in a vapor cell. *Physical Review Letters*, 65(13):1571–1574, September 1990.
- [103] Shau-Yu Lan, Pei-Chen Kuan, Brian Estey, Philipp Haslinger, and Holger Müller. Influence of the Coriolis force in atom interferometry. *Physical Review Letters*, 108(9):090402, February 2012.
- [104] Stephen R. Segal, Quentin Diot, Eric A. Cornell, Alex A. Zozulya, and Dana Z. Anderson. Revealing buried information: Statistical processing techniques for ultracold-gas image analysis. *Physical Review A*, 81(5):053601, May 2010.
- [105] G. T. Foster, J. B. Fixler, J. M. McGuirk, and M. A. Kasevich. Method of phase extraction between coupled atom interferometers using ellipse-specific fitting. *Optics Letters*, 27(11):951–953, 2002.
- [106] Holger Müller, Sheng-wei Chiow, Sven Herrmann, Steven Chu, and Keng-Yeow Chung. Atom-interferometry tests of the isotropy of post-Newtonian gravity. *Physical Review Letters*, 100(3):031101, January 2008.
- [107] Jürgen Audretsch and Karl-Peter Marzlin. Ramsey fringes in atomic interferometry: Measurability of the influence of space-time curvature. *Physical Review A*, 50(3):2080–2095, September 1994.
- [108] M. V. R. K. Murty. The use of a single plane parallel plate as a lateral shearing interferometer with a visible gas laser source. *Applied Optics*, 3(4):531–534, 1964.
- [109] T. Schumm, S. Hofferberth, L. M. Andersson, S. Wildermuth, S. Groth, I. Bar-Joseph, J. Schmiedmayer, and P. Krüger. Matter-wave interferometry in a double well on an atom chip. *Nature Physics*, 1(1):57–62, September 2005.

- [110] Florian Baumgärtner, R. J. Sewell, S. Eriksson, I. Llorente-Garcia, Jos Dingjan, J. P. Cotter, and E. A. Hinds. Measuring energy differences by BEC interferometry on a chip. *Physical Review Letters*, 105(24):243003, December 2010.
- [111] S. Cahn, A. Kumarakrishnan, U. Shim, T. Sleator, P. Berman, and B. Dubetsky. Time-domain de Broglie wave interferometry. *Physical Review Letters*, 79(5):784–787, August 1997.
- [112] S. Gupta, K. Dieckmann, Z. Hadzibabic, and D. E. Pritchard. Contrast interferometry using Bose-Einstein condensates to measure h/m and α . *Physical Review Letters*, 89(14):140401, September 2002.
- [113] S. Beattie, B. Barrett, M. Weel, I. Chan, C. Mok, S. B. Cahn, and A. Kumarakrishnan. Influence of spontaneous emission on a single-state atom interferometer. *Physical Review A*, 77(1):013610, January 2008.
- [114] Saijun Wu, Alexey Tonyushkin, and Mara G. Prentiss. Observation of saturation of fidelity decay with an atom interferometer. *Physical Review Letters*, 103(3):034101, July 2009.
- [115] B. Barrett, A. Carew, S. Beattie, and A. Kumarakrishnan. Measuring the atomic recoil frequency using a modified grating-echo atom interferometer. *Physical Review A*, 87(3):033626, March 2013.
- [116] G. Wilpers, T. Binnewies, C. Degenhardt, U. Sterr, J. Helmcke, and F. Riehle. Optical clock with ultracold neutral atoms. *Physical Review Letters*, 89(23):230801, November 2002.
- [117] Olaf Mandel, Markus Greiner, Artur Widera, Tim Rom, Theodor W. Hänsch, and Immanuel Bloch. Controlled collisions for multi-particle entanglement of optically trapped atoms. *Nature*, 425(6961):937–40, October 2003.
- [118] Waseem S. Bakr, Jonathon I. Gillen, Amy Peng, Simon Fölling, and Markus Greiner. A quantum gas microscope for detecting single atoms in a Hubbard-regime optical lattice. *Nature*, 462(7269):74–78, November 2009.

- [119] A. E. Leanhardt, T. A. Pasquini, M. Saba, A. Schirotzek, Y. Shin, D. Kielpinski, D. E. Pritchard, and W. Ketterle. Cooling Bose-Einstein condensates below 500 picokelvin. *Science*, 301(5639):1513–5, September 2003.
- [120] Juris G. Kalnins, Jason M. Amini, and Harvey Gould. Focusing a fountain of neutral cesium atoms with an electrostatic lens triplet. *Physical Review A*, 72(4):043406, October 2005.
- [121] G. D. McDonald, C. C. N. Kuhn, S. Bennetts, J. E. Debs, K. S. Hardman, M. Johnsson, J. D. Close, and N. P. Robins. $80\hbar k$ momentum separation with Bloch oscillations in an optically guided atom interferometer. *Physical Review A*, 88(5):053620, November 2013.
- [122] W. J. Engelen, M. A. van der Heijden, D. J. Bakker, E. J. D. Vredenbregt, and O. J. Luiten. High-coherence electron bunches produced by femtosecond photoionization. *Nature Communications*, 4:1693, January 2013.
- [123] B. Dubetsky and M. Kasevich. Atom interferometer as a selective sensor of rotation or gravity. *Physical Review A*, 74(2):023615, August 2006.
- [124] E. Giese, W. Zeller, S. Kleinert, M. Meister, V. Tamma, A. Roura, and W. P. Schleich. The interface of gravity and quantum mechanics illuminated by Wigner phase space. (arXiv:1402.0963v1 [quat-ph]), 2014.
- [125] J. M. McGuirk, M. J. Snadden, and M. A. Kasevich. Large area light-pulse atom interferometry. *Physical Review Letters*, 85(21):4498–4501, November 2000.
- [126] Tim Kovachy, Sheng-wei Chiow, and Mark A. Kasevich. Adiabatic-rapid-passage multiphoton Bragg atom optics. *Physical Review A*, 86(1):011606, July 2012.
- [127] Holger Müller, Sheng-wei Chiow, Quan Long, Sven Herrmann, and Steven Chu. Atom interferometry with up to 24-photon-momentum-transfer beam splitters. *Physical Review Letters*, 100(18):180405, May 2008.
- [128] Malcolm H. Levitt. Composite pulses. *Progress in Nuclear Magnetic Resonance Spectroscopy*, 18:61–122, 1986.

- [129] K. Sakmann and M. Kasevich. Single shot three-dimensional imaging of dilute atomic clouds. *Submitted to OL*, (arXiv:1405.3598v1 [physics.atom-ph]), 2014.